Diplomarbeit in Physik

Ab initio investigation of the Dzyaloshinskii-Moriya interaction in transition-metal chains deposited on Platinum step-edges

von

Benedikt Schweflinghaus

vorgelegt der

Fakultät für Mathematik, Informatik und Naturwissenschaften
der Rheinisch-Westfälischen Technischen Hochschule Aachen

im
Oktober 2011

angefertigt am

Peter-Grünberg-Institut (PGI-1)
Forschungszentrum Jülich

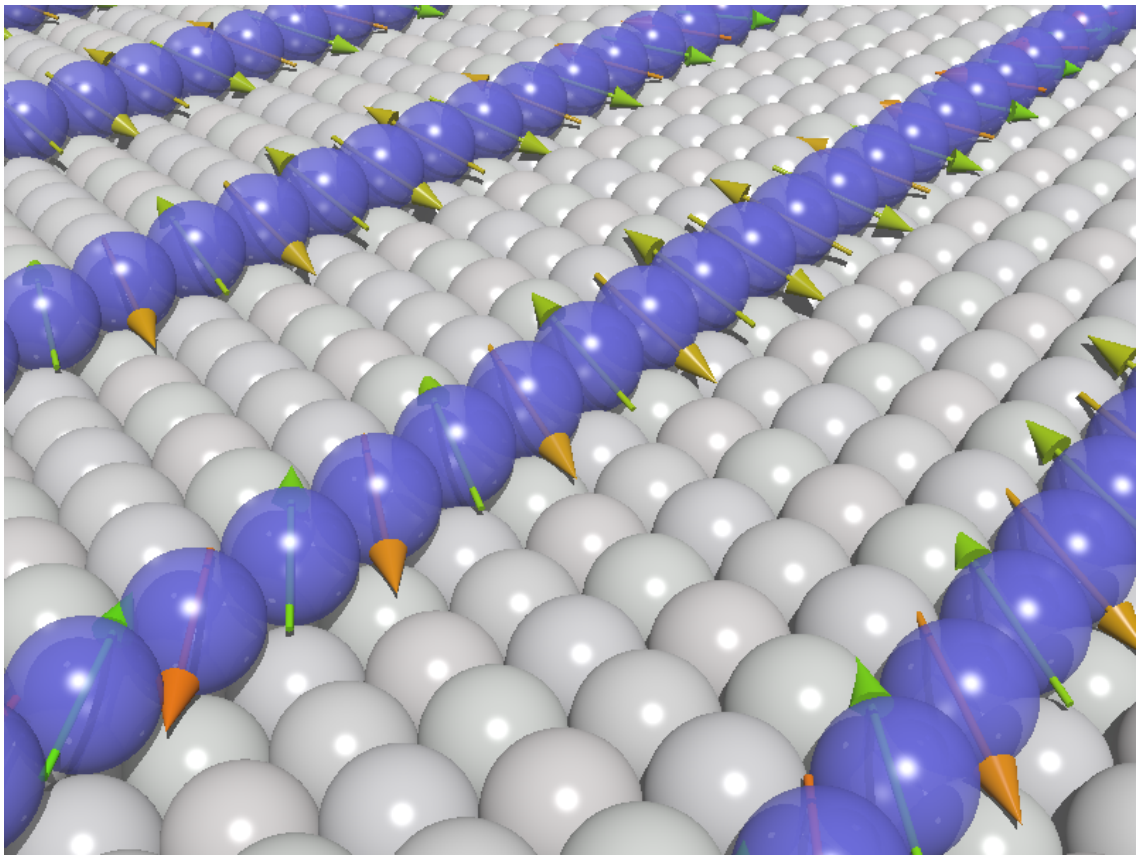

This is a visualization of the investigated surface structure. The top-view shows single-atomic chains of transition metals (blue spheres) deposited along the step edge of a Pt(664) surface (grey spheres), *i.e.* vicinal layers of Pt(111) terraces with a width of six atomic rows. The spin moments of the transition metals (colored arrows) are likely to form spin spirals of unique rotational sense if the Dzyaloshinskii-Moriya interaction is strong enough. This thesis investigates this type of interaction for the first time for these one-dimensional magnetic systems.

Contents

1 Introduction

The phenomenon of magnetism is one of the oldest and yet vibrant branches of scientific research in modern solid state physics. Whereas by now the principle physical origin can be regarded as well understood, magnetism today meets challenges on 20 orders of length scales starting at coherent superpositions of a few spins in a molecular magnet to magnetic chains, thin films, surfaces, patterned multilayers to single crystals and complex multicomponent frustrated magnets and stretches as well over 20 orders of magnitude in time starting at femtosecond time scale and ends up by years. Magnetism has also a dimension into strongly correlated materials and has a large impact into applications. As an example, a large number of publications witnesses the investigation of material-related characteristics such as the interaction of magnetic and non-magnetic atoms in a bulk crystal based on a variety of exchange-interaction models (for a review see *e.g.* [1]). There are still lots of thrilling questions that remain unanswered, among them those related to the exploration of magnetism in low-dimensional surface structures [2, 3], which is the topic of this thesis. It is to emphasize that in the last two to three decades an enormous effort has been undertaken to explore magnetic properties of such systems from both, the experimental and the theoretical point of view.

Especially transition-metal (TM) films down to the monolayer limit supported by metal surfaces playing the role of an interacting substrate are a topic of general research in recent years leading to the discovery of novel magnetic phases [4] and vivid discussions about the role of *e.g.* magnetic anisotropies in low-dimensional systems. This effort of investigation is induced by basic questions leading to fundamental research and stimulated by industrial demands for the development of novel materials capable of storing information with increasingly higher density that preserve its information for a long lifetime. Sophisticated investigation tools such as spin-polarized scanning tunneling microscopy or magnetic force microscopy give insight in submolecular systems and their magnetic properties. This is complimented by modern simulation concepts and algorithms that rely on a modern theory to describe electronic properties on the basis of the many-body problem, known as the density functional theory (DFT), a theory that has proven to be of predictive power for the investigation of magnetic systems. Its applicability benefits from using the charge density as principle variable instead of a many-body wave function and from increasingly powerful computers that have reached the peta-flop scale in case of massively parallel computers.

An example of a breathtaking discovery made in ultrathin metallic heterostructures of alternating ferromagnetic and non-magnetic atomic layers is the giant magneto-resistance (GMR) effect [5, 6] that was awarded with the Nobel prize in physics in the year 2007. The GMR effect is world-wide considered to be the starting point of a new field known today as spintronics, *i.e.* the incorporation of the electronic spin mo-

ment as a central physical quantity in technological applications and electronic devices. It is therefore not inappropriate to state that the fundament of the present era of binary information, starting with the development of computers up to the creation of laptops and smartphones in recent years, is partly made possible by this field of research, the exploration of magnetism in low-dimensional systems.

As a consequence of intensive research of two-dimensional (2D) systems in the last decades, a vista to a new challenge has become available: The extension of the focus of research to the exploration of magnetic systems of even lower dimensionality, *i.e.* chains and adatoms deposited on substrates [7]. Experimentally great effort was put into assembling high-density engineered quasi-1D magnetic stripes of ten to 20 atomic rows [8, 9].

A breakthrough experiment was performed by Dallmeyer *et al.* [10] who realized the growth of single-atomic Co and Cu chains deposited on vicinal Pt(997) terraces. The magnetic measurements carried out by Gambardella *et al.* [11, 12] exhibited a long-ranged ferromagnetic order of the Co atoms along the step edges, when the temperature falls below the so-called blocking temperature of about 15 K [11]. On the other hand it is known from theoretical examinations that at finite temperatures in the limit of infinite chains a collinear magnetic structure breaks down to smaller ferromagnetic regions [13] separated by domain walls. It is therefore of major significance to explore and analyze the different magnetic interactions that are of importance for the formation of the magnetic ground state of this structure.

Gambardella *et al.* [11, 12] witnessed large magnetic anisotropies, *i.e.* large energy differences between hard and easy axis (the spin directions that lead to the highest and lowest energy value, respectively) and an unorthodox oscillatory behavior of the easy axis direction in reaching the crossover to the 2D TM-covered surface [14]. This triggered the accomplishment of a number of computational simulations [15, 16, 17, 18, 19, 20, 21] addressing the magnetic properties of this step-edged structure. In fact the previously mentioned oscillatory behavior could be confirmed by theoretical investigations [20] and could be explained by individual contributions to the magnetic anisotropy energy (MAE) and to the total orbital moment coming from the different Co chains and the spin-polarized Pt atoms in the substrate underneath.

Till 2007, the magnetic phases of low dimensional metallic magnets on substrate seemed understood in general by the conventional notion that any magnetic phase can be understood by three major interactions: The exchange interaction conceptionalized by the Heisenberg model, the magnetocristalline anisotropy and the dipole-dipole interaction. This foundation was shaken a few years ago by Bode *et al.* [22] who reported on the discovery of non-collinear spiral magnetic structures of a unique handedness – a new magnetic phase in 2D thin-film systems on substrates that lack structural inversion symmetry. This novel magnetic ground state is only explainable when, besides the Heisenberg exchange and the magnetic anisotropies, a third magnetic contribution is taken into account. This is the so-called *Dzyaloshinskii-Moriya interaction* (DMI), a spin-orbit (SO) driven antisymmetric exchange interaction between two spins $\mathbf{S}_i$ and $\mathbf{S}_j$

of the form

$$E_{\mathrm{DM}} = \mathbf{D} \cdot (\mathbf{S}_i \times \mathbf{S}_j) \,,$$

that only appears in structures that lack inversion symmetry. Up to now several systems with a homochiral DMI-driven magnetic ground state are known (e.g. Mn/W(110), Cr/W(110), Fe/Ir(001)). For all cases the corresponding Dzyaloshinskii-vector (**D**-vector) is oriented along a high symmetry direction due to the symmetry of the surface.

In this thesis we address the question what does this discovery mean for the magnetism of single atom Co chains at a Pt(997) step-edge considering that the experiments were analyzed previously not knowing of the existance of the Dzyaloshinskii-Moriya interaction and that it may play an important role. Additionally SO-related effects increase typically in structures of reduced dimensions, which may also be the case for the strength of the DMI. *I.e.* the question arises whether the DMI reveals a **D**-vector with an unorthodox direction and of a strength large enough to introduce a homochiral magnetic phase.

Thus the present work contributes to the search for the magnetic ground state of monatomic TM chains deposited at the Pt step-edges from a theoretical point of view. The experimental investigated structure of a Pt(997) substrate is modeled by a Pt(664) surface, where vicinal step edges are closer to one another. The unit cell represents an inversion symmetric film structure with 7-8 layers of fcc Pt(111) containing in total two Co atoms distributed over both sides of the structure.

By accounting for a micromagnetic model (assuming that possible spiral magnetic structures are of long wave lengths), it is possible to determine the magnetic ground state evaluating in part independently by first-principles calculations three parameters that enter the micromagntic model and depend on the system's structure: Besides the spin stiffness and the anisotropy tensor the present work focuses for the first time on the investigation of the DMI in a 1D magnet. The strength and the direction of the **D**-vector with respect to the system's easy and hard axes must be taken into account as the different contributions favor different spin alignments.

The calculations are performed using the FLEUR code[23], a parallelized full-potential linearized augmented plane-wave (FLAPW) code based on DFT that has the unique capability of calculating the DMI interaction. The calculation of the DMI is not straightforward since non-collinear calculations are explored and DMI only occurs in the presence of SO coupling. Thus it is necessary to calculate either by using large supercells with commensurate magnetic moments or by using more sophisticated perturbative approaches. The calculations performed in this thesis use a computational scheme with a perturbative approach as implemented in the FLEUR code, where SO coupling is treated in first order perturbation theory. Since the expectation is that spiral magnetic structures are of long wave lengths this work uses a perturbative approach as implemented in the FLEUR code, where SO coupling is treated in first order perturbation theory [24]. The calculations presented in this thesis are of cutting edge considering combination of structural and magnetic complexity.

The thesis is structured as follows:

In Chapter 2 we describe the underlying model of magnetic interactions by analyzing the incorporated contributions coming from the spin stiffness, the anisotropy energy and the DMI. Then a micromagnetic model which is capable to describe non-collinear spin-spiral structures of long wave lengths is discussed. Within this analysis an emphasis is put on one-dimensional (1D) magnetic chain structures that preserve no symmetry but one mirror-plane perpendicular to the chain direction. Two criteria for the appearance of homogeneous and inhomogeneous spin spirals are derived.

In Chapter 3 we briefly summarize the main ideas and concepts of DFT as well as the Kohn-Sham reference system. Also this theory is expanded to spin systems and non-collinear magnetic structures in Chapter 4.

This will be followed by a description of the FLAPW method in Chapter 5, as all calculations are performed with the FLEUR code, an FLAPW code capable of dealing with non-collinear magnetic structures.

Then, the performed calculations are shown. In Chapter 6 the system of monatomic Co chains is analyzed and the contributions to the micromagnetic model are collected. This study also incorporates several additional test calculations that allow a prediction concerning the validity of the method and the calculated parameters. A comparison to investigations of two other TM chains, Fe and Mn chains, is given in Chapter 7. For all three investigated structures a prediction of the formed magnetic ground state is given.

In Chapter 8 we give a summary and an outlook. Cast into one sentence, we conclude by stating that monatomic chains of Fe and Co at the step edge of Pt(664) are ferromagnetic at sufficiently low temperatures and the DMI is not sufficient to introduce a new magnetic phase, but for a monatomic Mn chain we predict a left-rotating cycloidal spin spiral as magnetic ground state. We encourage experimentalists to confirm our prediction.

2 Simple Models for magnetic Structures in 1D magnets

In the course of the development of quantum mechanics in the beginning of the 20th century major progresses in the understanding of magnetism were achieved and the insights in this phenomenon and its underlying origin continuously have grown to the present day. In recent time an increased focus on low-dimensional magnetic systems on the atomic scale has become an exciting and beneficial branch of research [25]. This is mainly based on two reasons: First, the increasing amount of binary data to store requires higher information density, which asks for a deep understanding of the magnetic processes in a submicroscopic structure and the interaction among atoms therein. And secondly, reducing the dimensions from three-dimensional bulk crystals to a surface or even a wire structure usually lowers the symmetry, which gives rise to new kinds of interactions, such as the *Dzyaloshinskii-Moriya interaction* (DMI). Resulting from the interplay of the contributing interactions, magnetic structures beyond the collinear ferro-, ferri- and antiferromagnetic states can appear in such systems of reduced dimensionality.

The goal of this chapter is to introduce the wide field of simple models of magnetic structures to the reader and to discuss the major contributions to the system's energy. In this thesis transition metal chains deposited on a Pt substrate are investigated, therefore an emphasis is put on one-dimensional magnetic structures.

2.1 Spin Models on Lattices

To describe the magnetic interaction between atoms arranged in a lattice structure a variety of simple models is known. It is beyond the scope of this thesis to describe the different approaches. A detailed review on this topic can be found for example in Ref. [26]. Usually, these models are based on the assumption that the magnetic moment of each atom at lattice site $\mathbf{R}_i$ is given by a classical spin vector $\mathbf{S}_i$ with a normed magnitude (*cf.* Fig. 2.1), so that the model Hamiltonian and thus the energy is given by a function of these spin moments.[1]

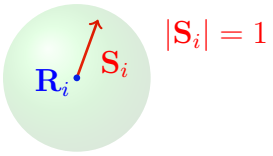

Fig. 2.1: An illustration of a spin vector $\mathbf{S}_i$ (red arrow) with origin at lattice site $\mathbf{R}_i$ (blue dot). The atom is indicated by a green shadow.

[1] More precisely, the local magnetic moment $\mathbf{m}_i$ is connected to the spin via $\mathbf{m}_i = -g\frac{\mu_\mathrm{B}}{\hbar}\mathbf{S}_i$, where $g \approx 2$ is the Landé factor, μ_B is the Bohr magneton and $\hbar$ is Planck's constant divided by 2π. However, a distinction between these two quantities will be dropped in most parts of the thesis.

A widely used ansatz is the Heisenberg model [13, 27, 28],

$$H_{\mathrm{H}} = -\sum_{i,j} J_{ij} \mathbf{S}_i \cdot \mathbf{S}_j \,. \tag{2.1}$$

This model allows for two-particle interactions only. The so-called exchange-interaction integrals J_{ij} usually decay fast with increasing distance $R_{ij} = |\mathbf{R}_j - \mathbf{R}_i|$. In some cases they can be restricted to nearest-neighbor interactions,

$$J_{ij} = \begin{cases} \frac{J}{2} & , \text{ for neighboring } \mathbf{R}_i \text{ and } \mathbf{R}_j \\ 0 & , \text{ else} \end{cases} \,. \tag{2.2}$$

Thus, the model can describe a ferromagnetic ($J > 0$) or an antiferromagnetic ($J < 0$) ground state.

Especially in metallic systems J_{ij} can exhibit a wide-ranged oscillatory behavior (see *e.g.* Ref. [29]). As a general solution to the Heisenberg model (2.1) for a lattice structure, it can be proven that the ground state is a superposition of spiral magnetic phases [30]. How this type of magnetic structure can be described mathematically is the topic of the next Section 2.1.1.

2.1.1 Spin Spirals

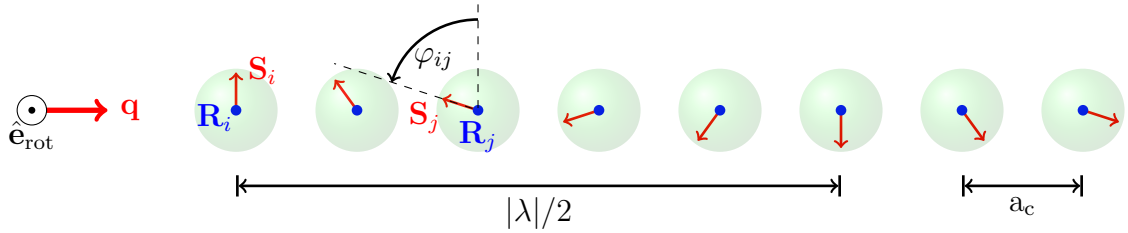

Fig. 2.2: Here, a visualization of a spin spiral with period length $|\lambda| = 10\,\mathrm{a_c}$ in a chain of atoms is shown. In accordance with the previously described spin models each atomic site carries a normed spin moment, illustrated by a red vector. The spin-spiral vector $\mathbf{q}$ is pointing along the propagation direction of the spiral and the rotation axis $\hat{\mathbf{e}}_{\mathrm{rot}}$ points out of the drawing plane.

A spin spiral is a periodic non-collinear magnetic structure of period length $|\lambda|$ in which the spin moments positioned at the atomic sites are rotated clockwise or anticlockwise around a fixed axis, the so-called *rotation axis* $\hat{\mathbf{e}}_{\mathrm{rot}}$, along a certain direction in the crystal, called spin-spiral direction or propagation direction. In analogy to the wave vector $\mathbf{k}$, one can define a spiral vector $\mathbf{q}$, that points along this direction. The length q of this vector is proportional to the reciprocal period length of the magnetic structure and is given in units of $2\pi \cdot a_{\mathrm{c}}^{-1}$, where a_{c} is the next-neighbor distance along the chain's direction. Thus, in the simple case of a homogeneous spiral magnetic structure with a

rotation axis pointing in z-direction, a spin vector $\mathbf{S}_j$ is given by

$$\mathbf{S}_j = \begin{pmatrix} \sin\vartheta \cdot \cos(\varphi_{ij} + \delta_i) \\ \sin\vartheta \cdot \sin(\varphi_{ij} + \delta_i) \\ \cos\vartheta \end{pmatrix} , \tag{2.3}$$

with the angle $\varphi_{ij} = \mathbf{q} \cdot \mathbf{R}_{ij}$ and δ_i accounting for a possible offset at lattice site $\mathbf{R}_i$. The cone angle (*i.e.* the angle between the rotation axis and the spin vectors) is given by ϑ. For $\vartheta = \frac{\pi}{2}$, the spiral rotates in the plane perpendicular to the rotation axis and is called a flat spiral. If the rotation axis is oriented along the $\mathbf{q}$-vector the spiral structure is called helical, and if it is perpendicular, the structure is called cycloidal. The latter case is indicated by Fig. 2.2. It is important to mention that this distinction only makes sense, when the spin space is adjunctive to the real space, which is realized via spin-orbit coupling (SOC). This effect is discussed in Chapter 4.

In order to distinguish the two possible rotational senses and to give a unique definition of the rotation axis, it is necessary to discuss the spin spiral with respect to a surface structure the atomic chain is placed on. With $\hat{\mathbf{e}}_y$ and $\hat{\mathbf{e}}_z$ pointing in chain and out-off-plane direction, respectively (*cf.* Fig. 2.3), the definition of the rotation axis reads

$$\hat{\mathbf{e}}_{\mathrm{rot}} = \frac{\mathbf{S}_0 \times \mathbf{S}_1}{|\mathbf{S}_0 \times \mathbf{S}_1|} \cdot \begin{cases} \mathsf{sign}([\mathbf{S}_0 \times \mathbf{S}_1] \cdot \hat{\mathbf{e}}_y) & , \text{ helical spiral} \\ \mathsf{sign}([\mathbf{S}_0 \times \mathbf{S}_1] \cdot \hat{\mathbf{e}}_z) & , \text{ cycloidal spiral} \end{cases} , \tag{2.4}$$

where the sign-function ensures that $\hat{\mathbf{e}}_{\mathrm{rot}}$ points in the vacuum half-space.

To distinguish spirals with different rotational senses, we define $\lambda > 0$ for a right-handed spiral and $\lambda < 0$ for a left-handed spiral and introduce the chirality

$$C = \mathsf{sign}([\mathbf{R}_1 - \mathbf{R}_0] \cdot \hat{\mathbf{e}}_y) \cdot \begin{cases} \mathsf{sign}([\mathbf{S}_0 \times \mathbf{S}_1] \cdot \hat{\mathbf{e}}_y) & , \text{ helical spiral} \\ \mathsf{sign}([\mathbf{S}_0 \times \mathbf{S}_1] \cdot \hat{\mathbf{e}}_z) & , \text{ cycloidal spiral} \end{cases} , \tag{2.5}$$

where C is positive for a right-handed spiral and negative for a left-handed spiral.

2.2 Extension of the Heisenberg Model

In a more general form, the two-particle interaction can be expressed in the form

$$H = -\sum_{i,j} \mathbf{S}_i^{\mathrm{T}} \underline{V}_{ij} \mathbf{S}_j \, , \tag{2.6}$$

where $\underline{V}_{ij}$ is a (3×3) matrix. It is useful to divide this matrix into a symmetric and an antisymmetric part,

$$\underline{V}_{ij} = \underline{V}_{ij}^{+} + \underline{V}_{ij}^{-} \quad , \; \underline{V}_{ij}^{\pm} = \frac{\underline{V}_{ij} \pm \underline{V}_{ij}^{\mathrm{T}}}{2} \, , \tag{2.7}$$

where the symmetric contribution is further separated into an isotropic and a traceless symmetric part,

$$\underline{V}_{ij}^{+} = J_{ij}\underline{\mathbb{1}} - \underline{K}_{ij} \; , \text{ with } J_{ij} = \frac{1}{3}\mathsf{tr}\big[\underline{V}_{ij}^{+}\big] \text{ and } \underline{K}_{ij} = -\left(\underline{V}_{ij}^{+} - J_{ij}\underline{\mathbb{1}}\right) . \tag{2.8}$$

For $i = j$ the onsite energy contribution $-\mathbf{S}_i^{\mathrm{T}} J_{ii} \underline{\mathbb{1}} \mathbf{S}_i = -J_{ii}$ yields the so-called *Stoner term*, which is independent of the spins' orientation. Due to its constant contribution to the energy, it can be neglected. The remaining isotropic part reveals the Heisenberg-type interaction. It usually is the energetically largest interaction term, considering that the other contributions at least partly require the previously in Section 2.1.1 mentioned spin-orbit interaction. Furthermore, the terms of the form $\mathbf{S}_i^{\mathrm{T}} \underline{K}_{ij} \mathbf{S}_j$ for $i \neq j$, named *pseudo-dipole term* or *symmetric anisotropy* [31] are expected to be small due to the fact that they are relativistic two-particle effects. They will not be considered in the following theoretical investigation. The remaining contribution ($i = j$) of the anisotropic symmetric part will be described by anisotropy tensors $\{\underline{K}_i\}$ and is the topic of Section 2.2.2.

Using the Levi-Civita symbol ϵ_{klm} the antisymmetric part can be rewritten in the form

$$-\mathbf{S}_i^{\mathrm{T}} \underline{V}_{ij}^{-} \mathbf{S}_j = -\mathbf{D}_{ij} \cdot (\mathbf{S}_i \times \mathbf{S}_j) \quad , \quad \text{where } \left(\underline{V}_{ij}^{-}\right)_{l,m} = \sum_{k=1}^{3} \left(\mathbf{D}_{ij}\right)_k \cdot \epsilon_{klm} \,. \tag{2.9}$$

This term is called Lifshitz invariant or Dzyaloshinskii-Moriya interaction [32, 33], where the vector $\mathbf{D}_{ij}$ is the Dzyaloshinskii-vector. How the symmetry of the system allows to constrain the components of this vector will be described in Section 2.2.1.

In conclusion the contributions to the energy, that are accounted for in this thesis, form the model Hamiltonian[2]

$$H = -\sum_{i \neq j} \left[J_{ij} \left(\mathbf{S}_i \cdot \mathbf{S}_j - 1 \right) + \mathbf{D}_{ij} \cdot (\mathbf{S}_i \times \mathbf{S}_j) \right] + \sum_i \mathbf{S}_i^{\mathrm{T}} \underline{K}_i \mathbf{S}_i \,. \tag{2.10}$$

2.2.1 The Dzyaloshinskii-Moriya Interaction

The antisymmetric exchange interaction described by Eq. (2.9) plays a central role in the investigation performed and presented within this thesis. In fact the properties of the chemical structure are chosen such, that the two most important and crucial requirements leading to a strong DMI are fulfilled:

- On the one hand the surface structure ensures a lack of inversion symmetry, which is necessary for the appearance of DMI in the first place.
- And on the other hand the choice of Pt as a heavy 5d metal to form the substrate provides a strong spin-orbit interaction among the magnetic atoms leading to a strong DMI.

By exploring an energy contribution of the form

$$E_{\mathrm{DM}} = -\mathbf{D}_{ij} \cdot (\mathbf{S}_i \times \mathbf{S}_j) = -\mathbf{D}_{ij} \cdot \hat{\mathbf{e}}_{\perp} \sin \varphi_{ij} \,, \tag{2.11}$$

[2] An additional energy offset $\sum_{i \neq j} J_{ij}$ is introduced, so that the Heisenberg-type contribution vanishes in a ferromagnetic structure.

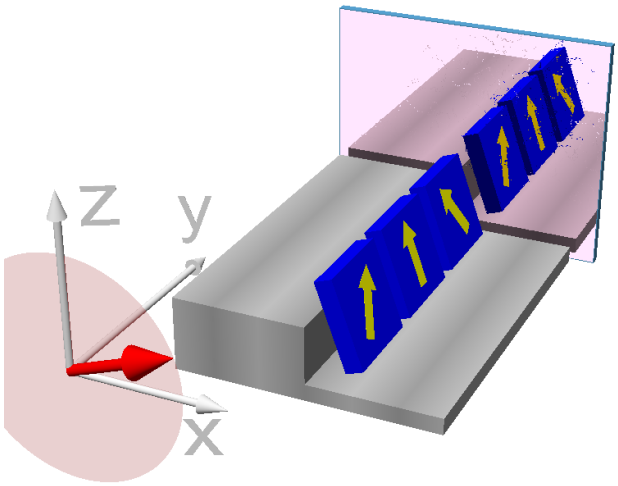

Fig. 2.3: The step-edged structure (gray) with the remaining mirror-plane symmetry perpendicular to the chain is shown as well as three atoms (blue) forming a flat spiral (yellow arrows). The direction of the Dzyaloshinskii-vector is constricted to the xz-plane and indicated by a red vector. In this figure the rotation axis is perpendicular to the spin moments (yellow arrows) and parallel to the Dzyaloshinskii-vector, so that the DMI reaches its extremal value.

it is obvious that this interaction is largest for $\varphi_{ij} = \frac{\pi}{2}$, *i.e.* the regarded spins are perpendicular to each other. Due to the scalar product with $\mathbf{S}_i \times \mathbf{S}_j$ only the projection of $\mathbf{D}_{ij}$ on $\hat{\mathbf{e}}_\perp$, the direction perpendicular to both spins, is of relevance. Also, $E_{\mathrm{DM}} = E_{\mathrm{DM}}(\varphi_{ji})$ fulfills the important relation

$$E_{\mathrm{DM}}(\varphi_{ji}) = -E_{\mathrm{DM}}(\varphi_{ij}) \quad , \text{ with } \varphi_{ji} = -\varphi_{ij} \, . \tag{2.12}$$

Due to Eq. (2.12) the energy contribution distinguishes left-handed ($\varphi_{ij} = \mathbf{q}\cdot\mathbf{R}_{ij} > 0$) and right-handed ($\varphi_{ij} < 0$) spirals: The energy is shifted upwards or downwards, depending on the rotational sense of the spiral structure. Therefore, DMI driven non-collinear magnetic spin arrangements always show a spiral structure with a unique sense of rotation, in contrast to those originating from Heisenberg-type interactions, *e.g.* Ref. [34].

The DMI is a spin-orbit driven effect, due to the fact that SOC is crucial for breaking the chiral symmetry. Without this relativistic energy contribution, it is not possible to distinguish left- and right-handed spirals: An operator that causes a reflection of the magnetic moments within the spin space always leaves the system's energy unchanged, as long as SOC is neglected. On the other hand, this operation changes the sign of the DMI by transforming a left-handed spiral into its right-handed counterpart, meaning that $E_{\mathrm{DM}}(\varphi_{ij}) = -E_{\mathrm{DM}}(\varphi_{ij}) = 0$.

Furthermore, the same argument leads to a vanishing DMI in systems with (real-space) inversion symmetry, where the inversion of spin and real space at the same time results in a system with the same energy but a different chirality and thus again $E_{\mathrm{DM}} = 0$.

It has been pointed out by Moriya [33] that in some systems already the consideration of the symmetry can provide an indication to the direction of the corresponding Dzyaloshinskii-vector $\mathbf{D}_{ij}$. In particular, if a mirror-plane exists, such that a spin $\mathbf{S}_i$ at lattice site $\mathbf{R}_i$ is reflected into $\mathbf{S}_j$ positioned at $\mathbf{R}_j$, the corresponding $\mathbf{D}_{ij}$ points into a direction within this plane. Since the investigated system is a chain-decorated step-edged structure (see Fig. 2.3), that contains a mirror-plane perpendicular to the direction along the step edge, the resulting Dzyaloshinskii-vector is expected to have a vanishing component along the chain direction. Thus, a helical spiral, meaning that

$\mathbf{S}_i \times \mathbf{S}_j$ points along the chain direction, is not expected to appear in the system, which is why the investigation is constrained to cycloidal spiral structures only.

2.2.2 The Magnetic Anisotropy Energy

Most magnetic materials show the tendency to prefer a certain direction of magnetization, *i.e.* they are *magnetically anisotropic*. For example a compass needle always tries to point along the streamlines of the earth's magnetic field (see Fig. 2.4). In other words, for the needle it is energetically favorable to be magnetized along the south-north-axis of the needle.

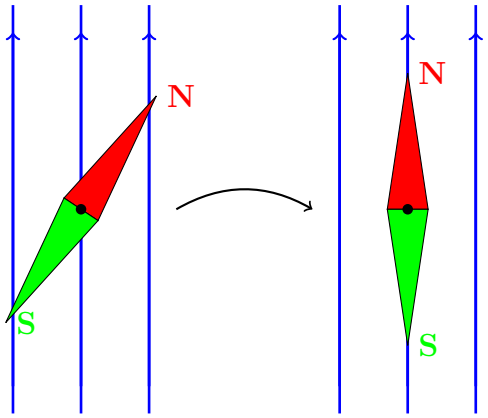

Fig. 2.4: In the earth's magnetic field a compass needle always orients itself along the magnetic streamlines (blue arrows).

On an atomic scale, the magnetic moments at the lattice site prefer to point along a certain direction, the so-called *easy axis*, whereas their rotation into a different direction costs energy. Perpendicular to the easy axis, the *hard axis* defines the magnetization direction with the highest energetic cost. The direction that is perpendicular to both, easy and hard axis, is named *medium axis*. As indicator of the strength of the magnetization preference, one can determine the *magnetic anisotropy energy* (MAE), that is the energy difference of the arrangements with magnetic moments pointing into hard and easy axis.

In the following, two contributions to the MAE will be discussed. One of them is due to the macroscopic form of the sample and is described from a classical point of view leading to the *magnetic shape anisotropy* (MSA) energy. The second term origins from the anisotropic arrangement of atoms within the crystal and is called *magnetocrystalline anisotropy* (MCA). The MCA only occurs in the presence of SOC.

The Magnetic Shape Anisotropy

The magnetic field of a dipole moment $\mathbf{m}_i$ positioned at $\mathbf{R}_i$ is given by

$$\mathbf{B}_i(\mathbf{r}) = -\frac{\mu_\mathrm{B}^2}{2}\frac{1}{r_i^5}\left[r_i^2\mathbf{m}_i - 3\left(\mathbf{r}_i\cdot\mathbf{m}_i\right)\mathbf{r}_i\right] , \tag{2.13}$$

with the Bohr magneton μ_B and $\mathbf{r}_i = \mathbf{r} - \mathbf{R}_i$. A second dipole moment $\mathbf{m}_j$ located at $\mathbf{R}_j$ interacts with the field and gives rise to the dipole-dipole energy

$$\begin{aligned} E_{dd}(\mathbf{R}_i,\mathbf{R}_j) &= -\mathbf{B}_i(\mathbf{R}_j)\cdot\mathbf{m}_j \\ &= \frac{\mu_\mathrm{B}^2}{2}\frac{1}{r_{ij}^5}\left[r_{ij}^2\mathbf{m}_i\cdot\mathbf{m}_j - 3\left(\mathbf{r}_{ij}\cdot\mathbf{m}_i\right)\left(\mathbf{r}_{ij}\cdot\mathbf{m}_j\right)\right] , \end{aligned} \tag{2.14}$$

with $\mathbf{r}_{ij} = \mathbf{R}_j - \mathbf{R}_i$. If both moments are pointing in the same direction, as it is the case in a ferromagnet, the term can be simplified to

$$E_{dd}(\mathbf{R}_i, \mathbf{R}_j) = \frac{\mu_\mathrm{B}^2}{2} \frac{1}{r_{ij}^3} m_i m_j \left[1 - 3\cos^2\Theta\right] , \tag{2.15}$$

where Θ represents the angle between $\mathbf{m}_i$ and $\mathbf{r}_{ij}$.

For monatomic chains, the difference between the energies of in-chain and out-of-chain directions is given by [35]

$$\begin{aligned} \Delta E_{dd} &= \frac{\mu_\mathrm{B}^2}{2} \left(2 \sum_{j=1}^{\infty} \frac{1}{j^3} \right) \frac{m^2}{a_\mathrm{c}^3} 3 \left[\cos^2 0 - \cos^2 \frac{\pi}{2} \right] \\ &\approx \frac{3 \cdot 1.202057}{137.036^2} \frac{m^2}{a_\mathrm{c}^3} < 0.1 \frac{\mathrm{meV}}{\mathrm{atom}} , \end{aligned} \tag{2.16}$$

with a typical magnetic moment $m = 2\,\mu_\mathrm{B}$ and a nearest-neighbor distance within the chain of $a_\mathrm{c} = 5.3\,a_\mathrm{B}$ with the Bohr radius a_B, which is comparable to the value used in the investigated structure (*cf.* Chs. 6 and 7). In this thesis ΔE_{dd} can be neglected against the corresponding MCA value, as the latter is more than 10 times larger.

The Magnetocrystalline Anisotropy

The MCA depends on the spins' direction within the crystal, which only influences the structure's total energy if SOC is taken into account. In the following it is assumed that the spins point parallel to each other along a certain direction. The MCA of such a collinear spin structure is closely related to the symmetry of the investigated system. Especially at surface structures, that normally exhibit less symmetries compared to the corresponding bulk structure, additional contributions to the anisotropy energy are expected to appear [36].

Since for a static system this energy term only depends on the direction of the (normed) magnetization $\mathbf{m}$, Akulov [37] proposed to expand the energy in components of $\mathbf{m}$:

$$E_\mathrm{MCA}(\mathbf{m}) = \mathsf{k}_0 + \sum_\alpha \mathsf{k}_\alpha m_\alpha + \sum_{\alpha,\beta} \mathsf{k}_{\alpha\beta} m_\alpha m_\beta + \sum_{\alpha,\beta,\gamma} \mathsf{k}_{\alpha\beta\gamma} m_\alpha m_\beta m_\gamma + \dots , \tag{2.17}$$

where $\mathbf{m} = (m_x, m_y, m_z)^\mathrm{T}$ and $\alpha, \beta, \gamma, \dots \in \{x, y, z\}$. Due to the time-inversion symmetry within a static system, the anisotropy energy is invariant with respect to spin inversion. The operator of spin inversion applied to all energy states causes a change of the magnetization's sign,

$$\mathbf{m}(\mathbf{r}) \xrightarrow[\text{spin inversion}]{} -\mathbf{m}(\mathbf{r}) . \tag{2.18}$$

Thus, all terms in Eq. (2.17) containing an odd number of magnetization components must vanish, so that $\mathsf{k}_\alpha = \mathsf{k}_{\alpha\beta\gamma} = \dots = 0$. In the following we will concentrate on

anisotropy contributions up to the second order. Higher order terms are not considered within this thesis, as they describe fast oscillations with respect to the magnetization direction and play a minor role in low-symmetric systems such as the regarded one. Since $\mathsf{k}_{\alpha\beta} = \mathsf{k}_{\beta\alpha}$, the energy is given by

$$\begin{aligned} E_{\mathrm{MCA}}(\mathbf{m}) &= \mathsf{k}_0 + \mathsf{k}_{x,x} m_x^2 + \mathsf{k}_{y,y} m_y^2 + \mathsf{k}_{z,z} m_z^2 \\ &\quad + 2\mathsf{k}_{x,y} m_x m_y + 2\mathsf{k}_{x,z} m_x m_z + 2\mathsf{k}_{y,z} m_y m_z + \mathcal{O}(m_\alpha^4)\,. \end{aligned} \tag{2.19}$$

As already discussed in Section 2.2.1, the investigated step-edged structure contains a mirror-plane perpendicular to the y-direction. This simplifies Eq. (2.19), due to the fact that every term containing an odd number of m_y has to be zero. Thus, the magnetocrystalline anisotropy up to the second order in m_α reads

$$E_{\mathrm{MCA}}(\mathbf{m}) = \mathbf{m}^{\mathrm{T}} \underbrace{(\mathsf{k}_0 \underline{\mathbb{1}} + \underline{\mathsf{k}})}_{=\underline{\mathsf{K}}} \mathbf{m}\,, \quad \text{with } \underline{\mathsf{k}} = \begin{pmatrix} \mathsf{k}_{x,x} & 0 & \mathsf{k}_{x,z} \\ 0 & \mathsf{k}_{y,y} & 0 \\ \mathsf{k}_{x,z} & 0 & \mathsf{k}_{z,z} \end{pmatrix}. \tag{2.20}$$

The anisotropy tensor of order 2, $\underline{\mathsf{K}}$, is symmetric and thus can be transformed into a diagonal form using a rotation matrix $\underline{\mathsf{U}}$,

$$\begin{pmatrix} \mathsf{K}_1 & 0 & 0 \\ 0 & \mathsf{K}_2 & 0 \\ 0 & 0 & \mathsf{K}_3 \end{pmatrix} = \begin{pmatrix} \mathsf{k}_0 + \mathsf{k}_1 & 0 & 0 \\ 0 & \mathsf{k}_0 + \mathsf{k}_2 & 0 \\ 0 & 0 & \mathsf{k}_0 + \mathsf{k}_3 \end{pmatrix} = \mathsf{k}_0 \underline{\mathbb{1}} + \underline{\mathsf{U}}\, \underline{\mathsf{k}}\, \underline{\mathsf{U}}^{\dagger}\,. \tag{2.21}$$

with the principal components K_1, K_2 and K_3. The constant k_0 is arbitrary, since it does not depend on the direction of $\mathbf{m}$. In most cases it is set to $\mathsf{k}_0 = -\frac{1}{3}\mathsf{tr}[\underline{\mathsf{k}}]$, in order to have a traceless anisotropy tensor in agreement with K_{ij} in Eq. (2.8). However, in preparation for Section 2.3 the definition

$$\mathsf{k}_0 = -\min\{\mathsf{k}_1, \mathsf{k}_2, \mathsf{k}_3\} \tag{2.22}$$

is used, so that the MCA vanishes if the spin moments point along the easy axis.

2.2.3 Higher-order terms

Of course it is possible to include exchange interactions that incorporate higher order terms such as four-particle interactions. Considering the Hubbard model [38, 39] a perturbative expansion up to the second order yields the Heisenberg model. However, if terms of higher order are taken into account additional contributions appear, *i.e.* the four-spin exchange interaction

$$H_{4-\mathrm{spin}} = -\sum_{i,j,k,l} K_{ijkl} \left[(\mathbf{S}_i \cdot \mathbf{S}_j)(\mathbf{S}_k \cdot \mathbf{S}_l) + (\mathbf{S}_j \cdot \mathbf{S}_k)(\mathbf{S}_l \cdot \mathbf{S}_i) - (\mathbf{S}_i \cdot \mathbf{S}_k)(\mathbf{S}_j \cdot \mathbf{S}_l) \right] \tag{2.23}$$

and the bi-quadratic exchange interaction

$$H_{\mathrm{bi-quadr}} = -\sum_{i,j} B_{ij} ((\mathbf{S}_i \cdot \mathbf{S}_j))^2\,. \tag{2.24}$$

Whereas the latter contribution describes a two-spin interaction of higher order, the four-spin exchange term incorporates the interaction among spins of four different lattice sites. These interactions can give rise to so-called multi-**Q** states, which are superpositions of symmetry equivalent spin-spirals and are believed to appear in several triangular monolayer structures, for example Mn/Cu(111) [40] or Fe/Rh(111) [41]. Although it cannot be excluded in the first place that their impact is not negligible in a one-dimensional structure with spatially slowly rotating spins, it is beyond the scope of this thesis to investigate their influence on the magnetic ground state. Instead, we will focus on the interaction terms that appear in Eq. (2.10).

2.3 The Micromagnetic Model

The magnetic ground state of a spin system usually is the result of an interplay of different contributions to the energy. If two contributions prefer differing spin alignments, this interplay can give rise to so-called *frustrated* spin structures. The effect of frustration can occur in systems with a non-vanishing DMI, which has been reported in low-dimensional antiferromagnetic structures [4, 42].

As pointed out in Section 2.2.1, the DMI favors canted spin structures of a particular rotational sense. Due to its relativistic origin, however, this SOC-driven effect is expected to cause only a small change in energy. Competing with the (usually strong) symmetric Heisenberg-type exchange interaction, that favors collinear spin alignments, the search for spin spiral structures can be restricted to those with a long-ranged periodicity $|\lambda| \gg a$, where a is the lattice constant. Another counter-role to the DMI play magnetic anisotropy effects, that describe the energetic costs when spin moments are rotated out of the easy axis into another direction. Only if the DMI is strong enough, *i.e.* in inversion asymmetric systems that exhibit a strong SOC within the substrate atoms, these barriers can be overcome, so that a non-collinear magnetic ground state occurs.

For the investigation of these mesoscale magnetic structures with a long-ranged periodicity, it is advisable to take advantage of slowly varying spin moments $\{\mathbf{S}_j\}$ by using a micromagnetic model as proposed for example by Döring [43]. Here, the spin vectors are replaced by a continuous function $\mathbf{m}(\mathbf{r})$, that fulfills $|\mathbf{m}| \equiv 1$ and $\mathbf{m}(\mathbf{R}_j) = \mathbf{S}_j$.[3] In a scenario of slowly rotating spin moments, it is justifiable to use a Taylor expansion for their Cartesian components in the vicinity of $\mathbf{R}_j$,

$$m_k(\mathbf{r}) \approx m_k(\mathbf{R}_j) + (\mathbf{r} - \mathbf{R}_j) \cdot \boldsymbol{\nabla} m_k(\mathbf{r})|_{\mathbf{r}=\mathbf{R}_j} \quad , \; k \in \{x, y, z\} \, . \tag{2.25}$$

Therefore, the difference of two magnetic moments at lattice sites $\mathbf{R}_i$ and $\mathbf{R}_j$, that are not too far apart from each other, is expressed by

$$m_k(\mathbf{R}_i) - m_k(\mathbf{R}_j) \approx (\mathbf{R}_i - \mathbf{R}_j) \cdot \boldsymbol{\nabla} m_k(\mathbf{R}_j) \propto \dot{m}_k(\mathbf{R}_j) \, , \tag{2.26}$$

[3] Note, that this definition is applicable to (nearly) antiferromagnetic structures as well, where $\mathbf{m}(r)$ is orientated anti-parallel to every second $\mathbf{S}_j$, *e.g.* $\mathbf{m}(\mathbf{R}_j) = (-1)^j \mathbf{S}_j$. The resulting $\mathbf{q}$-vector is shifted by $0.5 \cdot 2\pi/a_c$ along the rotation direction, so that $\mathbf{q} = 0$ describes the antiferromagnetic spin order.

with $\dot{m}_k = \frac{\partial m_k}{\partial r}$. The energy as a functional of the magnetic moment $\mathbf{m} = \mathbf{m}(\mathbf{r})$ is given by

$$\begin{aligned} E[\mathbf{m}] &= \int \mathrm{d}^3 r' \left[\tilde{\mathsf{A}} \dot{\mathbf{m}}^2 + \tilde{\mathbf{D}} \cdot (\mathbf{m} \times \dot{\mathbf{m}}) + \mathbf{m}^{\mathrm{T}} \underline{\mathsf{K}} \mathbf{m} \right] \\ &= \int \mathrm{d}^3 r' \left[\frac{\mathsf{A}}{4\pi^2} \dot{\mathbf{m}}^2 + \frac{\mathbf{D}}{2\pi} \cdot (\mathbf{m} \times \dot{\mathbf{m}}) + \mathbf{m}^{\mathrm{T}} \underline{\mathsf{K}} \mathbf{m} \right] \quad , \ \mathbf{m} = \mathbf{m}(\mathbf{r}') \,. \end{aligned} \tag{2.27}$$

Here, the sum of Eq. (2.10) is replaced by an integral over space and the reformulations

$$\begin{aligned} 1 - \mathbf{S}_i \cdot \mathbf{S}_j = \frac{1}{2} (\mathbf{S}_i - \mathbf{S}_j)^2 \to \frac{1}{2} (\mathbf{m}(\mathbf{R}_i) - \mathbf{m}(\mathbf{R}_j))^2 &\propto \dot{\mathbf{m}}(\mathbf{R}_j)^2 \\ -\mathbf{S}_i \times \mathbf{S}_j = \mathbf{S}_i \times (\mathbf{S}_i - \mathbf{S}_j) & \\ \to \mathbf{m}(\mathbf{R}_i) \times (\mathbf{m}(\mathbf{R}_i) - \mathbf{m}(\mathbf{R}_j)) &\propto \mathbf{m}(\mathbf{R}_i) \times \dot{\mathbf{m}}(\mathbf{R}_j) \end{aligned} \tag{2.28}$$

have been used. The (constant) model parameter $\tilde{\mathsf{A}}$ is called spin stiffness constant and its contribution to the energy origins from the Heisenberg-type interaction [44]. The index-free Dzyaloshinskii-vector $\tilde{\mathbf{D}}$ describes the averaged contribution to the energy that comes from the DMI. For reasons that will become clear later (*cf.* Sec. 2.3.1) we will proceed by using the parameters $\mathsf{A} = 4\pi^2 \tilde{\mathsf{A}}$ and $\mathsf{D} = 2\pi \tilde{\mathsf{D}}$ that represent the corresponding quantities normalized to one period length of a spiral rotation. Finally, the anisotropy tensor $\underline{\mathsf{K}}$ denotes the anisotropy effects within the crystal.

The derived ansatz within the micromagnetic model, *cf.* Eq. (2.27), will now be used to describe cycloidal spin spirals. Regarding the chemical structure of the investigated system (*cf.* Fig. 2.5), it is assumed to have knowledge of the model parameters

$$\mathsf{A} \quad , \quad \mathbf{D} = \begin{pmatrix} D_x \\ 0 \\ D_z \end{pmatrix} \quad , \quad \underline{\mathsf{K}} = \begin{pmatrix} \mathsf{K}_{11} & 0 & \mathsf{K}_{13} \\ 0 & \mathsf{K}_{22} & 0 \\ \mathsf{K}_{13} & 0 & \mathsf{K}_{33} \end{pmatrix} = \underline{\mathsf{U}}_\alpha^\dagger \begin{pmatrix} \mathsf{K}_1 & 0 & 0 \\ 0 & \mathsf{K}_2 & 0 \\ 0 & 0 & \mathsf{K}_3 \end{pmatrix} \underline{\mathsf{U}}_\alpha \,. \tag{2.29}$$

Here, already the symmetry of the chain structure is contributed to by accounting for the mirror plane perpendicular to the chain direction (along the y-axis), so that $D_y = 0$. The entries of the anisotropy matrix $\underline{\mathsf{K}}$ are connected to the anisotropies along easy, medium and hard axis, the principal components K_1, K_2 and K_3, via the rotation matrix

$$\underline{\mathsf{U}}_\alpha = \begin{pmatrix} \cos\alpha & 0 & -\sin\alpha \\ 0 & 1 & 0 \\ \sin\alpha & 0 & \cos\alpha \end{pmatrix} \tag{2.30}$$

and read

$$\begin{aligned} \mathsf{K}_{11} &= \mathsf{K}_1 \cos^2\alpha + \mathsf{K}_3 \sin^2\alpha \,, \\ \mathsf{K}_{13} &= (\mathsf{K}_3 - \mathsf{K}_1) \sin\alpha \cdot \cos\alpha \,, \\ \mathsf{K}_{22} &= \mathsf{K}_2 \\ \text{and} \quad \mathsf{K}_{33} &= \mathsf{K}_1 \sin^2\alpha + \mathsf{K}_3 \cos^2\alpha \,, \end{aligned} \tag{2.31}$$

where α is the angle between the x-axis and the direction of the principal component K_1. Note that the principal component pointing into easy axis direction is set to zero.

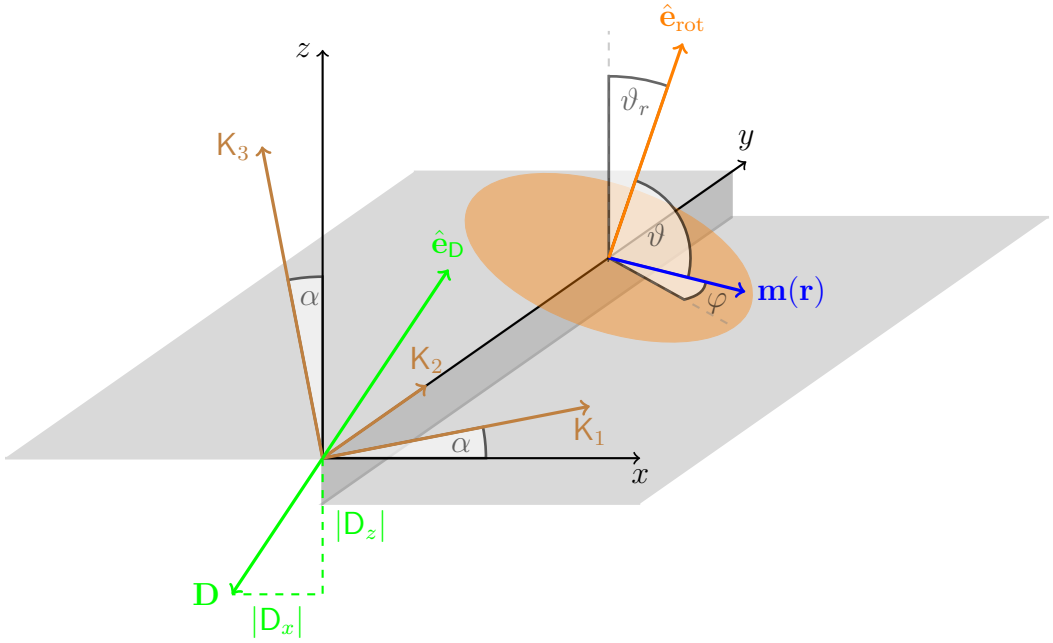

Fig. 2.5: The step-edge structure with the Dzyaloshinskii-vector $\mathbf{D}$ and the principal axes K_1, K_2 and K_3 of the anisotropy matrix $\underline{\mathsf{K}}$ with respect to the used coordinate system. Note that the principal component pointing along the easy axis can be chosen to be zero, due to an arbitrary energy offset within the anisotropy contribution. In the background, the rotation axis $\hat{\mathbf{e}}_{\mathrm{rot}}$ with respect to the z-direction is shown as well as one representing vector of the magnetization $\mathbf{m}(\mathbf{r})$, which is dependent on the function $\varphi = \varphi(y)$. The cone-angle ϑ (here: $\vartheta = \frac{\pi}{2}$) is not to confuse with ϑ_r, the angle between the z-axis and $\hat{\mathbf{e}}_{\mathrm{rot}}$.

The following analysis will be restricted to flat spirals only, which means that $\vartheta = \frac{\pi}{2}$. Assuming that the rotation axis $\hat{\mathbf{e}}_{\mathrm{rot}} = (\sin\vartheta_r, 0, \cos\vartheta_r)^{\mathrm{T}}$ of the spiral and the z-axis enclose the angle ϑ_r, the magnetization direction along the chain and its derivative are given by

$$\mathbf{m}(y) = \begin{pmatrix} \cos\vartheta_r & 0 & \sin\vartheta_r \\ 0 & 1 & 0 \\ -\sin\vartheta_r & 0 & \cos\vartheta_r \end{pmatrix} \begin{pmatrix} \cos\varphi \\ \sin\varphi \\ 0 \end{pmatrix} = \begin{pmatrix} \cos\vartheta_r \cdot \cos\varphi \\ \sin\varphi \\ -\sin\vartheta_r \cdot \cos\varphi \end{pmatrix}, \tag{2.32}$$

$$\dot{\mathbf{m}}(y) = \dot{\varphi} \cdot \frac{\mathrm{d}\mathbf{m}(y)}{\mathrm{d}\varphi} = \dot{\varphi} \cdot \begin{pmatrix} -\cos\vartheta_r \cdot \sin\varphi \\ \cos\varphi \\ \sin\vartheta_r \cdot \sin\varphi \end{pmatrix}, \tag{2.33}$$

with the monotonic function $\varphi = \varphi(y)$ and $\dot{\varphi} = \frac{\mathrm{d}\varphi}{\mathrm{d}y}$. Inserting this into Eq. (2.27), the energy functional is given by

$$E[\varphi] = \int \mathrm{d}y \left[\frac{\mathsf{A}}{4\pi^2}\dot{\varphi}^2 + \frac{\mathsf{D}_r}{2\pi}\dot{\varphi} + \mathsf{K}_\perp \cos^2\varphi + \mathsf{K}_2 \sin^2\varphi \right] \tag{2.34}$$

The expression $\mathsf{D}_r = \mathbf{D}\cdot\hat{\mathbf{e}}_{\mathrm{rot}} = D_x \sin\vartheta_r + D_z \cos\vartheta_r$ is the projection of the Dzyaloshinskii-vector on the rotation axis, $\mathsf{K}_\perp = \mathsf{K}_{11}\cos^2\vartheta_r + \mathsf{K}_{33}\sin^2\vartheta_r + 2\mathsf{K}_{13}\cos\vartheta_r\sin\vartheta_r$ denotes the

energetic costs due to the magnetic anisotropy, when the spins are pointing perpendicular to both, $\hat{\mathbf{e}}_{\mathrm{rot}}$ and $\hat{\mathbf{e}}_y$, the propagation direction of the spiral. Due to the only asymmetric part in Eq. (2.34) with respect to φ, the rotational sense of a possible spiral minimizing Eq. (2.34) is connected to the sign of D_r, *i.e.* $\mathsf{D}_r < 0 \Leftrightarrow \dot{\varphi} > 0$ and *vice versa*. The energy for a period length λ is given by

$$\begin{aligned} E_\lambda[\varphi] &= \frac{1}{\lambda}\left(E[\varphi(\lambda)] - E[\varphi(0)]\right) \\ &= \frac{1}{\lambda}\int_0^\lambda \mathrm{d}y \left[\frac{\mathsf{A}}{4\pi^2}\dot{\varphi}^2 + \frac{\mathsf{D}_r}{2\pi}\dot{\varphi} + \mathsf{K}_\perp \cos^2\varphi + \mathsf{K}_2 \sin^2\varphi\right] \\ &= \frac{1}{\lambda}\int_0^{2\pi} \mathrm{d}\varphi \left[\frac{\mathsf{A}}{4\pi^2}\dot{\varphi} + \frac{\mathsf{D}_r}{2\pi} + \left(\mathsf{K}_\perp \cos^2\varphi + \mathsf{K}_2 \sin^2\varphi\right)\dot{\varphi}^{-1}\right] . \end{aligned} \tag{2.35}$$

2.3.1 Homogeneous Spin Spirals

In the case of a homogeneous spin spiral, the rotation angle φ is linear dependent on the distance in chain direction,

$$\varphi(y) = \frac{2\pi}{\lambda}\cdot y\,. \tag{2.36}$$

This simplifies Eq. (2.35) to a function that shows a parabolic behavior with respect to λ^{-1},

$$\begin{aligned} E_\lambda &= \frac{1}{\lambda}\int_0^{2\pi} \mathrm{d}\varphi \left[\frac{\mathsf{A}}{4\pi^2}\frac{2\pi}{\lambda} + \frac{\mathsf{D}_r}{2\pi} + \left(\mathsf{K}_\perp \cos^2\varphi + \mathsf{K}_2 \sin^2\varphi\right)\frac{\lambda}{2\pi}\right] \\ &= \mathsf{A}\lambda^{-2} + \mathsf{D}_r\lambda^{-1} + \frac{1}{2}\left(\mathsf{K}_\perp + \mathsf{K}_2\right) . \end{aligned} \tag{2.37}$$

Using the abbreviation $\overline{\mathsf{K}} = \left(\mathsf{K}_\perp + \mathsf{K}_2\right)/2$, the averaged anisotropic energy costs a rotating spiral structure claims, the minimal energy value E_{min} and the corresponding period length λ_{min} read

$$E_{\mathrm{min}} = E_{\lambda_{\mathrm{min}}} = -\frac{\mathsf{D}_r^2}{4\mathsf{A}} + \overline{\mathsf{K}} \quad , \text{ with } \lambda_{\mathrm{min}} = -2\frac{\mathsf{A}}{\mathsf{D}_r}\,. \tag{2.38}$$

In the case of a collinear magnetic structure of spins that are pointing into the easy axis direction, the energy functional vanishes. Therefore a non-collinear (homogeneous) spiral structure is established as the magnetic ground state only if the inequality $E_{\mathrm{min}} < 0$ is fulfilled. This leads to the criterion for the appearance of a homogeneous spin spiral,

$$\frac{\mathsf{D}_r^2}{\mathsf{A}\overline{\mathsf{K}}} \overset{!}{>} 4\,. \tag{2.39}$$

In Fig. 2.6 an example is shown, in which this criterion is fulfilled, as the minimum of the parabola E_λ is less than zero. As already discussed in Section 2.2.1, the slope of the DMI prefers a spiral of a unique sense of rotation, which – in the shown case in Fig. 2.6 – results in a left-handed ($\lambda_{\mathrm{min}} < 0$) spiral.

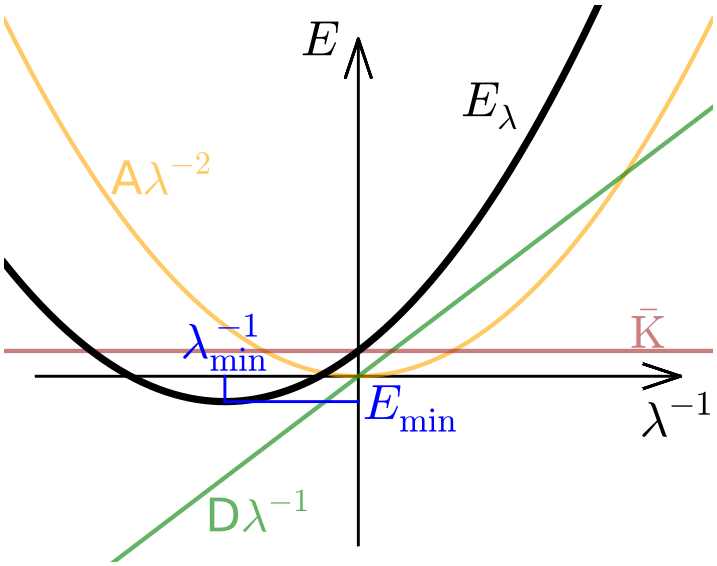

Fig. 2.6: The black curve is the energy as a function of the (inverse) period length. In this case we have a ground state of a spin spiral, due to the fact that the criterion in Eq. (2.39) is fulfilled.

2.3.2 Inhomogeneous Spin Spirals

In the previous Section 2.3.1 a criterion was derived that allows to predict whether the ground state of a magnetic system forms a (homogeneous) spiral structure or a collinear spin alignment. In the following, the approximation from Eq. (2.36) is dropped. By replacing $\dot{\varphi} = (\mathrm{d}y/\mathrm{d}\varphi)^{-1} = 1/y'$, the energy of an inhomogeneous spiral (see Eq. (2.35)) structure within a period length λ reads

$$E_\lambda = \frac{1}{\lambda}\int_0^{2\pi} \mathrm{d}\varphi \underbrace{\left[\frac{\mathsf{A}}{4\pi^2}\frac{1}{y'} + \frac{\mathsf{D}_r}{2\pi} + g_{\mathsf{K}_\perp,\mathsf{K}_2}(\varphi)y'\right]}_{=f(y,y')} \tag{2.40}$$

$$\text{with} \quad g_{\mathsf{K}_\perp,\mathsf{K}_2}(\varphi) = \mathsf{K}_\perp \cos^2\varphi + \mathsf{K}_2 \sin^2\varphi = \mathsf{K}_{\max} - (\mathsf{K}_{\max} - \mathsf{K}_{\min})\sin^2(\varphi+\varphi_0) \geq \mathsf{K}_{\min}\,, \tag{2.41}$$

where the expressions

$$\begin{array}{rcl} \mathsf{K}_{\min} & = & \min\{\mathsf{K}_\perp, \mathsf{K}_2\} \geq 0\,, \\ \mathsf{K}_{\max} & = & \max\{\mathsf{K}_\perp, \mathsf{K}_2\} \geq \mathsf{K}_{\min} \end{array} \quad \text{and} \quad \varphi_0 = \begin{cases} 0 & , \mathsf{K}_\perp \geq \mathsf{K}_2 \\ \frac{\pi}{2} & , \mathsf{K}_\perp < \mathsf{K}_2 \end{cases} \tag{2.42}$$

have been used. Within the rotation plane of the spiral, $\mathsf{K}_{\min}$ is the direction of lowest energetic costs, the local easy axis so to speak. Thus, if the (global) easy axis is placed within the spiral rotation plane, its value is zero, $\mathsf{K}_{\min} = 0$. The function $g_{\mathsf{K}_\perp,\mathsf{K}_2}(\varphi)$ is introduced to ensure the readability of the following equations.

Although the solution of Eq. (2.40) is not straightforward to derive compared to the investigated homogeneous spiral structures, it is still possible to name a criterion for the appearance of an inhomogeneous flat spiral. The following derivation is partly build upon scientific contributions by Dzyaloshinskii [45] as well as Izyumov [46]. Within the Euler-Lagrange formalism

$$0 \stackrel{!}{=} \frac{\mathrm{d}}{\mathrm{d}\varphi}\frac{\partial f(y,y')}{\partial y'} - \frac{\partial f(y,y')}{\partial y} = \frac{\mathrm{d}}{\mathrm{d}\varphi}\underbrace{\left[-\frac{\mathsf{A}}{4\pi^2}\frac{1}{y'^2} + g_{\mathsf{K}_\perp,\mathsf{K}_2}(\varphi)\right]}_{=-c\stackrel{!}{=}\text{const.}} \tag{2.43}$$

a closed expression for $y(\varphi)$ and its derivative with respect to φ, $y'(\varphi)$, can be derived:

$$y(\varphi) = \pm\frac{\sqrt{\mathsf{A}}}{2\pi}\int_0^\varphi \mathrm{d}\tilde{\varphi}\,(c + g_{\mathsf{K}_\perp,\mathsf{K}_2}(\tilde{\varphi}))^{-\frac{1}{2}}\ , \tag{2.44}$$

$$y'(\varphi) = \pm\frac{\sqrt{\mathsf{A}}}{2\pi}\,(c + g_{\mathsf{K}_\perp,\mathsf{K}_2}(\varphi))^{-\frac{1}{2}}\ , \tag{2.45}$$

with the constant $c > -\mathsf{K}_{\min}$. The lower integration boundary of $y(\varphi)$ is chosen such, that $y(0) = 0$. Thus, the energy E_λ and the period length $\lambda = y(2\pi)$ take the form

$$E_\lambda = \pm\frac{\sqrt{\mathsf{A}}}{2\pi\lambda}\int_0^{2\pi}\mathrm{d}\varphi\frac{c + 2g_{\mathsf{K}_\perp,\mathsf{K}_2}(\varphi)}{(c + g_{\mathsf{K}_\perp,\mathsf{K}_2}(\varphi))^{\frac{1}{2}}} + \frac{1}{\lambda}\mathsf{D}_r\,, \tag{2.46}$$

$$\lambda = \pm\frac{\sqrt{\mathsf{A}}}{2\pi}\int_0^{2\pi}\mathrm{d}\tilde{\varphi}\,(c + g_{\mathsf{K}_\perp,\mathsf{K}_2}(\tilde{\varphi}))^{-\frac{1}{2}}\ . \tag{2.47}$$

Similar to the procedure in Section 2.3.1 it is now the next step to find the period length that minimizes the energy. Since E_λ as well as λ can be considered as functions of the parameter c, the minimum value is reached, when

$$\begin{aligned} 0 \stackrel{!}{=} \frac{\mathrm{d}E_\lambda}{\mathrm{d}c} &= -\frac{E_\lambda}{\lambda}\frac{\mathrm{d}\lambda}{\mathrm{d}c} \pm \frac{\sqrt{\mathsf{A}}}{2\pi\lambda}\int_0^{2\pi}\mathrm{d}\varphi\left[\frac{1}{(c + g_{\mathsf{K}_\perp,\mathsf{K}_2}(\varphi))^{\frac{1}{2}}} - \frac{1}{2}\frac{c + 2g_{\mathsf{K}_\perp,\mathsf{K}_2}(\varphi)}{(c + g_{\mathsf{K}_\perp,\mathsf{K}_2}(\varphi))^{\frac{3}{2}}}\right] \\ &= -\frac{E_\lambda}{\lambda}\frac{\mathrm{d}\lambda}{\mathrm{d}c} - \frac{c}{\lambda}\cdot\underbrace{\left(\mp\frac{1}{2}\frac{\sqrt{\mathsf{A}}}{2\pi}\int_0^{2\pi}\mathrm{d}\varphi\,(c + g_{\mathsf{K}_\perp,\mathsf{K}_2}(\varphi))^{-\frac{3}{2}}\right)}_{=\frac{\mathrm{d}\lambda}{\mathrm{d}c}} \\ &= -\underbrace{\frac{1}{\lambda}\frac{\mathrm{d}\lambda}{\mathrm{d}c}}_{\neq 0}(E_\lambda + c) \end{aligned} \tag{2.48}$$

Thus, the minimal value of the spiral's energy is given by $E_\lambda = -c$. This means, that a spiral structure is only energetically more favorable than the collinear ground state $E = 0$ if $c > 0$. At last, the constant c must be put into a relationship with the

parameters that describe the system. Since (use Eqs. (2.46) and 2.47))

$$\begin{aligned}\lambda \cdot (E_\lambda + c) &= \pm\frac{\sqrt{\mathsf{A}}}{2\pi}\int_0^{2\pi} \mathrm{d}\varphi \left[\frac{c + 2g_{\mathsf{K}_\perp,\mathsf{K}_2}(\varphi)}{(c + g_{\mathsf{K}_\perp,\mathsf{K}_2}(\varphi))^{\frac{1}{2}}} + \frac{c}{(c + g_{\mathsf{K}_\perp,\mathsf{K}_2}(\varphi))^{\frac{1}{2}}}\right] + \mathsf{D}_r \\ &= \pm 2\frac{\sqrt{\mathsf{A}}}{2\pi}\int_0^{2\pi} \mathrm{d}\varphi\,(c + g_{\mathsf{K}_\perp,\mathsf{K}_2}(\varphi))^{\frac{1}{2}} + \mathsf{D}_r \end{aligned} \tag{2.49}$$

is equal to zero for the spiral structure with the lowest energy value, the model parameters and the constant c are connected via the formula

$$\begin{aligned}|\mathsf{D}_r| &= \frac{\sqrt{\mathsf{A}}}{\pi}\int_0^{2\pi} \mathrm{d}\varphi\,(c + g_{\mathsf{K}_\perp,\mathsf{K}_2}(\varphi))^{\frac{1}{2}} \\ &> \frac{\sqrt{\mathsf{A}}}{\pi}\int_0^{2\pi} \mathrm{d}\varphi\,(g_{\mathsf{K}_\perp,\mathsf{K}_2}(\varphi))^{\frac{1}{2}} \\ &= 4\frac{\sqrt{\mathsf{A}\mathsf{K}_{\max}}}{\pi}\underbrace{\int_0^{\pi/2} \mathrm{d}\varphi \left(1 - \frac{\mathsf{K}_{\max} - \mathsf{K}_{\min}}{\mathsf{K}_{\max}}\sin^2(\varphi + \varphi_0)\right)^{\frac{1}{2}}}_{=\mathsf{E}\left(\sqrt{\frac{\mathsf{K}_{\max}-\mathsf{K}_{\min}}{\mathsf{K}_{\max}}}\right)} \end{aligned} \tag{2.50}$$

with the complete elliptic function of the second kind[4]

$$\mathsf{E}(\epsilon) = \int_0^{\pi/2} \mathrm{d}\varphi\left(1 - \epsilon^2\sin^2\varphi\right)^{\frac{1}{2}} \quad , \ |\epsilon| \le 1\,. \tag{2.51}$$

Using Eq. (2.50), the criterion for the appearance of an inhomogeneous spin spiral reads

$$\frac{\mathsf{D}_r^2}{\mathsf{A}\mathsf{K}_{\max}\left(\mathsf{E}\left(\sqrt{\frac{\mathsf{K}_{\max}-\mathsf{K}_{\min}}{\mathsf{K}_{\max}}}\right)\right)^2} \overset{!}{>} \frac{16}{\pi^2} \approx 1.62\,. \tag{2.52}$$

In the case of $\mathsf{K}_{\min} = 0$ (the easy axis points in a direction within the rotation plane of the spins) Eq. (2.52) is simplified due to $\mathsf{E}(1) = 1$. Furthermore if $\mathsf{K}_{\min} = \mathsf{K}_{\max}$ no direction within the spiral's rotation plane should be favored by the spins, so that the appearance of a homogeneous spiral is expected. Since $\mathsf{E}(0) = \frac{\pi}{2}$ and $\mathsf{K}_{\max} = \frac{1}{2}(\mathsf{K}_\perp + \mathsf{K}_2) = \overline{\mathsf{K}}$ in such a structure, indeed, the criterion in Eq. (2.52) becomes identical to Eq. (2.39).

The shape of the spiral structure, *i.e.* the function $\varphi(y)$, depends on the parameter

$$0 \le \epsilon = \sqrt{\frac{\mathsf{K}_{\max} - \mathsf{K}_{\min}}{\mathsf{K}_{\max} + c}} < 1 \qquad (\text{since } c > -\mathsf{K}_{\min})\,. \tag{2.53}$$

By using the Jacobian elliptic amplitude function

$$\mathsf{am}\left(\int_0^{\varphi} \mathrm{d}\tilde{\varphi}\left(1 - \epsilon^2\sin^2\tilde{\varphi}\right)^{-\frac{1}{2}}, \epsilon\right) = \varphi - z\cdot\pi\,, \quad \text{for } \varphi \in \left[z\cdot\pi - \frac{\pi}{2}, z\cdot\pi + \frac{\pi}{2}\right)\,, \tag{2.54}$$

[4]Note that in Eq. (2.51) the value of $\mathsf{E}(\epsilon)$ remains unchanged if $\cos^2\varphi$ was used instead of $\sin^2\varphi$. Thus a distinction caused by φ_0 is not necessary in Eq. (2.50).

where $\epsilon^2 < 1$ and $z \in \mathbb{Z}$, the shape of the spiral with the minimal energy ($c = -E_\lambda > -\mathsf{K}_{\min}$) takes the form

$$\begin{aligned}\varphi(y) &= \mathsf{am}\left(\pm 2\pi\sqrt{\frac{\mathsf{K}_{\max}+c}{\mathsf{A}}}\left(y - \frac{|\lambda|}{2\pi}\left(\frac{\pi}{2}-\varphi_0\right)\right), \epsilon\right) \pm \left(\frac{\pi}{2}-\varphi_0\right) + z\cdot\pi\,, \\ &\quad \text{for } y \in \left[(z\cdot\pi-\varphi_0)\cdot\frac{|\lambda|}{2\pi}, ((z+1)\cdot\pi-\varphi_0)\cdot\frac{|\lambda|}{2\pi}\right)\,. \end{aligned} \tag{2.55}$$

This formula distinguishes right- and left-handed spirals, as it is shown in Fig. 2.7. Depending on the system, *i.e.* whether $\mathsf{K}_{\max} = \mathsf{K}_\perp$ ($\Rightarrow \varphi_0 = 0$) or $\mathsf{K}_{\max} = \mathsf{K}_2$ ($\Rightarrow \varphi_0 = \frac{\pi}{2}$), the slope $\dot{\varphi}$ is such, that the spins along the chain prefer the direction of $\mathsf{K}_{\min}$. In the case of $\mathsf{K}_{\max} = \mathsf{K}_{\min}$ ($\Rightarrow \epsilon = 0$), the expression for the period length (*cf.* Eq. (2.47)) reads

$$\lambda_{\epsilon=0} = \pm\frac{\sqrt{\mathsf{A}}}{2\pi}\int_0^{2\pi} \mathrm{d}\tilde{\varphi}\,(c+\mathsf{K}_{\max})^{-\frac{1}{2}} = \pm\sqrt{\frac{\mathsf{A}}{\mathsf{K}_{\max}+c}}\,. \tag{2.56}$$

Thus, in this special case Eq. (2.44) can be simplified to

$$y(\varphi) = \pm\frac{\sqrt{\mathsf{A}}}{2\pi}\int_0^{\varphi} \mathrm{d}\tilde{\varphi}\,(c+\mathsf{K}_{\max})^{-\frac{1}{2}} = \pm\frac{1}{2\pi}\sqrt{\frac{\mathsf{A}}{\mathsf{K}_{\max}+c}}\cdot\varphi = \frac{\lambda_{\epsilon=0}}{2\pi}\varphi\,, \tag{2.57}$$

which leads directly to Eq. (2.36), the ansatz for $\varphi(y)$ in the case of a homogeneous spin spiral.

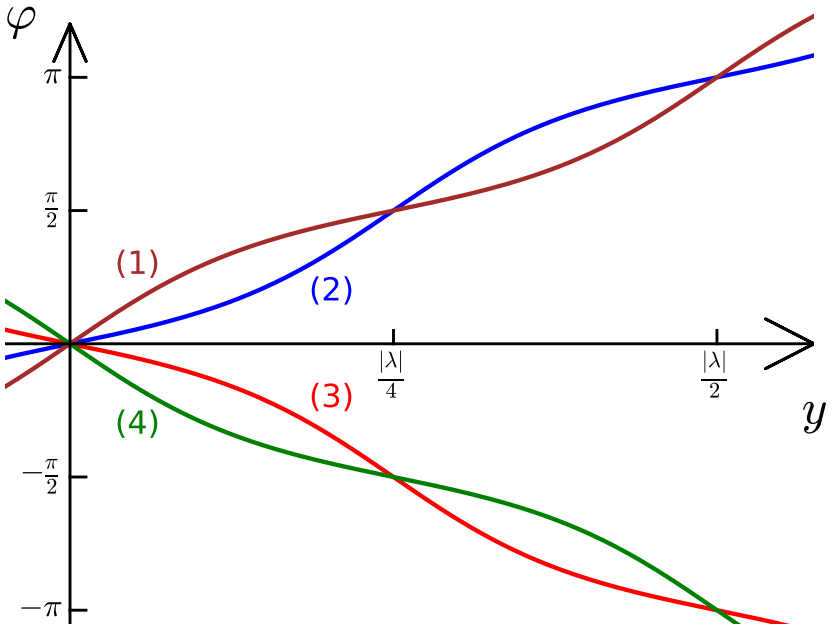

Fig. 2.7: The figure shows four examples of the function $\varphi(y)$ as it appears in an inhomogeneous spiral. Two right-handed spirals are indicated by the brown (1) and the blue (2) function, whereas the red (3) and green (4) curves follow the path of two left-handed spirals. In the cases (1) and (4), $\mathsf{K}_{\max} = \mathsf{K}_{\perp}$, so that the slope is steepest for $\varphi \in \{0, \pm\pi, \dots\}$. When elsewise $\mathsf{K}_{\max} = \mathsf{K}_2$ (as in the remaining cases (2) and (3)), the spins prefer the (local) easy axis within the plane, so that the slope is steepest for $\varphi \in \{\pm\frac{\pi}{2}, \pm\frac{3\pi}{2}, \dots\}$. For $\epsilon \nearrow 1$ ($c \searrow -\mathsf{K}_{\min}$) the preference of the easy axis is so strong, that it results in spin groups, that alternating point parallel and antiparallel along the easy axis. For $\epsilon \searrow 0$ ($\mathsf{K}_{\max} \searrow \mathsf{K}_{\min}$), (1) and (2) become identical (as well as (3) and (4)). Then, the resulting functions describe homogeneous spirals.

2.3.3 Phase Diagrams

Up to now, the investigation was restricted to flat spiral structures that rotate homogeneously or inhomogeneously along the chain direction. In order to account for anisotropy effects within a real crystal, however, it could be necessary to drop the constraint $\vartheta = \frac{\pi}{2}$. Thus, coned spirals ($\vartheta \neq \frac{\pi}{2}$) or 3D-spirals ($\vartheta = \vartheta(y)$), that allow a variation of the cone-angle within a period, provide an even larger field of possible magnetic phases. To explore the theoretical approach a more general ansatz compared to Eq. (2.27) has to be formulated. This investigation however, is beyond the scope of this thesis, so that the step-edged systems will be investigated only in terms of flat spiral structures.

A general overview of 3d-spin structures can be found in Ref. [47]. Here the investigation was performed assuming that the Dzyaloshinskii-vector is pointing along a high symmetry line within the crystal, *i.e.* a principal axis of the anisotropy tensor. This assumption is valid, only if the considered system exhibits two mirror-planes perpendicular

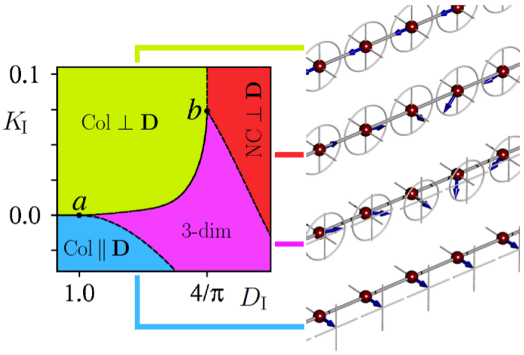

Fig. 2.8: An example for a phase diagram with two reduced parameters, a reduced Dzyaloshinskii-vector D_I and an reduced anisotropy contribution K_I, taken from [47].

to each other. This allows to assume

$$\mathbf{D} = \mathrm{D} \cdot \hat{\mathbf{e}}_z \quad \text{and} \quad \underline{\mathsf{K}} = \begin{pmatrix} \mathsf{K}_1 & 0 & 0 \\ 0 & \mathsf{K}_2 & 0 \\ 0 & 0 & \mathsf{K}_\mathrm{D} \end{pmatrix} . \tag{2.58}$$

In the case $\mathsf{K}_1 < \mathsf{K}_2$ (for a detailed case-by-case analysis, see *e.g.* Ref. [47]) the reduced parameters

$$\mathrm{D}_\mathrm{I} = \frac{\mathrm{D}}{\sqrt{A(\mathsf{K}_2 - \mathsf{K}_1)}} \quad \text{and} \quad \mathsf{K}_\mathrm{I} = \frac{\mathsf{K}_\mathrm{D} - \mathsf{K}_1}{\mathsf{K}_2 - \mathsf{K}_1} \tag{2.59}$$

are definable. In order to understand their interplay and influence on the magnetic ground state, a phase diagram can be created, as it is shown in Fig. 2.8. Obviously the non-collinear ground states dominate in the figure's right region, where D_I is largest.

3 The Density Functional Theory

In the previous Chapter 2 a simple micromagnetic model for spin structures on lattices was discussed. Within this model only a few parameters were found to be sufficient to give a prediction for a variety of magnetic orders of a magnetic system's ground state. These orders can be collinear (ferro-, ferri- or antiferromagnetic) or non-collinear (e.g. spin spirals). However, the question arises, how these physical quantities can be determined if a specific atomic structure is investigated. In addition it would be useful and enlightening to understand how certain properties of the system, such as the type of chemical elements occurring in the structure or the chosen lattice constant, enter the parameters and therefore affect the magnetic ground state.
For the description of a solid with a periodic structure the number N of particles can exceed a few hundred per unit cell. Then the treatment of such a many-body problem consisting of N_N nuclei and $N_\mathrm{e} = N - N_\mathrm{N}$ electrons is a formidable task, which cannot be accomplished using the "traditional" wave-function formalism for quantum-mechanical systems. To circumvent this problem a variety of concepts and methods have been developed up to this date, of which an important example, the *density functional theory* (DFT), will be introduced in this chapter.

When dealing with a static quantum-mechanical ground state problem, it is common to use the ansatz of the *time-independent Schrödinger equation*

$$H\Psi(\mathbf{R}_1, \ldots, \mathbf{R}_{N_\mathrm{N}}, \mathbf{r}_1, \ldots, \mathbf{r}_{N_\mathrm{e}}) = E\Psi(\mathbf{R}_1, \ldots, \mathbf{R}_{N_\mathrm{N}}, \mathbf{r}_1, \ldots, \mathbf{r}_{N_\mathrm{e}})\,, \tag{3.1}$$

with the many-body wave-function $\Psi(\mathbf{R}_1, \ldots, \mathbf{R}_{N_\mathrm{N}}; \mathbf{r}_1, \ldots, \mathbf{r}_{N_\mathrm{e}})$ and the corresponding eigenenergy E, where $\mathbf{R}_\mu$ and $\mathbf{r}_i$ assign the positions of the μth nucleus and the ith electron, respectively. Considering that each electron possesses the mass $\mathrm{m_e}$ and the negative of the elementary charge e, and that the μth nucleus has the mass M_μ and the atomic number Z_μ, the Hamiltonian H can be expressed in the form

$$H = -\sum_{\mu=1}^{N_\mathrm{N}} \frac{\hbar^2}{2\mathrm{M}_\mu} \boldsymbol{\nabla}_\mu^2 - \sum_{i=1}^{N_\mathrm{e}} \frac{\hbar^2}{2\mathrm{m_e}} \boldsymbol{\nabla}_i^2 + \frac{e^2}{4\pi\epsilon_0} \left[\sum_{\mu<\nu}^{N_\mathrm{N}} \frac{\mathrm{Z}_\mu \mathrm{Z}_\nu}{r_{\mu,\nu}} + \sum_{i<j}^{N_\mathrm{e}} \frac{1}{r_{i,j}} - \sum_{\mu,i=1}^{N_\mathrm{N},N_\mathrm{e}} \frac{\mathrm{Z}_\mu}{r_{\mu,i}} \right], \tag{3.2}$$

with Planck's constant $2\pi\hbar$ and Coulomb's force constant $1/4\pi\epsilon_0$. To improve the readability the abbreviations

$$\begin{aligned} \boldsymbol{\nabla}_\mu &= \frac{\partial}{\partial \mathbf{R}_\mu} = \sum_{j=x,y,z} \frac{\partial}{\partial R_{j,\mu}} \hat{\mathbf{e}}_j \quad \text{with Cartesian unit vectors } \hat{\mathbf{e}}_j\ ,\ j \in \{x, y, z\}\,, \\ \boldsymbol{\nabla}_i &= \frac{\partial}{\partial \mathbf{r}_i}\,, \quad r_{\mu,\nu} = |\mathbf{R}_\mu - \mathbf{R}_\nu|\,, \quad r_{i,j} = |\mathbf{r}_i - \mathbf{r}_j| \quad \text{and} \quad r_{\mu,i} = |\mathbf{R}_\mu - \mathbf{r}_i| \end{aligned} \tag{3.3}$$

are used. The first two terms in Eq. (3.2) denote the kinetic energy contribution of the nuclei and of the electrons, respectively. The latter three terms express the electrostatic interaction among the nuclei, among the electrons and finally among each pair of particles with opposite charges.

In the vast majority of problems in solid state physics, the task of solving Eq. (3.1) is simplified by the *Born-Oppenheimer approximation* [48]. Here the many-body wave-function is approximated by a product of wave functions

$$\Psi(\{\mathbf{R}_\mu\},\{\mathbf{r}_i\}) = \Psi_\mathrm{N}(\{\mathbf{R}_\mu\}) \cdot \Psi_\mathrm{e}^{(\{\mathbf{R}_\mu\})}(\{\mathbf{r}_i\})\,, \tag{3.4}$$

where $\{\mathbf{R}_\mu\}$ and $\{\mathbf{r}_i\}$ collect all nuclear and all electronic coordinates, respectively. Thus, the purely electronic eigenvalue problem

$$H_\mathrm{e}^{(\{\mathbf{R}_\mu\})}\Psi_\mathrm{e}^{(\{\mathbf{R}_\mu\})}(\{\mathbf{r}_i\}) = E_\mathrm{e}^{(\{\mathbf{R}_\mu\})}\Psi_\mathrm{e}^{(\{\mathbf{R}_\mu\})}(\{\mathbf{r}_i\}) \tag{3.5}$$

can be treated separately from the nuclei, which only enter Eq. (3.5) as a set of parameters $\{\mathbf{R}_\mu\}$. This is justified by the fact that the mass ratio $\mathrm{m_e}/\mathrm{M}_\mu$ is in the order of 10^{-4} or less, which means that the electrons adapt to a new set of atomic positions $\{\mathbf{R}'_\mu\}$ nearly instantaneous. From now on the index for the nuclear positions will be dropped.

The electronic Hamiltonian in Eq. (3.5) can be written in the form

$$H_\mathrm{e} = T_\mathrm{e} + V_\mathrm{e,e} + V_\mathrm{N,e}\,. \tag{3.6}$$

Using Hartree atomic units[1] these components read $T_\mathrm{e} = \sum_{i=1}^{N_\mathrm{e}} \boldsymbol{\nabla}_i^2/2$ for the kinetic energy of the electrons, $V_\mathrm{e,e} = \sum_{i>j}^{N_\mathrm{e}} 1/r_{i,j}$ for the Coulomb interaction among the electrons and $V_\mathrm{N,e} = -\sum_{\mu,i=1}^{N_\mathrm{N},N_\mathrm{e}} \mathrm{Z}_\mu/r_{\mu,i}$ for the interaction among electrons and nuclei, which is treated as static external potential caused by the charges of the nuclei at fixed positions.

Since Ψ_e describes a multi-fermionic system, it has to be anti-symmetric with respect to particle exchange, as required by *Pauli's principle*. In addition, it is a complex function existing in the $3N_\mathrm{e}$-dimensional *Fock space*. Thus, the remaining task of solving Eq. (3.5) is possible only numerically and for systems with few electrons. Fortunately it turns out that the wave function contains far more information then usually needed, to gain requested physical quantities of a complex many-body problem. In DFT, which was derived in the mid-60s of the last century by Hohenberg, Kohn and Sham [49, 50], the density

$$n(\mathbf{r}) = \sum_{j=1}^{N_\mathrm{e}} \int \cdots \int \Psi_\mathrm{e}^*(\{\mathbf{r}_i\})\delta(\mathbf{r}-\mathbf{r}_j)\Psi_\mathrm{e}(\{\mathbf{r}_i\})\mathrm{d}^3r_1 \cdots \mathrm{d}^3r_{N_\mathrm{e}} \tag{3.7}$$

is found to be sufficient to derive any ground state property from. This is most astonishing given the fact that $n(\mathbf{r})$ only depends on the three space coordinates. In the next Section 3.1 the basic statements of this theory will be given.

[1] In Hartree atomic units one defines $\mathrm{m}_e = e = \hbar = 1/4\pi\epsilon_0 = 1$. Therefore length is expressed in units of Bohr's radius $a_\mathrm{B} = 4\pi\epsilon_0\hbar^2/\mathrm{m}_e e^2$ and the electrostatic energy of two elementary charges at this distance, called 1 Hartree ($\mathrm{htr} \equiv e^2/4\pi\epsilon_0 a_\mathrm{B}$), is defined as energy unit. Throughout this thesis formulas and values are expressed in atomic units, elsewise this will be pointed out explicitly.

3.1 The Theorem of Hohenberg and Kohn

Consider a system consisting of N_e electrons with a non-degenerate ground-state density $n(\mathbf{r})$. Then the following two major theorems build the foundation of DFT:

T1 Any ground-state observable O for the given system can be expressed as a unique functional $O[n]$ of the ground-state density $n(\mathbf{r})$.

T2 The energy functional fulfills the inequation

$$E_\mathrm{e}[\tilde{n}] > E_\mathrm{e}[n] \quad \forall\, \tilde{n} \not\equiv n\ ,\ \text{that satisfy} \int \tilde{n}(\mathbf{r})\mathrm{d}^3r = N_\mathrm{e} \tag{3.8}$$

The first statement ensures that if only the ground-state density n is known, in principle the determination of any other ground-state property is possible. Thus, the knowledge of Ψ_e is not essential. In particular, if two external potentials $V_\mathrm{ext}(\mathbf{r})$ and $V'_\mathrm{ext}(\mathbf{r})$ are known to belong to the same ground-state density $n(\mathbf{r})$, they are identical apart from a constant. The energy functional $E_\mathrm{e}[n]$ (*cf.* Eq. (3.5)) can be written as

$$E_\mathrm{e}[n] = E_\mathrm{ext}[n] + F[n] = \int V_\mathrm{ext}(\mathbf{r})n(\mathbf{r})\mathrm{d}^3r + F[n]\,, \tag{3.9}$$

with the external potential $V_\mathrm{ext}(\mathbf{r}) = \sum_{\mu=1}^{N_\mathrm{N}} \mathrm{Z}_\mu/|\mathbf{r}-\mathbf{R}_\mu|$ caused by the nuclei[2] and the so-called *Hohenberg-Kohn functional* $F[n]$, which contains the kinetic energy contribution as well as the electron-electron Coulomb interaction. $F[n]$ is called *universal*, since it does not depend on the system itself. So far, a closed expression for $F[n]$ has not been derived, but using a smart division and performing reasonable approximations help to perform DFT calculations nonetheless.

3.2 The Kohn-Sham Equations

Historically, the *Thomas-Fermi model* [51] was the first attempt to describe an electronic many-body system based on the density. Not without reason it is often referred to as antecessor of modern DFT calculation schemes. It showed, however, that approximations to the kinetic energy made within this model lead to imprecise, if not incorrect results (see *e.g.* [52] and references therein), even when additional terms like the Weizsäcker correction [53] are taken into account.

In 1965 Kohn and Sham proposed a decomposition of the *universal functional* F (*cf.* Eq. (3.9) of the form

$$F[n] = T_\mathrm{s}[n] + E_\mathrm{H}[n] + E_\mathrm{xc}[n]\,, \tag{3.10}$$

[2] In general V_ext also includes additional external potentials caused by an external electric field $\mathbf{E}(\mathbf{r})$. In this thesis, however, they are not considered.

with the kinetic energy of non-interacting electrons

$$T_\mathrm{s}[n] = \sum_i \int \psi_i^\dagger(\mathbf{r}') \left[-\frac{1}{2}\nabla^2\right] \psi_i(\mathbf{r}')\mathrm{d}^3r' \tag{3.11}$$

leading to the same density n, the classical Hartree energy

$$E_\mathrm{H}[n] = \frac{1}{2}\int\int \frac{n(\mathbf{r})n(\mathbf{r}')}{|\mathbf{r}-\mathbf{r}'|}\mathrm{d}^3r\mathrm{d}^3r' \tag{3.12}$$

and the so-called exchange-correlation energy functional $E_\mathrm{xc}[n]$, in which the remaining energetic contributions are collected. In fact, for the latter term Eq. (3.10) can be seen as definition. The main advantage of this decomposition of F is that the functionals with large contributions to the total energy, *i.e.* $T_\mathrm{s}[n]$ and $E_\mathrm{H}[n]$, are known explicitly, whereas the small correction to the kinetic energy of non-interacting particles and other exchange-correlation effects are stored in the latter term $E_\mathrm{xc}[n]$.

The second theorem of Hohenberg and Kohn states that the energy functional of the ground-state density is stationary on the condition of particle conservation:

$$0 \stackrel{!}{=} \frac{\delta E_e[n]}{\delta n} = \frac{\delta}{\delta n}\left(E_\mathrm{ext}[n] + T_\mathrm{s}[n] + E_\mathrm{H}[n] + E_\mathrm{xc}[n]\right) \tag{3.13}$$
$$\forall\, n(\mathbf{r}) \text{ with } \int n(\mathbf{r})\mathrm{d}^3r = N_\mathrm{e}\,.$$

If the density is replaced by a sum of normalized single particle wave-functions $\{\psi_j(\mathbf{r})\}$, *i.e.*

$$n(\mathbf{r}) = \sum_{j=1}^{N_\mathrm{e}} |\psi_j(\mathbf{r})|^2\,, \quad \int |\psi_j(\mathbf{r})|^2\mathrm{d}^3r = 1 \quad \forall\, 1 \le j \le N_\mathrm{e}\,, \tag{3.14}$$

the variational principle used in Eq. (3.13) can also be formulated with respect to these wave functions $\{\psi_j(\mathbf{r})\}$ or their complex conjugates $\{\psi_j^*(\mathbf{r})\}$. Thus, the interacting system is described by a system consisting of N_e non-interacting particles, that still lead to the same density $n(\mathbf{r})$. In literature it is referred to as *Kohn-Sham system*. Accounting for the need of normalized wave functions by Lagrange parameters $\{\epsilon_j\}$, the variation of $E_e[\{\psi_j\}]$ with respect to ψ_i^* yields

$$0 \stackrel{!}{=} \frac{\delta}{\delta\psi_i^*}\left(E_\mathrm{e}[\{\psi_j\}] - \sum_j \epsilon_j\left(\int |\psi_j(\mathbf{r})|^2\mathrm{d}^3r - 1\right)\right)\,. \tag{3.15}$$

Solving these expressions for every index i, leads to the *Kohn-Sham equations*

$$\left(-\frac{1}{2}\boldsymbol{\nabla}^2 + V_\mathrm{eff}(\mathbf{r})\right)\psi_i(\mathbf{r}) = \epsilon_i\psi_i(\mathbf{r}) \quad \forall\, 1 \le i \le N_\mathrm{e}\,. \tag{3.16}$$

The Kohn-Sham equations have the form of one-particle Schrödinger equations of N_e non-interacting electrons in an effective potential

$$V_\mathrm{eff}(\mathbf{r}) = V_\mathrm{ext}(\mathbf{r}) + V_\mathrm{H}(\mathbf{r}) + V_\mathrm{xc}(\mathbf{r}) \tag{3.17}$$

with

$$V_{\mathrm{H}}(\mathbf{r}) = \int \frac{n(\mathbf{r}')}{|\mathbf{r}-\mathbf{r}'|}\mathrm{d}^3r' \quad \text{and} \quad V_{\mathrm{xc}}(\mathbf{r}) = \frac{\delta E_{\mathrm{xc}}[n(\mathbf{r})])}{\delta n(\mathbf{r})}\,. \tag{3.18}$$

Although Eq. (3.16) resembles a one-particle Schrödinger equation, the wave functions $\{\psi_i(\mathbf{r})\}$ and the Lagrange parameters $\{\epsilon_i\}$ do not have any physical meaning, but stand for each Kohn-Sham particle's *effective* contribution to the density or the energy. In Section 3.4 it is shown how these parameters enter the total energy.

3.2.1 The self-consistency cycle

Given the fact, that the effective potential $V_{\mathrm{eff}}(\mathbf{r})$ depends on the density and that this density, on the other hand, is build by the solutions of Eq. (3.16), the Kohn-Sham equations form a self-consistent problem. The concept of solving such a problem is briefly suggested in the following sketch:

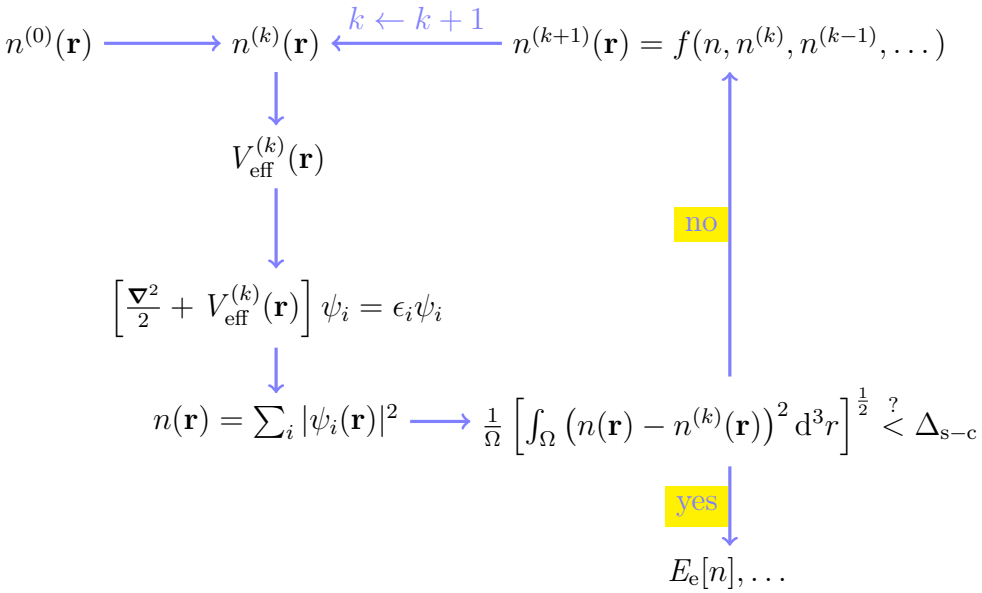

The starting density $n^{(0)}$ enters the cycle and within every iteration loop, the function f mixes the previous density $n^{(k)}$ with the recently calculated density n as it results from the Kohn-Sham functions $\{\psi_i\}$. In its simplest form the function f linearly mixes these two densities,

$$f(n, n^{(k)}) = \alpha n + (1-\alpha)n^{(k)}\,, \tag{3.19}$$

with the parameter α, normally in the range of a few percents. However, more complex mixing schemes, that for example include the mixing history, are known (see *e.g.* [54] and references therein). If now within one loop the densities do not vary much anymore, *i.e.* the integration norm of their absolute difference within the unit cell volume Ω is smaller than a certain value $\Delta_{\mathrm{s-c}}$, the Kohn-Sham equations can be regarded as nearly self-consistent, so that requested physical quantities can be derived as functionals of the most recent density n.

3.3 Concepts to approximate the Exchange-Correlation Energy

The decomposition of the *Hohenberg Kohn functional* $F[n]$ into three parts (*cf.* Eq. (3.10)) is mainly motivated by the ability to separate multi-particle effects, described by the exchange-correlation energy functional E_{xc}, from the single-electron contributions, namely the kinetic energy T_{s} of non-interacting particles and the Hartree energy E_{H}. Thus, the main contributions to the total energy are expressed explicitly. On the other hand the functional unawareness of F is only transferred to the lack of knowing E_{xc}. Ever since DFT has been investigated and improved, the search for reasonable approximations to E_{xc} has been *the* crucial task. Throughout decades a variety of approximations have been proposed and compared among each other (several references needed). Within this section two widely used schemes are presented, the *local density approximation* (LDA) and the *generalized gradient approximation* (GGA).

3.3.1 The Local Density Approximation

The *local density approximation* (LDA) in its originally form was proposed by Kohn and Sham in 1965 [50]. Historically, it is the first and at the same time most nearby concept to approximate the exchange-correlation functional $E_{\mathrm{xc}}[n]$. It is based upon the assumption that the electronic density is not varying rapidly. In fact LDA is exact for $n(\mathbf{r}) = const.$, *i.e.* a homogeneous electron gas. As the name already suggests, in LDA the unknown functional dependence of E_{xc} upon n is replaced by an integral over a function $\epsilon_{\mathrm{xc}}^{\mathrm{LDA}}$, that only depends upon the local values $n(\mathbf{r})$ of the density:

$$E_{\mathrm{xc}}[n] \approx E_{\mathrm{xc}}^{\mathrm{LDA}}[n] = \int n(\mathbf{r}')\epsilon_{\mathrm{xc}}^{\mathrm{LDA}}(n(\mathbf{r}'))\mathrm{d}^3r' \,. \tag{3.20}$$

The exchange-correlation energy density $\epsilon_{\mathrm{xc}}^{\mathrm{LDA}}$ can be decomposed into a sum of exchange part $\epsilon_{\mathrm{x}}^{\mathrm{LDA}}$ and correlation part $\epsilon_{\mathrm{c}}^{\mathrm{LDA}}$. Whereas the former contribution is obtainable for example from Hartree-Fock calculations for a homogeneous electron gas [55], the latter expression can be calculated using the Quantum Monte-Carlo method [56]. Despite the fact that the density of a solid is often far away from being constant, LDA was found to give reliable results on a variety of structural setups consisting of chemical elements throughout the periodic table [52]. However, LDA is also known for an overestimation of the binding energies (see *e.g.* [57]), whereas the prediction of the ground state energy of metal surfaces is too low compared to the experimental results [58]. Therefore, for certain systems it becomes necessary to use a different type of approximation to $E_{\mathrm{xc}}[n]$.

LDA can be extended to magnetic systems by $\epsilon_{\mathrm{xc}}^{\mathrm{LDA}}(n(\mathbf{r}), |\mathbf{m}(\mathbf{r})|)$ rather straightforward, where $\mathbf{m}$ denotes the magnetization of the system. The formulation of DFT for a magnetic system will be a topic of the next Chapter 4.

3.3.2 The Generalized Gradient Approximation

Aside from LDA, a more sophisticated technique has become popular in the last 20 years. The *generalized gradient approximation* (GGA) can be regarded as an extension of LDA. Additionally to the density n itself its gradient is taken into account as well. The approximation then reads

$$E_{\mathrm{xc}}[n] \approx E_{\mathrm{xc}}^{\mathrm{GGA}}[n] = \int n(\mathbf{r}')\epsilon_{\mathrm{xc}}^{\mathrm{GGA}}(n(\mathbf{r}'), \boldsymbol{\nabla} n(\mathbf{r}'))\mathrm{d}^3r' \,. \tag{3.21}$$

In contrast to the well-established form of $\epsilon_{\mathrm{xc}}^{\mathrm{LDA}}$, being the exchange-correlation energy density for a homogeneous electron gas, a reasonable form of the term $\epsilon_{\mathrm{xc}}^{\mathrm{GGA}}$ is more complicated. For example, for the description of an exchange-correlation hole that surrounds each electron, it is necessary to account for sum rules, that are fulfilled in LDA automatically. A widely used version of GGA, that fulfills several exact relations is the PBE, referring to the first letters of the authors' names [59]. In the same paper, they proposed a description of $\epsilon_{\mathrm{xc}}^{\mathrm{GGA}}$ using only a few adjusted parameters. The GGA-calculation within this thesis are performed using a scheme proposed by Perdew and Wang [60].

Build upon GGA even more sophisticated expressions for $E_{\mathrm{xc}}[n]$ are known, such as *meta*-GGA with the non-interaction kinetic energy as third input variable for ϵ_{xc} [61].

Besides LDA and GGA, a different class worth to mention is the approximation of the exchange-correlation potential with *hybrid functionals*. This technique is a mixed form of the Hartree-Fock formalism and a standard DFT contribution, such as LDA or GGA [62].

In this thesis most of the calculations were performed using the LDA as proposed by Moruzzi, Janak and Williams [63]. In Section 6.4.1 LDA- and GGA-calculations are compared.

3.4 The Total Energy

As pointed out in the previous Sections 3.1 and 3.2, the electronic energy E_{e} is a unique functional of the density and thus, can be expressed by *Kohn-Sham* wave-functions $\{\psi_i\}$:

$$E_{\mathrm{e}}[\{\psi_i\}] = T_{\mathrm{s}}[\{\psi_i\}] + E_{\mathrm{ext}}^{(\{\mathbf{R}_\mu\})}[\{\psi_i\}] + E_{\mathrm{H}}[\{\psi_i\}] + E_{\mathrm{xc}}[\{\psi_i\}] \,. \tag{3.22}$$

Using the Kohn-Sham equation (3.16) the expression for the kinetic energy functional can be rewritten as

$$\begin{aligned} T_{\mathrm{s}}[\{\psi_i\}] &= \sum_i \int \psi_i^\dagger(\mathbf{r}') \left[-\frac{1}{2}\nabla^2\right] \psi_i(\mathbf{r}')\mathrm{d}^3r' \\ &\underset{(3.16)}{=} \sum_i \int \psi_i^\dagger(\mathbf{r}')\epsilon_i\psi_i(\mathbf{r}')\mathrm{d}^3r' - \int V_{\mathrm{eff}}(\mathbf{r}')n(\mathbf{r}')\mathrm{d}^3r' \,. \end{aligned} \tag{3.23}$$

With the normalization condition for the wave functions $\{\psi_i\}$, defined in Eq. (3.14), the Hartree energy term (*cf.* Eq. (3.12)), which can be expressed as $E_{\mathrm{H}} = \frac{1}{2}\int V_{\mathrm{H}} n(\mathbf{r}')\mathrm{d}^3r'$,

and the expression $E_{\mathrm{xc}}[n] = \int \epsilon_{\mathrm{xc}}[n] n(\mathbf{r}') \mathrm{d}^3 r$ with the exchange-correlation energy density $\epsilon_{\mathrm{xc}}[n]$, the total electronic energy can be written as

$$E_{\mathrm{e}}[n] = \sum_i \epsilon_i + \underbrace{\int \left[-\frac{1}{2} V_{\mathrm{H}}(\mathbf{r}') - V_{\mathrm{xc}}(\mathbf{r}') + \epsilon_{\mathrm{xc}}[n(\mathbf{r}')] \right] n(\mathbf{r}') \mathrm{d}^3 r}_{= E_{\mathrm{dc}}[n]} , \tag{3.24}$$

where the expression E_{dc} is called *double counting term*, in analogy to $\frac{1}{2} \int V_{\mathrm{H}} n(\mathbf{r}) \mathrm{d}^3 r$, the term in the Hartree method.
Finally the interaction of the nuclei is taken into account and the equation for the total energy of the investigated problem reads

$$\begin{aligned} E = E(\{\mathbf{R}_\mu\}, \{\mathbf{r}_i\}) &= E_{\mathrm{N}}(\{\mathbf{R}_\mu\}) + E_{\mathrm{e}}[n] \\ &= \sum_{\mu<\nu}^{N_N} \frac{\mathrm{Z}_\mu \mathrm{Z}_\nu}{r_{\mu,\nu}} + \sum_i \epsilon_i + E_{\mathrm{dc}}[n] \end{aligned} \tag{3.25}$$

Varying the positions $\{\mathbf{R}_\mu\}$ of the nuclei and solving the corresponding electronic system yield a set of total energies, of which the ground-state energy of the full system can be calculated. This is useful, for example, to find the "best" value for the lattice constant a of a given structure or to obtain the relaxed structure of a surface. Note that within formula (3.25) still the nuclear kinetic energy is neglected, as it is common for calculations in the Born-Oppenheimer approximation.

3.4.1 Andersen's Force Theorem

As previously mentioned in Section 3.2.1 the Kohn-Sham equations (3.16) state a self-consistent problem, that only can be solved by performing a sufficient high number of iterations within the self-consistent cycle. This is necessary in order to approach the "correct" density up to a desired accuracy. However, if a self-consistent solution to a problem is already known, whose external potential V_{ext} slightly differs from the regarded one, it is not necessary to do so. In 1980, Mackintosh and Andersen proposed a scheme called *frozen force theorem* [64], that allows the calculation of the electronic energy without knowing the self-consistent solution. In order to gain the change ΔE of the total electronic energy, the force theorem makes use of the fact, that E_{dc} does not depend explicitly on V_{ext}, so that in first order ΔE is given by the change in the sum of the Kohn-Sham eigenvalues $\sum_i \epsilon_i$.

Consider an electronic problem that is described by Kohn-Sham equations of the form

$$H \psi_\nu = \epsilon_\nu \psi_\nu \quad \text{with} \quad H = H[\{\psi_\nu\}] , \tag{3.26}$$

where the index ν enumerates the number of orbitals that are occupied by the electrons. If now a self-consistent solution to a closely related problem

$$H^{(0)} \psi_\nu^{(0)} = \epsilon_\nu^{(0)} \psi_\nu^{(0)} \quad \text{with} \quad H^{(0)} = H^{(0)}[\{\psi_\nu^{(0)}\}] \tag{3.27}$$

is known, the Hamiltonian of Eq. (3.26) can be separated into two parts, $H = H^{(0)} + H^{\text{pert}}$. Instead of solving Eq. (3.26) self-consistently, the change within the total electronic energy is given by

$$\Delta E \approx E_e^{\text{FT}} - E_e^{(0)} = \sum_{\nu}^{\text{occ.}} \epsilon_\nu^{\text{FT}} - \sum_{\nu}^{\text{occ.}} \epsilon_\nu^{(0)} \tag{3.28}$$

with the eigenvalues ϵ_ν^{FT} satisfying the eigenvalue problem

$$H[\{\psi_\mu^{(0)}\}]\psi_\nu^{\text{FT}} = \epsilon_\nu^{\text{FT}}\psi_\nu^{\text{FT}}\,. \tag{3.29}$$

Note, that Eq. (3.29) is not a self-consistent problem. Thus, performing the force step only one iteration is needed. A derivation of the force theorem is presented *e.g.* in [65].

Since E_{ext} was not specified by Eqs. (3.26) or (3.27) the force theorem can be used for a number of different scenarios. However, when *e.g.* the volume of the unit cell is varied, the force theorem does not apply anymore, since E_{dc} depends explicitly on the density n.

Within this thesis, the force theorem is used when spin-orbit coupling is included into a calculationi that is pre-converged in the scalar-relativistic approximation or when a rotation of the spin moments is performed. When the Dzyaloshinskii-Moriya interaction is calculated, the perturbation of small varying propagation vectors describing slightly different spin spirals is calculated within this scheme as well. In fact, in the latter case a combination with perturbations regarding spin-orbit coupling is performed.

4 Vector-spin DFT

In the previous Chapter 3 the concept of DFT and the Kohn-Sham formalism were introduced as a powerful approach to the treatment of a complex many-body problem in solid state physics with respect to its ground state. It is now necessary to expand the theory to the wide class of magnetic systems and include the capability of dealing with relativistic effects.

4.1 The Formalism of Barth and Hedin

An electron interacts with an external magnetic field $\mathbf{B}_{\text{ext}}(\mathbf{r})$ via its electronic spin moment $\boldsymbol{\mu}$. Therefore, a structure that exhibits a non-vanishing magnetic density $\mathbf{m}(\mathbf{r})\not\equiv 0$ can only be described properly by a *spin polarized* DFT. In 1972, von Barth and Hedin were the first to propose such an extension of DFT [66]. They showed that the uniqueness of a ground state property is not provided anymore, if it is regarded as a functional of the density $n(\mathbf{r})$ only[1]. Thus, the scalar $n(\mathbf{r})$, is replaced by a hermitian (2×2) density matrix $\underline{n}(\mathbf{r})$ with spin-resolved components

$$n_{\alpha\beta}(\mathbf{r}) = \langle \Psi_{\text{e}}(\{\mathbf{r}_i\})|\phi_\beta(\mathbf{r})^\dagger \phi_\alpha(\mathbf{r})|\Psi_{\text{e}}(\{\mathbf{r}_i\})\rangle \quad , \quad \alpha,\beta \in \{\sigma_1,\sigma_2\}\,, \tag{4.1}$$

where $\Psi_{\text{e}}(\{\mathbf{r}_i\})$ is the electronic wave function (*cf.* Eq. (3.5)) and $\phi_\alpha(\mathbf{r})$ and $\phi_\beta(\mathbf{r})$ are the field operators for particles with spin quantum numbers α and β, respectively. In addition, within the spin-polarized Kohn-Sham formalism the scalar potentials $V_{\text{ext}}(\mathbf{r})$ and $V_{\text{xc}}(\mathbf{r})$ are replaced by (2×2) matrices $\underline{V}_{\text{ext}}(\mathbf{r})$ and $\underline{V}_{\text{xc}}(\mathbf{r})$, respectively. Their components read

$$V_{\text{ext},\alpha\beta}(\mathbf{r}) = V_{\text{ext},\alpha\beta}[n_{\alpha\beta}(\mathbf{r})] \quad \text{and} \quad V_{\text{xc},\alpha\beta}(\mathbf{r}) = \frac{\delta E_{\text{xc}}}{\delta n_{\alpha\beta}(\mathbf{r})}\,. \tag{4.2}$$

In analogy to the variational principle in Eq. (3.8), the ground-state density matrix $\underline{n}(\mathbf{r})$ minimizes the energy functional under the constraint of particle conservation, *i.e.*

$$E_{\text{e}}[\underline{\tilde{n}}] > E_{\text{e}}[\underline{n}] \quad \forall\ \underline{\tilde{n}} \not\equiv \underline{n}\ ,\ \text{that satisfy}\ \int \mathsf{tr}[\underline{\tilde{n}}(\mathbf{r})]\,\mathrm{d}^3 r = N_{\text{e}}\,, \tag{4.3}$$

where $\mathsf{tr}[\underline{\tilde{n}}] = \sum_\alpha \tilde{n}_{\alpha\alpha}$ represents the trace of the matrix $\underline{\tilde{n}}$. The Kohn-Sham equations for a spin system are formulated with respect to a two-component *Kohn-Sham spinor*

$$\boldsymbol{\psi}_i(\mathbf{r}) = \begin{pmatrix} \psi_{i\sigma_1}(\mathbf{r}) \\ \psi_{i\sigma_2}(\mathbf{r}) \end{pmatrix} \tag{4.4}$$

[1] In fact, explicit examples of potentials are known that differ in more than a constant shift, yet belong to the same ground state density [67].

and have the form

$$\left[\left(-\frac{1}{2}\boldsymbol{\nabla}^2+\int\frac{\mathsf{tr}[\underline{n}(\mathbf{r}')]}{|\mathbf{r}-\mathbf{r}'|}\mathrm{d}^3r'\right)\underline{\mathbb{1}}+\underline{V}_{\mathrm{ext}}(\mathbf{r})+\underline{V}_{\mathrm{xc}}(\mathbf{r})\right]\boldsymbol{\psi}_i(\mathbf{r})=\epsilon_i\boldsymbol{\psi}_i(\mathbf{r})\,, \tag{4.5}$$

where $\underline{\mathbb{1}}$ denotes the (2×2) unity matrix. The Kohn-Sham spinor's components can be used to express the components of the density matrix,

$$n_{\alpha\beta}(\mathbf{r})=\sum_{i=1}^{N_\mathrm{e}}\psi_{i\beta}(\mathbf{r})^*\psi_{i\alpha}(\mathbf{r})\,. \tag{4.6}$$

In an equivalent formulation, however, the density matrix can also be written as a sum of a scalar and a vectorial contribution,

$$\underline{n}(\mathbf{r})=\frac{1}{2}\left(n(\mathbf{r})\underline{\mathbb{1}}+\underline{\boldsymbol{\sigma}}\cdot\mathbf{s}(\mathbf{r})\right)=\frac{1}{2}\begin{pmatrix}n(\mathbf{r})+s_z(\mathbf{r}) & s_x(\mathbf{r})-\mathrm{i}s_y(\mathbf{r})\\ s_x(\mathbf{r})+\mathrm{i}s_y(\mathbf{r}) & n(\mathbf{r})-s_z(\mathbf{r})\end{pmatrix}\,, \tag{4.7}$$

where $n(\mathbf{r})$ is the spin-averaged density used throughout Chapter 3, and $\mathbf{s}(\mathbf{r})$ is the spin density , which is related to the magnetization density $\mathbf{m}(\mathbf{r})$ via $\mathbf{m}(\mathbf{r})=-\mu_\mathrm{B}\mathbf{s}(\mathbf{r})$, where μ_B is the *Bohr magneton*[2]. The expression $\underline{\boldsymbol{\sigma}}$ is the vector of *Pauli matrices*, *i.e.*

$$\underline{\boldsymbol{\sigma}}=\left(\underline{\sigma_x},\underline{\sigma_y},\underline{\sigma_z}\right)^\mathrm{T}=\left(\begin{pmatrix}0&1\\1&0\end{pmatrix},\begin{pmatrix}0&-\mathrm{i}\\\mathrm{i}&0\end{pmatrix},\begin{pmatrix}1&0\\0&-1\end{pmatrix}\right)^\mathrm{T}\,. \tag{4.8}$$

A comparison of the components in Eq. (4.6) to Eq. (4.7) leads to

$$n(\mathbf{r}) \;=\; \sum_i\boldsymbol{\psi}_i(\mathbf{r})^\dagger\boldsymbol{\psi}_i(\mathbf{r})=\sum_i\left[\psi_{i\sigma_1}(\mathbf{r})^*\psi_{i\sigma_1}(\mathbf{r})+\psi_{i\sigma_2}(\mathbf{r})^*\psi_{i\sigma_2}(\mathbf{r})\right] \tag{4.9}$$

and

$$\mathbf{s}(\mathbf{r}) \;=\; \sum_i\boldsymbol{\psi}_i(\mathbf{r})^\dagger\underline{\boldsymbol{\sigma}}\boldsymbol{\psi}_i(\mathbf{r})=\begin{pmatrix}\sum_i\left[\psi_{i\sigma_1}(\mathbf{r})^*\psi_{i\sigma_2}(\mathbf{r})+\psi_{i\sigma_2}(\mathbf{r})^*\psi_{i\sigma_1}(\mathbf{r})\right]\\ -\mathrm{i}\sum_i\left[\psi_{i\sigma_1}(\mathbf{r})^*\psi_{i\sigma_2}(\mathbf{r})-\psi_{i\sigma_2}(\mathbf{r})^*\psi_{i\sigma_1}(\mathbf{r})\right]\\ \sum_i\left[\psi_{i\sigma_1}(\mathbf{r})^*\psi_{i\sigma_1}(\mathbf{r})-\psi_{i\sigma_2}(\mathbf{r})^*\psi_{i\sigma_2}(\mathbf{r})\right]\end{pmatrix}\,. \tag{4.10}$$

In a similar way, the potential matrices are decomposable into the originally used scalar potentials and vectorial contributions,

$$\underline{V}_{\mathrm{ext}}(\mathbf{r})=V_{\mathrm{ext}}(\mathbf{r})\underline{\mathbb{1}}+\mu_\mathrm{B}\underline{\boldsymbol{\sigma}}\cdot\mathbf{B}_{\mathrm{ext}}(\mathbf{r})\quad\text{and}\quad\underline{V}_{\mathrm{xc}}(\mathbf{r})=V_{\mathrm{xc}}(\mathbf{r})\underline{\mathbb{1}}+\mu_\mathrm{B}\underline{\boldsymbol{\sigma}}\cdot\mathbf{B}_{\mathrm{xc}}(\mathbf{r})\,, \tag{4.11}$$

with the exchange-correlation magnetic field

$$\mathbf{B}_{\mathrm{xc}}(\mathbf{r})=\frac{\delta E_{\mathrm{xc}}[n(\mathbf{r}),\mathbf{m}(\mathbf{r})]}{\delta\mathbf{m}(\mathbf{r})}=\sum_{k=x,y,z}\frac{\delta E_{\mathrm{xc}}[n(\mathbf{r}),\mathbf{m}(\mathbf{r})]}{\delta m_k(\mathbf{r})}\hat{\mathbf{e}}_k\,. \tag{4.12}$$

[2]In Hartree atomic units, the Bohr magneton is either given by $\mu_\mathrm{B}=1/2$ *a.u.* (referring to SI units) or by $\mu_\mathrm{B}=1/2c$ *a.u.* (referring to Gaussian CGS units), where c is the speed of light.

Using Eqs. (4.7) and (4.11), the *spin polarized Kohn-Sham equations* (4.5) can be rewritten in the form

$$\left[\left(-\frac{1}{2}\boldsymbol{\nabla}^2 + V_{\text{eff}}(\mathbf{r})\right)\underline{\mathbb{1}} + \mu_{\text{B}}\underline{\boldsymbol{\sigma}}\cdot\mathbf{B}_{\text{eff}}(\mathbf{r})\right]\boldsymbol{\psi}_i(\mathbf{r}) = \epsilon_i\boldsymbol{\psi}_i(\mathbf{r})\,. \tag{4.13}$$

The effective single-particle potential $V_{\text{eff}}(\mathbf{r})$ was already defined in Eq. (3.17) and consists of the Hartree term $V_{\text{H}}(\mathbf{r})$ as well as the external potential $V_{\text{ext}}(\mathbf{r})$ and the exchange-correlation potential $V_{\text{xc}}(\mathbf{r})$. The effective magnetic field $\mathbf{B}_{\text{eff}}(\mathbf{r})$ is given by the sum of the exchange-correlation field $\mathbf{B}_{\text{xc}}(\mathbf{r})$ and an external magnetic field $\mathbf{B}_{\text{ext}}(\mathbf{r})$. However, in this thesis the latter term shall not be considered.

The Local Spin Density Approximation

Within the spin polarized DFT, the LDA (*cf.* Eq. 3.20) is extended to the *local spin density* (LSD) *approximation*:

$$E_{\text{xc}}[n,\boldsymbol{m}] \approx E_{\text{xc}}^{\text{LSD}}[n,\boldsymbol{m}] = \int n(\mathbf{r}')\epsilon_{\text{xc}}^{\text{LSD}}(n(\mathbf{r}'),|\boldsymbol{m}(\mathbf{r}')|)\mathrm{d}^3r'\,. \tag{4.14}$$

Due to the local nature of $\epsilon_{\text{xc}}^{\text{LSD}}$ the direction of the magnetic moment does not enter the energy density of Eq. (4.14).

4.2 DFT for non-collinear magnetic systems

In principle, the vector-spin DFT, as presented in the previous Section 4.1, is applicable to any magnetic ground-state system. For a spin structure exhibiting a collinear magnetic density, i.e the magnetization direction $\hat{\mathbf{m}}(\mathbf{r}) = \mathbf{m}(\mathbf{r})/m(\mathbf{r})$ is constant throughout the crystal, it is always possible to choose the spin coordinate frame such, that the *spin quantization axis* (SQA) points along the z-direction of the real-space[3]. Thus, the Hamiltonian H in Eq. (4.13) becomes diagonal and the problem can be solved independently for each component of $\boldsymbol{\psi}_i$, where σ_1 and σ_2 are now associated with spin-up ($\uparrow$) and spin-down ($\downarrow$) states, respectively.
In the more general case of non-collinearity, the Hamiltonian cannot be set to a diagonal form using one global (g) spin frame. Instead it is possible to define a matrix field with position dependent complex (2×2) matrices $\underline{\mathsf{U}}^{\mathsf{lg}}(\mathbf{r})$, that can be used to transfer the problem into a local (l) spin frame, in which the rotated Hamiltonian is diagonal, *i.e.*

$$\underbrace{\begin{pmatrix} H^{(\mathsf{l})}_{(\uparrow)(\uparrow)}(\mathbf{r}) & 0 \\ 0 & H^{(\mathsf{l})}_{(\downarrow)(\downarrow)}(\mathbf{r})\end{pmatrix}}_{\underline{H}^{(\mathsf{l})}(\mathbf{r})} = \underline{\mathsf{U}}^{\mathsf{lg}}(\mathbf{r})\underbrace{\begin{pmatrix} H^{(\mathsf{g})}_{\sigma_1\sigma_1}(\mathbf{r}) & H^{(\mathsf{g})}_{\sigma_1\sigma_2}(\mathbf{r}) \\ H^{(\mathsf{g})}_{\sigma_2\sigma_1}(\mathbf{r}) & H^{(\mathsf{g})}_{\sigma_2\sigma_2}(\mathbf{r})\end{pmatrix}}_{\underline{H}^{(\mathsf{g})}(\mathbf{r})}\underline{\mathsf{U}}^{\mathsf{lg}}(\mathbf{r})^{\dagger}\,. \tag{4.15}$$

[3]This is no longer possible if the ground-state energy is affected by a coupling of spin- and real-space. This coupling term and its origin will be discussed in more detail in Section 4.4.1.

In certain cases it is useful to perform such a rotation into the local frame, to make profit from the diagonal form of the Hamiltonian therein. This is especially the case for homogeneous spin spirals, where the rotation by a constant angle along a given direction allows to work with a wave function that fulfills the generalized Bloch theorem.

The task of solving the Kohn-Sham equations for non-collinear magnetic structures will be picked up again in Section 5.5, where some aspects of the implementation into the FLEUR code are discussed.

4.3 The Generalized Bloch Theorem

A non-collinear calculation within a chemical periodic structure can be a very demanding task. Compared to the collinear structure the system normally exhibits a loss of symmetry and thus, several *a priori* simplifications cannot be made. In particular, the restriction to a chemical unit cell does not hold anymore. For systems with a periodic magnetic structure that is commensurate to the crystal structure, the use of a supercell, consisting of a certain number of unit cells, can express the periodicity of the system. In the case of a homogeneous spin spiral (*cf.* Sec. 2.3.1), however, the so-called *generalized Bloch theorem* can be used to circumvent costly calculations within a supercell.
The classical *Bloch theorem* is applicable to the crystal structure of a solid if the potential $V(\mathbf{r})$ and thus, the Hamilton operator $H(\mathbf{r})$ exhibit translational invariance, $\mathsf{T}_{\mathbf{R}^n} H(\mathbf{r}) = H(\mathbf{r}+\mathbf{R}^{\boldsymbol{n}}) = H(\mathbf{r})$, with the translation operator $\mathsf{T}_{\mathbf{R}^n}$. The lattice vector is defined as $\mathbf{R}^{\boldsymbol{n}} = \boldsymbol{n}\cdot\boldsymbol{a} = \sum_{i=1}^{3} n_i \boldsymbol{a}_i$, where $n_1, n_2, n_3 \in \mathbb{Z}$ and the vector $\boldsymbol{a}$ contains the three basis vectors $\boldsymbol{a}_1, \boldsymbol{a}_2$ and $\boldsymbol{a}_3$ of the unit cell. The corresponding eigenfunctions are given by *Bloch functions*

$$\psi_{\mathbf{k}\nu}(\mathbf{r}) = \mathrm{e}^{\mathrm{i}\mathbf{k}\cdot\mathbf{r}} u_{\mathbf{k}\nu}(\mathbf{r}) \quad , \; u_{\mathbf{k}\nu}(\mathbf{r}+\mathbf{R}^{\boldsymbol{n}}) = u_{\mathbf{k}\nu}(\mathbf{r})\,, \tag{4.16}$$

which are products of an exponential and a lattice-periodic function $u_{\mathbf{k}\nu}$, that depends on the Bloch vector $\mathbf{k}$ and the energy band ν.
For a spin-polarized system with a magnetization direction that is rotating with a constant angle[4] $\varphi = \mathbf{q}\cdot\mathbf{r}$ along a spatial direction in the crystal, the Hamiltonian $\underline{H}^{(\alpha)(\beta)}$ remains invariant under a general translation $\underline{\mathsf{T}}^{\mathrm{gen}}_{\boldsymbol{n}} = \mathsf{T}_{\mathbf{R}^n}\underline{\mathsf{U}}_{\varphi_{\boldsymbol{n}}}$, where $\underline{\mathsf{U}}_{\varphi_{\boldsymbol{n}}} = \exp\left(\mathrm{i}\frac{\varphi_{\boldsymbol{n}}}{2}\cdot\underline{\sigma_z}\right)$ denotes a rotation in the spin-space by an angle of $\varphi_{\boldsymbol{n}} = \mathbf{q}\cdot\mathbf{R}^{\boldsymbol{n}}$ perpendicular to the z-axis:

$$\underline{\mathsf{T}}^{\mathrm{gen}}_{\boldsymbol{n}}\underline{H}^{(\alpha)(\beta)}(\mathbf{r}) = \mathsf{T}_{\mathbf{R}^n}\underline{\mathsf{U}}_{\varphi_{\boldsymbol{n}}}\underline{H}^{(\alpha)(\beta)}(\mathbf{r}) = \underline{H}^{(\tilde{\alpha})(\tilde{\beta})}(\mathbf{r}+\mathbf{R}^{\boldsymbol{n}}) = \underline{H}^{(\alpha)(\beta)}(\mathbf{r})\,. \tag{4.17}$$

The spin-polarized *generalized Bloch functions* read

$$\boldsymbol{\psi}_{\mathbf{k}\nu}(\mathbf{r}) = \begin{pmatrix}\psi_{\mathbf{k}\nu\sigma_1}(\mathbf{r})\\ \psi_{\mathbf{k}\nu\sigma_2}(\mathbf{r})\end{pmatrix} = \begin{pmatrix}\mathrm{e}^{\mathrm{i}\left(\mathbf{k}-\frac{\mathbf{q}}{2}\right)\cdot\mathbf{r}} u^{(\uparrow)}_{\mathbf{k}\nu}(\mathbf{r})\\ \mathrm{e}^{\mathrm{i}\left(\mathbf{k}+\frac{\mathbf{q}}{2}\right)\cdot\mathbf{r}} u^{(\downarrow)}_{\mathbf{k}\nu}(\mathbf{r})\end{pmatrix} \quad , \; u^{(\sigma)}_{\mathbf{k}\nu}(\mathbf{r}+\mathbf{R}^{\boldsymbol{n}}) = u^{(\sigma)}_{\mathbf{k}\nu}(\mathbf{r})\,, \tag{4.18}$$

with $\sigma \in \{\uparrow,\downarrow\}$. When the spin-space is coupled to the real-space, as it is the case for calculations that include spin-orbit coupling (*cf.* Sec. 4.4.1), the generalized Bloch

[4] The spin spiral vector $\mathbf{q}$ is already known from Chapter 2.

theorem does not hold anymore. Since this coupling effect is of relativistic origin and therefore rather small, in the calculations performed for this thesis it is treated in a perturbative scheme (*cf.* Sec. 5.5.1). Thus, the use of supercells is circumvented.

4.4 Relativistic Corrections within DFT

If the investigated system involves heavy atoms, in most cases it is necessary to take relativistic effects into account. Especially in the vicinity of the nuclei the electrons gain large kinetic energies, whose description in a non-relativistic DFT normally lead to imprecise results. In addition the relativistic form gives rise to a coupling term of spin and spatial space, which will be discussed in Section 4.4.1. Thus, it is possible to talk about a spin orientation with respect to the lattice, as it becomes necessary for the MAE and DMI (*cf.* Ch. 2). The expansion of the DFT to the relativistic case was first proposed by Rajagopal and Callaway [68, 69], who introduced the electronic spin into the non-relativistic equations. The first full relativistic description of xc-effects within DFT was derived by MacDonald and Vosko [70].

For relativistic calculations it is necessary to introduce a four-component spinor

$$\boldsymbol{\Psi}_i = \left(\boldsymbol{\phi}_i, \boldsymbol{\chi}_i\right)^{\mathrm{T}} = \left(\phi_{i(\uparrow)}, \phi_{i(\downarrow)}, \chi_{i(\uparrow)}, \chi_{i(\downarrow)}\right)^{\mathrm{T}} \tag{4.19}$$

that consists of two parts, a so-called large component $\boldsymbol{\phi}_i$ and a small component $\boldsymbol{\chi}_i$. Both components are again divided into spin-up ($\uparrow$) and a spin-down ($\downarrow$) components. Formally the extension to the relativistic case is quite similar to the non-relativistic scheme, presented in Chapter 3. Despite the fact that now the kinetic energy has to be calculated from the Dirac equation, the total energy can still be decomposed into a sum of single-particle kinetic energies, a Hartree term, an energetic contribution from the external potential and a correlation-exchange energy functional. The latter can be approximated in the same way as in Section 3.3.
Instead of using the relativistic four-current[5]

$$j^{\mu}(\mathbf{r}) = c\overline{\boldsymbol{\Psi}}(\mathbf{r})\gamma^{\mu}\boldsymbol{\Psi}(\mathbf{r}) \tag{4.20}$$

as a basic variable of which the ground-state properties are functionals of, it is easier to continue using charge and magnetization densities, now given by:

$$\begin{aligned} n(\mathbf{r}) &= \sum_i |\boldsymbol{\Psi}_i(\mathbf{r})|^2 = \sum_i \left[\boldsymbol{\varphi}_i(\mathbf{r})^{\dagger}\boldsymbol{\varphi}_i(\mathbf{r}) + \boldsymbol{\chi}_i(\mathbf{r})^{\dagger}\boldsymbol{\chi}_i(\mathbf{r})\right] \\ \mathbf{m}(\mathbf{r}) &= \sum_i \left[\boldsymbol{\varphi}_i(\mathbf{r})^{\dagger}\underline{\boldsymbol{\sigma}}\boldsymbol{\varphi}_i(\mathbf{r}) + \boldsymbol{\chi}_i(\mathbf{r})^{\dagger}\underline{\boldsymbol{\sigma}}\boldsymbol{\chi}_i(\mathbf{r})\right] . \end{aligned} \tag{4.21}$$

[5] With the 4-tuple $\gamma^{\mu} = (\gamma^0, \boldsymbol{\gamma}) = \left(\begin{pmatrix} \underline{\mathbb{1}} & 0 \\ 0 & -\underline{\mathbb{1}} \end{pmatrix}, \begin{pmatrix} 0 & \underline{\boldsymbol{\sigma}} \\ -\underline{\boldsymbol{\sigma}} & 0 \end{pmatrix}\right)$ and the *Dirac adjoint* $\overline{\boldsymbol{\Psi}}(\mathbf{r}) = \boldsymbol{\Psi}^{\dagger}(\mathbf{r})\gamma^0$.

The total energy now reads

$$E_e(n(\mathbf{r}),\mathbf{m}(\mathbf{r})) = \int\left(\sum_i \mathbf{\Psi}_i^* \begin{pmatrix} c^2\underline{\mathbb{1}} & c\underline{\boldsymbol{\sigma}}\cdot\hat{\mathbf{p}} \\ c\underline{\boldsymbol{\sigma}}\cdot\hat{\mathbf{p}} & -c^2\underline{\mathbb{1}}\end{pmatrix}\mathbf{\Psi}_i + \left[V_{\mathrm{H}}(\mathbf{r}) + V_{\mathrm{ext}}(\mathbf{r}) + \epsilon_{\mathrm{xc}}\left[n(\mathbf{r}),\mathbf{m}(\mathbf{r})\right]\right] n(\mathbf{r})\right)\mathrm{d}^3r\,, \tag{4.22}$$

with the electron's rest mass c^2 and the momentum operator $\hat{\mathbf{p}} = -\mathrm{i}\boldsymbol{\nabla}$. As previously, variations of this expression lead to a set of equations similar to those of the non-relativistic case, the so-called *Kohn-Sham Dirac equations*

$$\left(\begin{pmatrix} c^2\underline{\mathbb{1}} & c\underline{\boldsymbol{\sigma}}\cdot\hat{\mathbf{p}} \\ c\underline{\boldsymbol{\sigma}}\cdot\hat{\mathbf{p}} & -c^2\underline{\mathbb{1}}\end{pmatrix} + \left(V_{\mathrm{eff}}(\mathbf{r}) + \mu_{\mathrm{B}}\underline{\boldsymbol{\sigma}}\cdot\mathbf{B}_{\mathrm{xc}}(\mathbf{r})\right)\begin{pmatrix}\underline{\mathbb{1}} & 0\\ 0 & \underline{\mathbb{1}}\end{pmatrix}\right)\mathbf{\Psi}_i(\mathbf{r}) = \left(\epsilon_i + c^2\right)\mathbf{\Psi}_i(\mathbf{r})\,. \tag{4.23}$$

In analogy to the non-relativistic case, $V_{\mathrm{eff}} = V_{\mathrm{H}} + V_{\mathrm{ext}} + V_{\mathrm{xc}}$ denotes the effective potential. The definitions of V_{xc} and $\mathbf{B}_{\mathrm{xc}}$ remain the same as given by Eqs. (3.18) and (4.12).

4.4.1 Spin-Orbit Coupling

An expansion of Eq. (4.23) up to the order of $1/c^2$ leads to the Hamiltonian (see *e.g.* [71])

$$\underline{H}_{\mathrm{rel}}(\mathbf{r}) = \underbrace{H_{\mathrm{KS}}(\mathbf{r})\underline{\mathbb{1}} + \frac{1}{c^2}\left[\left(-\hat{\mathbf{p}}^4 + \frac{1}{2}\boldsymbol{\nabla}^2 V_{\mathrm{eff}}(\mathbf{r})\right)\underline{\mathbb{1}} + \frac{\mu_{\mathrm{B}}}{2}\boldsymbol{\nabla}^2\left(\underline{\boldsymbol{\sigma}}\cdot\mathbf{B}_{\mathrm{eff}}(\mathbf{r})\right)\right]}_{=\underline{H}_{\mathrm{SR}}(\mathbf{r})} + \underbrace{\frac{1}{c^2}\underline{\boldsymbol{\sigma}}\cdot\left(\left(\boldsymbol{\nabla}V_{\mathrm{eff}}(\mathbf{r})\right)\times\hat{\mathbf{p}}\right)}_{=\underline{H}_{\mathrm{SO}}(\mathbf{r})} + \frac{\mu_{\mathrm{B}}}{c^2}\underline{B}(\mathbf{r}) + \mathcal{O}\left(\frac{1}{c^4}\right)\,, \tag{4.24}$$

where $H_{\mathrm{KS}}(\mathbf{r})$ is the non-relativistic Kohn-Sham Hamiltonian and $\underline{H}_{\mathrm{SR}}(\mathbf{r})$ the *scalar-relativistic approximation* [72], which is rotation-invariant in spin-space. Since $\mu_{\mathrm{B}}\underline{B}(\mathbf{r})/c^2$ is a comparatively small correction, it will be neglected in the following. The third term of Eq. (4.24), $\underline{H}_{\mathrm{SO}}(\mathbf{r})$, denotes a contribution to the total energy that is due to spin-orbit interaction. The coupling of the spin-space to the real-space is an important fact that is crucial to the appearance of the Dzyaloshinskii-Moriya interaction, as pointed out in Chapter 2.

In the vicinity of the μth nucleus ($\mathbf{r} = \mathbf{R}_\mu + \mathbf{r}_\mu$, $r_\mu \ll 1$) the gradient of the potential becomes large, so that $V_{\mathrm{eff}}(\mathbf{r})$ can be approximated by $\overline{V}_{\mathrm{eff}}(r_\mu)$, its spherical symmetric average with respect to the atomic center $\mathbf{R}_\mu$. Thus, the gradient of the potential reads

$$\boldsymbol{\nabla}V_{\mathrm{eff}}(\mathbf{r}) \approx \frac{\partial\overline{V}_{\mathrm{eff}}(r_\mu)}{\partial r_\mu}\hat{\mathbf{e}}_{r_\mu} \quad \text{, where } \hat{\mathbf{e}}_{r_\mu} = \frac{\mathbf{r}_\mu}{r_\mu}\,, \tag{4.25}$$

so that for this region, the cross product within $H_{\mathrm{SO}}(\mathbf{r})$ can be rewritten

$$(\boldsymbol{\nabla} V_{\mathrm{eff}}(\mathbf{r})) \times \hat{\mathbf{p}} \approx \frac{1}{r_\mu} \frac{\partial \overline{V}_{\mathrm{eff}}(r_\mu)}{\partial r_\mu} \hat{\mathbf{L}}_\mu \quad \text{, with} \quad \hat{\mathbf{L}}_\mu = \mathbf{r}_\mu \times \hat{\mathbf{p}} \,. \tag{4.26}$$

By introducing the *spin-orbit coupling constant* $\xi_\mu(r_\mu) = \frac{1}{c^2} \frac{1}{r_\mu} \frac{\partial \overline{V}_{\mathrm{eff}}(r_\mu)}{\partial r_\mu}$, that is normally decaying fast with increasing distance, the Hamiltonian denoting the spin-orbit interaction can be approximated by

$$H_{\mathrm{SO}}(\mathbf{r}) = \xi_\mu(r_\mu) \underline{\boldsymbol{\sigma}} \cdot \hat{\mathbf{L}}_\mu \quad \text{, for small } r_\mu = |\mathbf{r} - \mathbf{R}_\mu| \tag{4.27}$$

5 The FLAPW Method

In chapter 3 it was shown, that within DFT and the Kohn-Sham formalism the difficult task of solving a complex many-body problem is reducible to a problem of non-interacting so-called *Kohn-Sham particles* that are placed in an effective potential V_{eff}, containing all many-body effects such as Coulombic interaction, exchange and correlation effects. To solve these resulting Kohn-Sham equations (*cf.* Eq. (3.16)) within a computational procedure it is a common method to formulate the problem with respect to a well-chosen basis function set $\{\varphi_n\}$. For numerical reasons only a finite number M of basis functions can be taken into account. Thus, the main challenge of finding a well-suited basis set is to find an appropriate balance between the computational manageability of the basis functions and the requested accuracy of the calculated physical quantities. Suppose the expansion of the Kohn-Sham functions $\{\psi_i\}$ reads $\psi_i \approx \sum_{n=1}^{M} c_n^{(i)} \varphi_n$ and the expansion coefficients $c_n^{(i)}$ are written in the vector $\mathbf{c}^{(i)}$, then the Kohn-Sham equations are now described by

$$\underline{H} \cdot \mathbf{c}^{(i)} = \epsilon_i \underline{S} \cdot \mathbf{c}^{(i)} \,. \tag{5.1}$$

The matrices $\underline{H}$ and $\underline{S}$ are expressed in the chosen basis set and their components have the form

$$H_{m,n} = \int \varphi_m^*(\mathbf{r}) H \varphi_n(\mathbf{r}) \mathrm{d}^3 r \quad , \quad S_{m,n} = \int \varphi_m^*(\mathbf{r}) \varphi_n(\mathbf{r}) \mathrm{d}^3 r \underset{orth.}{=} \delta_{m,n} \,. \tag{5.2}$$

The last equal sign does only hold if the basis set is orthonormal. If this was the case, the matrix problem (5.1) becomes diagonal and a set of standard eigenvalue problems. Elsewise, it is a so-called *generalized eigenvalue problem.*

It is advisable to choose basis functions that already exhibit the symmetry or certain characteristics of the investigated structure. For a crystal with a lattice-periodic potential $V(\mathbf{r} + \mathbf{R}) = V(\mathbf{r})$ the resulting wave functions $\{\psi_i\} = \{\psi_{\mathbf{k},\nu}\}$ are Bloch waves. Hence, ordinary *plane waves* (PWs)

$$\varphi_n(\mathbf{r}) = \varphi_{\mathbf{K}}^{\text{PW}}(\mathbf{r}) = \frac{1}{\sqrt{\Omega}} \mathrm{e}^{\mathrm{i}\mathbf{K}\cdot\mathbf{r}} \quad \text{with} \quad \mathbf{K} = \mathbf{k} + \mathbf{G} \,, \tag{5.3}$$

where $\mathbf{G}$ is a reciprocal lattice vector with $\mathbf{G} \cdot \mathbf{R} \in 2\pi \cdot \mathbb{Z}$, form a promising basis set, since they are orthogonal and already fulfill Bloch's theorem, which can be verified easily. However, in the vicinity of the μth nucleus positioned at $\mathbf{R}_\mu$, the potential $V_{\text{eff}}(\mathbf{r})$ is dominated by a term proportional to $1/r_\mu$, where $r_\mu = |\mathbf{r} - \mathbf{R}_\mu|$. This induces a rapidly varying charge density, so that ψ_i can only be described properly by a huge number of basis functions [73]. In order to gain accurate results nonetheless, a widely used scheme is to work with *pseudo-potentials*, which normally differ from the original potential only

in the vicinity of the nuclei. As pointed out in Section 4.4, however, especially in these regions the proper description of the Kohn-Sham functions is desired, since relativistic effects, such as SOC, are largest there and play a major role regarding the calculated magnetic properties within this thesis. And more importantly, experiences have shown that the description of localized orbitals, like $3d$- or $4f$-states, is not satisfying within the method of pseudo-potentials [74]. Hence, an *all-electron* method with a different basis set is used, in which nearby the nuclei the PWs are substituted (*augmented*) by a different type of functions, whereas the true potential, containing divergences at the nuclei, nearly remains unchanged. In this chapter a brief introduction to this method and some aspects of the implementation into the FLEUR code are presented.

5.1 The Augmented Plane Wave Method

Close to the μth nucleus the problem can reasonably assumed to be radial symmetric with respect to the core center $\mathbf{R}_\mu$. Therefore, for regions with small r_μ a product ansatz

$$\varphi_n(\mathbf{r}) = \varphi_L^\mu(\mathbf{r}_\mu) = \tilde{u}_\ell(r_\mu) \cdot Y_L(\hat{\mathbf{r}}_\mu) \quad \text{with} \quad \hat{\mathbf{r}}_\mu = \mathbf{r}_\mu / r_\mu \tag{5.4}$$

is a favorable choice for a basis set, compared to the PWs of Eq. (5.3). L abbreviates the quantum numbers ℓ and m, $Y_L(\vartheta, \varphi)$ is a spherical harmonic and $\tilde{u}_\ell(r_\mu) = \tilde{u}_\ell(r_\mu|\epsilon)$ is a solution to the radial equation

$$\left[-\frac{1}{2}\frac{\partial^2}{\partial r_\mu^2} + \frac{\ell(\ell+1)}{2r_\mu^2} + V(r_\mu) - \epsilon\right] r_\mu \tilde{u}_\ell(r_\mu) = 0\,. \tag{5.5}$$

Although a basis set of this form is qualified to describe the wave function in the vicinity of the core sites, it is not preferable in the regions in between the atoms.
In 1937 Slater [73] proposed a scheme, called the *augmented* PW (APW) method, in which a basis set is used that combines the advantages of PWs and the product ansatz in Eq. (5.4), depending on the region in the crystal. For the construction of the basis functions, the real-space is divided into non-overlapping spheres, defined by $r_\mu < R_\mu^{\mathrm{MT}}$ and the remaining *interstitial region* (IR), *cf.* picture 5.1 on the right side. In the latter area a basis function is given by a PW $\varphi_{\mathbf{K}}^{\mathrm{PW}}$, whereas in the spheres, the so-called *muffin tins* (MTs), it is expanded into a finite number of functions $\{\varphi_L^\mu\}$. This expansion is necessary to ensure a correct *matching*, *i.e.* that a basis function is approximately continuous at the muffin-tin boundaries. Thus, the basis functions have the form

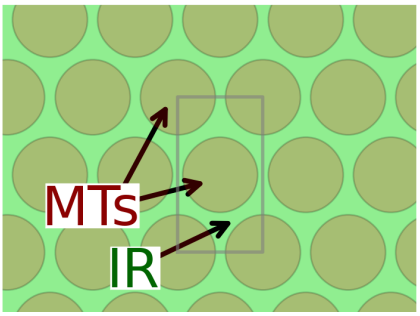

Fig. 5.1: The division of real-space into *muffin tins* (MTs) and remaining *interstitial region* (IR). The unit cell is illustrated by a gray rectangle.

$$\varphi_n(\mathbf{r}) = \varphi_{\mathbf{K}}^{\mathrm{APW}}(\mathbf{r}) = \begin{cases} \sum_L a_{\mathbf{K},L}^{(\mu)} \tilde{u}_\ell(r_\mu) Y_L(\hat{\mathbf{r}}_\mu) & , \ \mathbf{r} \in \mathrm{MT}\ \mu \\ \frac{1}{\sqrt{\Omega}} \mathrm{e}^{\mathrm{i}\mathbf{K}\cdot\mathbf{r}} & , \ \mathbf{r} \in \mathrm{IR} \end{cases}, \tag{5.6}$$

where the expansion coefficients $a^{(\mu)}_{\mathbf{K},L}$ are determined by the equations

$$\sum_L a^{(\mu)}_{\mathbf{K},L}\tilde{u}_\ell(R^{\mathrm{MT}}_\mu)Y_L(\hat{\mathbf{r}}_\mu) = \frac{1}{\sqrt{\Omega}}\mathrm{e}^{\mathrm{i}\mathbf{K}\cdot\left(\mathbf{R}_\mu + R^{\mathrm{MT}}_\mu\cdot\hat{\mathbf{r}}_\mu\right)}\,. \tag{5.7}$$

The corresponding approximation of the potential, called *shape-approximation*, is given by the expression

$$V_{\mathrm{eff}}(\mathbf{r}) \approx V^{\mathrm{ShA}}(\mathbf{r}) = \begin{cases} V^{(\mu)}(r_\mu) & ,\ \mathbf{r}\in \mathrm{MT}\ \mu \\ V_{\mathbf{0}} = \mathrm{const.} & ,\ \mathbf{r}\in \mathrm{IR} \end{cases} \tag{5.8}$$

and is indicated for the two-dimensional case in figure[1] 5.2. Although the APW method is a more sophisticated concept compared to a basis set of PWs, a major problem arises from the fact that $\tilde{u}_\ell$ and thus, the set of basis functions is depending on an energy value ϵ. It turns out that in order to properly describe an eigenstate $\psi_{\mathbf{k}\nu}$ for a given $\mathbf{k}$-point and the νth energy band, this parameter ϵ has to equal the corresponding band energy $\epsilon_{\mathbf{k}\nu}$. Thus, the set of basis functions differs for every eigenproblem and has to be determined separately within a nonlinear scheme. To circumvent such a time-demanding procedure, a *linearized* form of the APW basis set can be used instead, which is described in the next section.

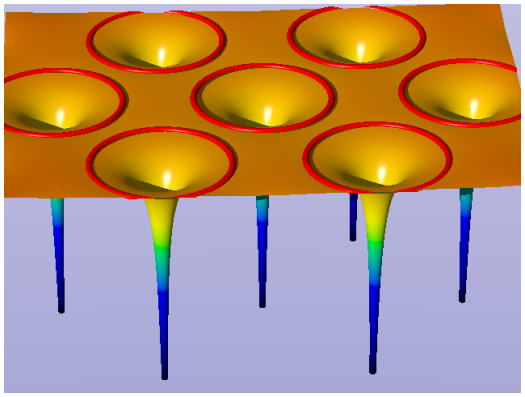

Fig. 5.2: The potential approximation within the APW method.

5.2 Extension to the FLAPW Method

In order to improve the basis set, the *linearized* APW (LAPW) method has been proposed [75] Here, the energy-dependent radial function $\tilde{u}_\ell$ is expanded up to the linear term within a Taylor series around a fixed energy parameter ϵ_ℓ:

$$\tilde{u}_\ell(r_\mu|\epsilon) = \underbrace{\tilde{u}_\ell(r_\mu|\epsilon_\ell)}_{=u_\ell(r_\mu)} + \underbrace{\frac{d\tilde{u}_\ell(r_\mu|\epsilon)}{d\epsilon}|_{\epsilon=\epsilon_\ell}}_{=\dot{u}_\ell(r_\mu)}(\epsilon-\epsilon_\ell) + \mathcal{O}\left((\epsilon-\epsilon_\ell)^2\right) \tag{5.9}$$

Thus, the problem of solving Eq. (5.5) can be expanded up to the linear term

$$\left[H^{(\mu)}_\ell - \underbrace{(\epsilon_\ell+\Delta\epsilon)}_{=\epsilon}\right] r_\mu \underbrace{\left[u_\ell(r_\mu|\epsilon_\ell) + \dot{u}_\ell(r_\mu|\epsilon_\ell)\Delta\epsilon + \mathcal{O}\left((\Delta\epsilon)^2\right)\right]}_{=\tilde{u}_\ell(r_\mu|\epsilon)} = 0\,, \tag{5.10}$$

[1] This picture was created in collaboration with Martin Schlipf.

with the Hamiltonian $H_\ell^{(\mu)} = -\Delta_{r_\mu}/2 + \ell(\ell+1)/2r_\mu^2 + V(r_\mu)$. Since $u_\ell(r_\mu)$ solves the equation (5.5) with the energy value ϵ_ℓ, the energy derivative $\dot{u}_\ell(r_\mu)$ satisfies the equation

$$\left[H_\ell^{(\mu)} - \epsilon_\ell\right] r_\mu \dot{u}_\ell(r_\mu|\epsilon_\ell) - r_\mu u_\ell(r_\mu|\epsilon_\ell) + \mathcal{O}\left((\Delta\epsilon)^2\right) = 0\,. \tag{5.11}$$

Both functions, u_ℓ and $\dot{u}_\ell$, are incorporated in the basis functions used within the LAPW method. Thus, these functions gain more variational freedom and their construction is done without the need for the knowledge of the accurate band energy values. The basis functions have the form

$$\varphi_n(\mathbf{r}) = \varphi_{\mathbf{K}}^{\mathrm{LAPW}}(\mathbf{r}) = \begin{cases} \sum_L \left(A_{\mathbf{K},L}^{(\mu)} u_\ell(r_\mu) + B_{\mathbf{K},L}^{(\mu)} \dot{u}_\ell(r_\mu)\right) Y_L(\hat{\mathbf{r}}_\mu) & ,\ \mathbf{r} \in \mathrm{MT}\ \mu \\ \frac{1}{\sqrt{\Omega}} \mathrm{e}^{\mathrm{i}\mathbf{K}\cdot\mathbf{r}} & ,\ \mathbf{r} \in \mathrm{IR} \end{cases}. \tag{5.12}$$

The expansion coefficients $A_{\mathbf{K},L}^{(\mu)}$ and $B_{\mathbf{K},L}^{(\mu)}$ are chosen such, that the basis function and its derivative are continuous at the boundaries between the MTs and the IR.

Because of

$$\int_{\mathrm{MT}\ \mu} \dot{u}^*(r_\mu|\epsilon) u(r_\mu|\epsilon) r^2 \mathrm{d}^3 r_\mu = \frac{1}{2}\frac{\mathrm{d}}{\mathrm{d}\epsilon} \underbrace{\int u^*(r_\mu|\epsilon) u(r_\mu|\epsilon) r^2 \mathrm{d}^3 r_\mu}_{=1} = 0\,, \tag{5.13}$$

the functions u_ℓ and $\dot{u}_\ell$ are orthogonal. Unfortunately, this does not hold for the LAPW basis set. Thus, in the problem given by Eq. (5.1) off-diagonal matrix elements have to be evaluated. However, this fact is tolerable, since the construction of the basis set is nicely adapted to the structure: Already a relative small number of basis functions is sufficient to give a proper description of the solid.

In contrast to the APW method, the basis function $\varphi_{\mathbf{K}}^{\mathrm{LAPW}}$, defined by Eq. (5.12), offers additional variational freedom, due to its linearized form with respect to u_ℓ. Especially in low-dimensional systems and open structures, such as surfaces or interlayers, chains or clusters, the appropriate description of the system can only be guaranteed if the potential is assumed to be non-spherical, so that the shape approximation in Eq. (5.8) must be dropped. Therefore, in the *full-potential* LAPW (FLAPW) method [76] the potential is expanded in the form

$$V_{\mathrm{eff}}(\mathbf{r}) \approx V^{\mathrm{FLAPW}}(\mathbf{r}) = \begin{cases} \sum_L^{L_{\max}^{\mathrm{n-sph}}} V_L^{(\mu)}(r_\mu) Y_L(\hat{\mathbf{r}}_\mu) & ,\ \mathbf{r} \in \mathrm{MT}\ \mu \\ \sum_{\mathbf{G}}^{\mathbf{G}_{\max}} \left[V_{\mathbf{G}}^{\mathrm{ext}}(\mathbf{r}) + V_{\mathbf{G}}^{\mathrm{H}}(\mathbf{r})\right] \mathrm{e}^{\mathrm{i}\mathbf{G}\cdot\mathbf{r}} & \\ \quad + \sum_{\mathbf{G}}^{\mathbf{G}_{\max}^{\mathrm{xc}}} V_{\mathbf{G}}^{\mathrm{xc}}(\mathbf{r}) \mathrm{e}^{\mathrm{i}\mathbf{G}\cdot\mathbf{r}} & ,\ \mathbf{r} \in \mathrm{IR} \end{cases}. \tag{5.14}$$

The expansion in the MTs in spherical harmonics up to a value $L_{\max}^{\mathrm{n-sph}}$ ($\ell_{\max}^{\mathrm{n-sph}}$ and corresponding quantum numbers m) is done by introducing a logarithmic radial mesh. In the IR $G_{\max}$ denotes the maximal wave vector that is taken into account. Additionally the exchange potential V_{xc} is expanded in basis functions up to a cut-off value $G_{\max}^{\mathrm{xc}}$.

The results presented within this thesis are calculated within the FLAPW method, as it is implemented into the FLEUR code. Within each iteration step of the self-consistent cycle (*cf.* Sec. 3.2.1), the basis set has to be regenerated, since the basis functions depend on the (renewed) potential V_{eff} per construction.

5.3 The Fermi Energy and Temperature Broadening

For a metallic system, the energy value of the highest occupied band of a system's ground state at zero temperature, $\mathrm{T} = 0$, is defined as *Fermi energy*, E_F. Thus, the charge density is given by

$$n(\mathbf{r}) = \frac{1}{\mathrm{V_{BZ}}} \int_\mathrm{BZ} \sum_\nu \Theta(E_\mathrm{F} - \epsilon_{\mathbf{k}\nu}) \boldsymbol{\psi}^\dagger_{\mathbf{k}\nu}(\mathbf{r}) \boldsymbol{\psi}_{\mathbf{k}\nu}(\mathbf{r}) \mathrm{d}^3k \,, \tag{5.15}$$

where $\mathrm{V_{BZ}}$ is the volume of the first *Brillouin zone* (BZ) in $\mathbf{k}$-space and $\Theta(E_\mathrm{F} - \epsilon_{\mathbf{k}\nu})$ is the *Heaviside step function*, which ensures that only occupied states contribute to the density. The requirement, that the integration of the density over the unit cell volume Ω equals N_e, the number of electrons therein, *i.e.*

$$\int_\Omega n(\mathbf{r}') \mathrm{d}^3r' \stackrel{!}{=} N_\mathrm{e} \,, \tag{5.16}$$

can be used to determine E_F. In the calculation scheme used in the FLEUR code, this quantity is recalculated within each iteration step (*cf.* Sec. 3.2.1). However, the sharp distinction between occupied and unoccupied states via the step function can slow down or even disrupt the convergence of the density. This is because of the states nearby E_F that may change their status from being occupied to empty or *vice versa* within one iteration step, which leads to sudden changes of the density. In order to avoid such convergence problems, the step function $\Theta(E_\mathrm{F} - \epsilon_{\mathbf{k}\nu})$ typically is replaced by a *Fermi-Dirac distribution*,

$$w_{\mathbf{k}\nu}(\epsilon_{\mathbf{k}\nu}, \mathrm{T}) = \left(\mathrm{e}^{\frac{1}{k_\mathrm{B}\mathrm{T}}(\epsilon_{\mathbf{k}\nu} - E_\mathrm{F})} + 1 \right)^{-1} \,, \tag{5.17}$$

with the temperature $\mathrm{T} > 0$ and the *Boltzmann constant* k_B. Thus, the impact of an energy state that crosses E_F during the self-consistency cycle on the density is scaled down depending on the chosen temperature. Note that $w_{\mathbf{k}\nu}(\epsilon_{\mathbf{k}\nu}, \mathrm{T}) \xrightarrow{\mathrm{T}\searrow 0} \Theta(E_\mathrm{F} - \epsilon_{\mathbf{k}\nu})$.

In the FLEUR code, the integral over the first BZ in Eq. (5.15) is replaced by a sum over a set of discrete $\mathbf{k}$-points. The accuracy of a calculation increases with the denseness of such a $\mathbf{k}$-point mesh, but so does the computational effort. Therefore it is highly advisable to use the structure's symmetry to reduce the BZ to the irreducible wedge of the BZ (IBZ) and use only the $\mathbf{k}$-points within this area. With a weight function $w(\mathbf{k})$, that fulfills $\sum_{\mathbf{k}\in\mathrm{IBZ}} w(\mathbf{k}) = 1$ and accounts for the number of $\mathbf{k}$-points connected to the regarded one via a symmetry transformation, the expression

$$\sum_{\mathbf{k}\in\mathrm{IBZ}} w(\mathbf{k}) \sum_\nu w_{\mathbf{k}\nu}(\epsilon_{\mathbf{k}\nu}, \mathbf{T}) \boldsymbol{\psi}^\dagger_{\mathbf{k}\nu}(\mathbf{r}) f_{\mathbf{k}\nu}(\mathbf{r}) \boldsymbol{\psi}_{\mathbf{k}\nu}(\mathbf{r}) \tag{5.18}$$

can be used to calculate the charge density ($f_{\mathbf{k}\nu}(\mathbf{r}) \equiv 1$), the magnetization density ($f_{\mathbf{k}\nu}(\mathbf{r}) \equiv \underline{\boldsymbol{\sigma}}$) and the sum of eigenvalues ($f_{\mathbf{k}\nu}(\mathbf{r}) \equiv \epsilon_{\mathbf{k}\nu}$).

5.4 Film Calculations within the FLAPW Method

The basis functions $\{\varphi_{\mathbf{K}}^{\mathrm{LAPW}}(\mathbf{r})\}$ (*cf.* Eq. (5.12)) are constructed such, that they fulfill Bloch's theorem for a three-dimensional bulk crystal. To investigate structures that are periodically repeated only in two dimensions, but non-periodic along the third direction, commonly chosen as z-axis, it is convenient to introduce a modified set of basis functions, that fulfill Bloch's theorem only in two dimensions[2]:

$$\psi_{\mathbf{k}_\parallel \nu}(\mathbf{r}) = \mathrm{e}^{\mathrm{i}\mathbf{k}_\parallel \cdot \mathbf{r}} u_{\mathbf{k}_\parallel \nu}(\mathbf{r}) \quad \text{, with } u_{\mathbf{k}_\parallel \nu}(\mathbf{r} + \mathbf{R}_\parallel^{\boldsymbol{n}}) = u_{\mathbf{k}_\parallel \nu}(\mathbf{r})\,. \tag{5.19}$$

The lattice vector $\mathbf{R}_\parallel^{\boldsymbol{n}}$ is parallel to the surface and the unit cell is stretched to $\pm\infty$ along the z-axis. In the reciprocal space the two-dimensional BZ is sampled by $\mathbf{k}_\parallel = (k_x, k_y)^{\mathrm{T}}$.

A semi-infinite structure, as it occurs when *e.g.* a solid's surface is investigated, can be approximated by a thin film, where the half space that contains the atoms is simulated by typically the first five to 20 atomic layers nearby the surface [77]. Hence, for calculations of a film structure with thickness D centered at $z = 0$, two vacuum regions (VRs) above and underneath the slab (labeled $\eta = 1$ and $\eta = 2$, respectively) are introduced. They are separated from the IR by the condition $|z| > D/2$ and fill out the remaining space.

The basis set that is used in the FLAPW method for two-dimensional structures is given by functions

$$\varphi_n(\mathbf{r}) = \varphi_{\mathbf{K}_\parallel, \mathbf{G}_\perp}^{\mathrm{LAPW,2D}}(\mathbf{r}) = \begin{cases} \sum_L \left(A_{\mathbf{K}_\parallel, L}^{(\mu)} u_\ell(r_\mu) + B_{\mathbf{K}_\parallel, L}^{(\mu)} \dot{u}_\ell(r_\mu) \right) Y_L(\hat{\mathbf{r}}_\mu) & , \mathbf{r} \in \mathrm{MT}\ \mu \\ \frac{1}{\sqrt{\Omega_{\mathrm{red}}}} \mathrm{e}^{\mathrm{i}(\mathbf{K}_\parallel + \mathbf{G}_\perp)\cdot \mathbf{r}} & , \mathbf{r} \in \mathrm{IR} \\ \mathrm{e}^{\mathrm{i}\mathbf{K}_\parallel \cdot \mathbf{r}} \left(A_{\mathrm{vac}, \mathbf{K}_\parallel}^{(\eta)} v_{\mathbf{K}_\parallel}(z) + B_{\mathrm{vac}, \mathbf{K}_\parallel}^{(\eta)} \dot{v}_{\mathbf{K}_\parallel}(z) \right) & , \mathbf{r} \in \mathrm{VR}\ \eta \end{cases} , \tag{5.20}$$

where Ω_{red} is the reduced unit-cell volume restricted to the IR only. While the MTs are treated equally to the bulk LAPW basis set as defined in Eq. (5.12), the plane wave in the IR distinguishes the directions parallel and perpendicular to the surface. The sum of reciprocal lattice vector $\mathbf{G}_\parallel$ and wave vector $\mathbf{k}_\parallel$, both parallel to the surface, is represented by $\mathbf{K}_\parallel$ and for the z-direction

$$\mathbf{G}_\perp = \frac{2\pi n}{\tilde{D}} \hat{\mathbf{e}}_z \quad , \quad n \in \mathbb{N} \text{ and } \tilde{D} > D \tag{5.21}$$

is defined. By using a new, larger, parameter $\tilde{D}$ rather than D, within the IR a restriction of the wave function ($\mathrm{e}^{\mathrm{i}G_\perp \cdot z} \xrightarrow{|z| \nearrow D/2} (-1)^n \ \forall n$ and $\tilde{D} = D$) at the boundaries to the VRs is avoided.

Finally, in the VRs the basis function is given by a product of a plane wave and a linear combination of two functions, $v_{\mathbf{K}_\parallel}(z)$ and its energy derivative $\dot{v}_{\mathbf{K}_\parallel}(z)$. They are

[2] In principle, it is also possible to create a superstructure, that preserves the three-dimensional periodicity by repeating the 2D-periodic structure along the third dimension at equidistant steps. However, in order to minimize artificially created interactions among the repeated images and their impact on the results the supercells have to be sufficiently large, so that a huge number of basis functions becomes necessary.

solutions to the equations

$$\left[\frac{1}{2}\mathbf{K}_{\parallel}^2 - \frac{1}{2}\frac{\partial^2}{\partial z^2} + V_{\text{vac}}(z) - E_{\text{vac}}\right] v_{\mathbf{K}_{\parallel}}(z) = 0 \tag{5.22}$$

$$\left[\frac{1}{2}\mathbf{K}_{\parallel}^2 - \frac{1}{2}\frac{\partial^2}{\partial z^2} + V_{\text{vac}}(z) - E_{\text{vac}}\right] \dot{v}_{\mathbf{K}_{\parallel}}(z) = v_{\mathbf{K}_{\parallel}}(z)\,, \tag{5.23}$$

with an energy parameter E_{vac} and a vacuum potential $V_{\text{vac}}(z)$, which is constructed from the average of $V_{\text{eff}}(\mathbf{r})$ over the x- and y-direction and sampled along the z-direction in equidistant intervals up to a desired distance from the surface. In analogy to the MTs the coefficients $A^{(\eta)}_{\text{vac},\mathbf{K}_{\parallel}}$ and $B^{(\eta)}_{\text{vac},\mathbf{K}_{\parallel}}$ in Eq. (5.20) are chosen such, that the resulting basis function and its derivative are continuous at the boundaries to the IR.

5.5 The FLAPW Method within Magnetic Systems

As pointed out in Chapter 4, for the capability of dealing with magnetic systems it is necessary to replace the one-component Kohn-Sham wave-function ψ_i by a spinor $\boldsymbol{\psi}_i = (\psi_{i\sigma_1}, \psi_{i\sigma_2})^{\mathrm{T}}$ with two components, one for each spin-channel[3]. This spinor is the solution to the Kohn-Sham equation for a magnetic system (*cf.* Eq. (4.13)),

$$\left[\left(-\frac{1}{2}\boldsymbol{\nabla}^2 + V_{\text{eff}}(\mathbf{r})\right)\underline{\mathbb{1}} + \mu_{\text{B}}\underline{\boldsymbol{\sigma}}\cdot\mathbf{B}_{\text{eff}}(\mathbf{r})\right]\begin{pmatrix}\psi_{i\sigma_1}(\mathbf{r})\\ \psi_{i\sigma_2}(\mathbf{r})\end{pmatrix} = \epsilon_i\begin{pmatrix}\psi_{i\sigma_1}(\mathbf{r})\\ \psi_{i\sigma_2}(\mathbf{r})\end{pmatrix}. \tag{5.24}$$

Each component $\psi_{i\sigma}(\mathbf{r})$ is expanded in terms of a spin-dependent basis set $\{\varphi^{\text{LAPW,2D}}_{\mathbf{K}_{\parallel}\mathbf{G}_{\perp},\sigma}(\mathbf{r})\}$, which is slightly modified compared to Eq. (5.20): The functions $u_{\ell,\sigma}$ and $v_{\ell,\sigma}$ as well as their derivatives are now derived from equations with spin-dependent potentials (e.g. $E_{\text{vac},\sigma}$) and energies $\epsilon_{\ell,\sigma}$ and $E_{\text{vac},\sigma}$, which is indicated by an additional index σ. Also, this index is added to the expansion A- and B-coefficients. In the IR the basis functions are identical for both spin-channels.

In the following, two cases are distinguished:

Collinear spin-configuration

If the spin moments are arranged parallel (or anti-parallel) along a fixed global direction, the magnetic density is given by

$$\mathbf{m}(\mathbf{r}) = m(\mathbf{r})\cdot\hat{\mathbf{e}}_z^{(\mathsf{g})}\ ,\ \hat{\mathbf{e}}_z^{(\mathsf{g})} = \underline{\mathsf{R}}^{(\mathsf{gr})}\hat{\mathbf{e}}_z\,, \tag{5.25}$$

with a (3×3) rotation matrix $\underline{\mathsf{R}}^{(\mathsf{gr})}$, connecting the real-space coordinate system to the global spin-frame (g), which – in this case – is the spin quantization axis (SQA, see Fig. 5.3).

[3]The extension to the relativistic spinor with its four components will not be described in this thesis. More information concerning this issue can be found in [78] and [79]

With the corresponding complex (2×2) rotation matrix in spin-space $\underline{\mathsf{U}}^{(\mathrm{gr})}$ the Hamiltonian in Eq. (5.24) can be transformed into a diagonal form:

$$\begin{aligned}\underline{H}(\mathbf{r}) &= \underline{\mathsf{U}}^{(\mathrm{gr})\,\dagger}\left[\left(-\frac{1}{2}\boldsymbol{\nabla}^2+V_{\mathrm{eff}}(\mathbf{r})\right)\underline{\mathbb{1}}+\mu_{\mathrm{B}}\underline{\sigma_z^{(\mathrm{g})}}\cdot B_{\mathrm{eff}}(\mathbf{r})\right]\underline{\mathsf{U}}^{(\mathrm{gr})}\\ &= \underline{\mathsf{U}}^{(\mathrm{gr})\,\dagger}\begin{pmatrix}-\frac{1}{2}\boldsymbol{\nabla}^2+V_{\mathrm{eff}}^{(\uparrow,\mathrm{g})}(\mathbf{r}) & 0\\ 0 & -\frac{1}{2}\boldsymbol{\nabla}^2+V_{\mathrm{eff}}^{(\downarrow,\mathrm{g})}(\mathbf{r})\end{pmatrix}\underline{\mathsf{U}}^{(\mathrm{gr})}\,,\end{aligned}\tag{5.26}$$

with $V_{\mathrm{eff}}^{(\uparrow,\mathrm{g})}(\mathbf{r})=V_{\mathrm{eff}}(\mathbf{r})+B_{\mathrm{eff}}(\mathbf{r})$ and $V_{\mathrm{eff}}^{(\downarrow,\mathrm{g})}(\mathbf{r})=V_{\mathrm{eff}}(\mathbf{r})-B_{\mathrm{eff}}(\mathbf{r})$.

Thus, in the global spin-coordinate frame the spin-channels become decoupled and the two components of the rotated spinor $\underline{\mathsf{U}}^{(\mathrm{gr})}\boldsymbol{\psi}_i$ are associated with spin-up ($\sigma_1^{(\mathrm{g})}=\uparrow^{(\mathrm{g})}$) and spin-down ($\sigma_2^{(\mathrm{g})}=\downarrow^{(\mathrm{g})}$) components. The remaining task resembles now the problem of two non-magnetic problems with different effective potentials $V_{\mathrm{eff}}^{(\uparrow,\mathrm{g})}$ and $V_{\mathrm{eff}}^{(\downarrow,\mathrm{g})}$, that have to be solved using individual basis sets. Besides the Kohn-Sham eigenvalues $\{\epsilon_i\}$, the only coupling link between these problems is in the exchange-correlation energy $E_{\mathrm{xc}}(n,m_z^{(\mathrm{g})})$, that has to be recalculated within each iteration step.

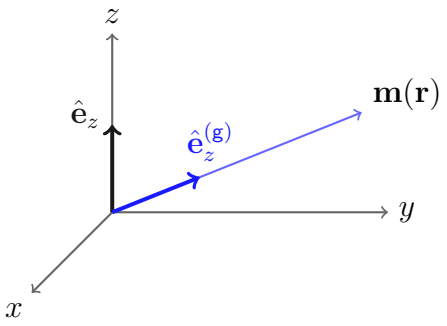

Fig. 5.3: $\hat{\mathbf{e}}_z^{(\mathrm{g})}$ with respect to real-space $\hat{\mathbf{e}}_z$.

If SOC is neglected, in a collinear calculation it is always possible to choose the SQA pointing into z-direction of real-space, without affecting the system's total energy. In that case, the rotation matrices $\underline{\mathsf{R}}^{(\mathrm{gr})}$ and $\underline{\mathsf{U}}^{(\mathrm{gr})}$ become unity matrices and the g-index can be dropped.

Non-collinear spin-configuration

For the description of a magnetic system with non-collinear spin density, a global spin-coordinate frame, in which the two spin-channels are decoupled throughout the crystal, is not provided anymore. By introducing a local spin-frame (l), that depends on the position and is connected to the global frame over rotation matrices $\underline{\mathsf{U}}^{(\mathrm{lg})}(\mathbf{r})$, the Hamiltonian can be transformed into a diagonal form, nonetheless. Within the FLEUR code, a non-collinear magnetic structure is described by the magnetization density

$$\mathbf{m}(\mathbf{r})=\begin{cases}m(\mathbf{r}_\mu)\hat{\mathbf{e}}_\mu & ,\quad \mathbf{r}\in\mathrm{MT}\ \mu\\ \mathbf{m}(\mathbf{r}) & ,\quad \text{else}\end{cases},\tag{5.27}$$

where the magnetic direction within the MTs is kept constant. The unit vector

$$\hat{\mathbf{e}}_\mu=\frac{\mathbf{M}}{|\mathbf{M}|}\ ,\ \mathbf{M}=\int_{\mathrm{MT}\mu}\mathbf{m}(\mathbf{r}')\mathrm{d}^3r'\tag{5.28}$$

denotes the average magnetic direction within the μth MT and is identical to the unit vector of the local-frame z-direction $\hat{\mathbf{e}}_z^{(\mathrm{l})}$. It is connected to the global coordinate system via the spin-rotation matrix $\underline{\mathsf{U}}^{(\mu)}$ constructed out of the two angles α_μ and β_μ, polar and azimuth angle, respectively. This allows to use basis functions constructed from $u_\ell^{(\sigma)}$ and $u_\ell^{(\sigma)}$ ($\sigma \in \{\uparrow, \downarrow\}$) in the local frame. Within each iteration step, the direction of the magnetization, and thus, the local frame is allowed to change in the IR, if desired also in the MTs. However, since the orientation converges while approaching a self-consistent solution, it is sufficient to only take the z-component of the magnetization in terms of the former local-frame into account when the new exchange potential is constructed [80, 81].

In the special case of a homogeneous spin-spiral (*cf.* Ch. 2) with spin-spiral vector $\mathbf{q}$ and magnetization direction

$$\mathbf{M}_\mu = M \begin{pmatrix} \cos(\mathbf{q}\cdot\mathbf{R}_\mu)\sin\vartheta \\ \sin(\mathbf{q}\cdot\mathbf{R}_\mu)\sin\vartheta \\ \cos\vartheta \end{pmatrix} \text{ with the cone angle } \vartheta\,, \tag{5.29}$$

it would be desirable to use a basis function set, that already fulfills the generalized Bloch theorem. This is achieved by multiplying a phase factor $\mathrm{e}^{\mp \mathrm{i}\frac{\mathbf{q}}{2}\cdot\mathbf{r}}$ to the LAPW basis function in the IR and the VRs. In addition, the functions $\{v_{\ell\sigma}\}$ and $\{\dot{v}_{\ell\sigma}\}$ are determined as solutions to differential equations, that are the spin-resolved analogues to Eqs. (5.22) and (5.23), except that $\mathbf{K}_\parallel^2$ is replaced by $(\mathbf{K}_\parallel \mp \mathbf{q})^2$. The basis functions within MT μ is defined with respect to the local frame therein. As usual, the A- and B-coefficients are constructed such, that the basis function and its derivative are continuous for every ℓ-channel up to a chosen $\ell_{\max}$ at the boundaries to the IR.

5.5.1 Spin-Orbit Coupling within the fleur code

Because of its relativistic origin, SOC normally gives only a small impact on the total energy compared to the energetic contributions of the scalar-relativistic part of the Hamiltonian. Therefore, as an approximation in FLAPW calculations it is restricted to the MTs only [82], where $\boldsymbol{\nabla} V_{\mathrm{eff}}(\mathbf{r})$ (*cf.* Eq. (4.24)) is largest [82], whereas in the IR and the VRs it is neglected. Then, Eq. (4.27) is simplified to

$$\underline{H}_{\mathrm{SO}}(\mathbf{r}) = \sum_\mu \underbrace{\Theta\left(R_\mu^{\mathrm{MT}} - r_\mu\right)\xi_\mu(r_\mu)\underline{\boldsymbol{\sigma}}\cdot\hat{\mathbf{L}}^{(\mu)}}_{\underline{H}_{\mathrm{SO}}^{(\mu)}(\mathbf{r})} \quad , \; \underline{\boldsymbol{\sigma}}\cdot\hat{\mathbf{L}}^{(\mu)} = \begin{pmatrix} \hat{L}_z^{(\mu)} & \hat{L}_-^{(\mu)} \\ \hat{L}_+^{(\mu)} & -\hat{L}_z^{(\mu)} \end{pmatrix}, \tag{5.30}$$

where $\hat{L}_\pm^{(\mu)} = \hat{L}_x^{(\mu)} \pm \mathrm{i}\hat{L}_y^{(\mu)}$ and R_μ^{MT} is the MT radius of the μth atom. As pointed out previously, the magnetization direction and therefore the SQA is assumed to be constant within a MT sphere. Using the spin-rotation matrix $\underline{\mathsf{U}}^{(\mu)}$, the Hamiltonian for the SOC contribution within one MT sphere, $\underline{H}_{\mathrm{SO}}^{(\mu)} = \underline{H}_{\mathrm{SO}}^{(\mu,\mathrm{g})}$, can be rotated into the local frame,

in which it is diagonal,

$$\underline{H}_{\mathrm{SO}}^{(\mu,\mathrm{g})}(\mathbf{r}) = \underline{\mathsf{U}}^{(\mu)\,\dagger}(\mathbf{r}) \underbrace{\left[\Theta\left(R_\mu^{\mathrm{MT}} - r_\mu\right)\xi_\mu(r_\mu)\begin{pmatrix}\hat{L}_{\tilde{z}}^{(\mu,\mathrm{l})} & 0\\ 0 & -\hat{L}_{\tilde{z}}^{(\mu,\mathrm{l})}\end{pmatrix}\right]}_{\underline{H}_{\mathrm{SO}}^{(\mu,\mathrm{l})}} \underline{\mathsf{U}}^{(\mu)}(\mathbf{r})\,. \tag{5.31}$$

Due to the decoupling of the two spin-channels in the diagonal form, both Hamiltonians can be solved (diagonalized) independently from each other. This takes approximately twice the time of a calculation neglecting the spin, whereas the diagonalization of the full Hamiltonian scales with the third power of the size (number of columns, rows). Thus, solving the problem in the block-diagonal form of Eq. (5.31) saves a factor of about $2^3/2 = 4$.

Depending on the physical quantity that is investigated, $\underline{H}_{\mathrm{SO}}$ is calculated or approximated differently. In this thesis, the magnetocrystalline anisotropy (*cf.* Sec. 2.2.2) is calculated using a scheme called *second variation* and the Dzyaloshinskii-Moriya interaction (*cf.* Sec. 2.2.1)is obtained by treating SOC as a first-order perturbation. In both cases, the force theorem is used, to derive the presented results. Both procedures will be discussed in the following.

First-Order Perturbation Theory

If $\underline{H}_{\mathrm{SO}}$ is treated as perturbation to the scalar-relativistic Hamiltonian $H_{\mathrm{SR}}\underline{\mathbb{1}}$, the energy correction in first order perturbation theory is given by the expectation value of $\underline{H}_{\mathrm{SO}}$ with respect to the unperturbed wave-function spinor components $\psi_\sigma^{(\mathrm{SR})}(\mathbf{r}) = \sum_{\mathbf{K}} c_{\mathbf{K},\sigma}\varphi_{\mathbf{K},\sigma}^{\mathrm{LAPW}}(\mathbf{r})$,

$$\begin{aligned}\Delta\mathrm{E} &= \int \boldsymbol{\psi}^{(\mathrm{SR})}(\mathbf{r}')^\dagger \underline{H}_{\mathrm{SO}}(\mathbf{r}')\boldsymbol{\psi}^{(\mathrm{SR})}(\mathbf{r}')\mathrm{d}^3r'\\ &= \sum_\mu \sum_{\mathbf{K},\mathbf{K}'} \int_{\mathrm{MT}\mu} \begin{pmatrix} c_{\mathbf{K},\sigma_1}\varphi_{\mathbf{K},\sigma_1}^{\mathrm{LAPW}}(\mathbf{r}')\\ c_{\mathbf{K},\sigma_2}\varphi_{\mathbf{K},\sigma_2}^{\mathrm{LAPW}}(\mathbf{r}')\end{pmatrix}^\dagger \underline{H}_{\mathrm{SO}}^{(\mu)}(\mathbf{r}') \begin{pmatrix} c_{\mathbf{K}',\sigma_1}\varphi_{\mathbf{K}',\sigma_1}^{\mathrm{LAPW}}(\mathbf{r}')\\ c_{\mathbf{K}',\sigma_2}\varphi_{\mathbf{K}',\sigma_2}^{\mathrm{LAPW}}(\mathbf{r}')\end{pmatrix} \mathrm{d}^3r'\,.\end{aligned} \tag{5.32}$$

For a spin-spiral calculation with a constant spin-spiral vector $\mathbf{q}$, the unperturbed wave functions $\{\boldsymbol{\varphi}_{\mathbf{K}}^{\mathrm{LAPW}}\}$ fulfill the general Bloch theorem, so that they can be written

$$\boldsymbol{\varphi}_{\mathbf{K}}^{\mathrm{LAPW}}(\mathbf{r}) = \begin{pmatrix} \mathrm{e}^{\mathrm{i}\left(\mathbf{k}-\frac{\mathbf{q}}{2}\right)\cdot\mathbf{r}} w_{\mathbf{K}}^{(\uparrow,\mathrm{g})}(\mathbf{r})\\ \mathrm{e}^{\mathrm{i}\left(\mathbf{k}+\frac{\mathbf{q}}{2}\right)\cdot\mathbf{r}} w_{\mathbf{K}}^{(\downarrow,\mathrm{g})}(\mathbf{r})\end{pmatrix} \quad,\; w_{\mathbf{K}}^{(\sigma)}(\mathbf{r}+\mathbf{R}) = w_{\mathbf{K}}^{(\sigma)}(\mathbf{r})\,. \tag{5.33}$$

Since $\underline{H}_{\mathrm{SO}}(\mathbf{r})$ is lattice periodic, it is straightforward to show that

$$\underline{H}_{\mathrm{SO}}(\mathbf{r}) \begin{pmatrix} \mathrm{e}^{\mathrm{i}\left(\mathbf{k}-\frac{\mathbf{q}}{2}\right)\cdot\mathbf{r}} w_{\mathbf{K}}^{(\uparrow,\mathrm{g})}(\mathbf{r})\\ \mathrm{e}^{\mathrm{i}\left(\mathbf{k}+\frac{\mathbf{q}}{2}\right)\cdot\mathbf{r}} w_{\mathbf{K}}^{(\downarrow,\mathrm{g})}(\mathbf{r})\end{pmatrix} = \begin{pmatrix} \mathrm{e}^{\mathrm{i}\left(\mathbf{k}-\frac{\mathbf{q}}{2}\right)\cdot\mathbf{r}} \tilde{w}_{\mathbf{K}}^{(\uparrow,\mathrm{g})}(\mathbf{r})\\ \mathrm{e}^{\mathrm{i}\left(\mathbf{k}+\frac{\mathbf{q}}{2}\right)\cdot\mathbf{r}} \tilde{w}_{\mathbf{K}}^{(\downarrow,\mathrm{g})}(\mathbf{r})\end{pmatrix} \quad,\; \tilde{w}_{\mathbf{K}}^{(\sigma)}(\mathbf{r}+\mathbf{R}) = \tilde{w}_{\mathbf{K}}^{(\sigma)}(\mathbf{r})\,. \tag{5.34}$$

The contributions of the off-diagonal $(\mathbf{k}\mathbf{k}')$-matrix elements in Eq. (5.32) cancel out, if summed over a supercell of $\mathrm{N} \geq 2$ chemical cells, accounting for both, the crystal and

the magnetic periodicity. With a lattice vector $\mathbf{R}$ that fulfills $\mathbf{R}\cdot\mathbf{q} = \frac{2\pi}{N}$, they read

$$\begin{aligned}
&\sum_{j=0}^{\mathrm{N}-1}\int_{\mathrm{MT}\mu}\varphi^{\mathrm{LAPW}}_{\mathbf{K},\sigma_1}(\mathbf{r}'+j\cdot\mathbf{R})^* H^{(\mu)}_{\mathrm{SO},\sigma_1\sigma_2}(\mathbf{r}'+j\cdot\mathbf{R})\varphi^{\mathrm{LAPW}}_{\mathbf{K}',\sigma_2}(\mathbf{r}'+j\cdot\mathbf{R})\mathrm{d}^3r' \\
= &\sum_{j=0}^{\mathrm{N}-1}\int_{\mathrm{MT}\mu}\mathrm{e}^{\mathrm{i}\mathbf{q}\cdot(\mathbf{r}'+j\cdot\mathbf{R})} w^{(\uparrow,\mathrm{g})}_{\mathbf{K}}(\mathbf{r}')^*\tilde{w}^{(\downarrow,\mathrm{g})}_{\mathbf{K}'}(\mathbf{r}')\mathrm{d}^3r' \\
= &\underbrace{\left(\sum_{j=0}^{\mathrm{N}-1}\mathrm{e}^{\mathrm{i}\frac{2\pi}{\mathrm{N}}\cdot j}\right)}_{=\delta_{\mathrm{N},1}}\int_{\mathrm{MT}\mu}\mathrm{e}^{\mathrm{i}\mathbf{q}\cdot\mathbf{r}'} w^{(\uparrow,\mathrm{g})}_{\mathbf{K}}(\mathbf{r}')^*\tilde{w}^{(\downarrow,\mathrm{g})}_{\mathbf{K}'}(\mathbf{r}')\mathrm{d}^3r' \underset{N\geq 2}{=} 0
\end{aligned} \tag{5.35}$$

Thus, the expression in Eq. (5.32) can be simplified to

$$\Delta\mathrm{E} = \sum_{\mu}\sum_{\mathbf{K},\mathbf{K}'}\int_{\mathrm{MT}\mu}\left[w^{(\uparrow,\mathrm{g})}_{\mathbf{K}}(\mathbf{r}')^*\tilde{w}^{(\uparrow,\mathrm{g})}_{\mathbf{K}'}(\mathbf{r}') + w^{(\downarrow,\mathrm{g})}_{\mathbf{K}}(\mathbf{r}')^*\tilde{w}^{(\downarrow,\mathrm{g})}_{\mathbf{K}'}(\mathbf{r}')\right]\mathrm{d}^3r'\,. \tag{5.36}$$

In conclusion we have

$$\Delta\mathrm{E} = \sum_{\substack{\mu,\mathbf{K},\mathbf{K}',\\(\sigma)=(\uparrow,\mathrm{g}),(\downarrow,\mathrm{g})}}\int_{\mathrm{MT}\mu}\left[w^{(\sigma)}_{\mathbf{K}}(\mathbf{r}')^*\underline{\mathrm{U}}^{(\mu)\ \dagger}\xi_\mu(r_\mu)\underline{\boldsymbol{\sigma}}\cdot\hat{\mathbf{L}}^{(\mu)}\underline{\mathrm{U}}^{(\mu)}w^{(\sigma)}_{\mathbf{K}'}(\mathbf{r}')\right]\mathrm{d}^3r' \tag{5.37}$$

$$\text{with}\quad \begin{pmatrix} w^{(\uparrow,\mathrm{g})}_{\mathbf{K}}(\mathbf{r}) \\ w^{(\downarrow,\mathrm{g})}_{\mathbf{K}}(\mathbf{r})\end{pmatrix} = \underline{\mathrm{U}}^{(\mu)}\sum_L Y_L(\hat{\mathbf{r}}_\mu)\begin{pmatrix} a^{(\mu)}_{\mathbf{K},L,(\uparrow,\mathrm{l})}u^{(\uparrow,\mathrm{l})}_\ell(r_\mu) + b^{(\mu)}_{\mathbf{K},L,(\uparrow,\mathrm{l})}\dot{u}^{(\uparrow,\mathrm{l})}_\ell(r_\mu) \\ a^{(\mu)}_{\mathbf{K},L,(\downarrow,\mathrm{l})}u^{(\downarrow,\mathrm{l})}_\ell(r_\mu) + b^{(\mu)}_{\mathbf{K},L,(\downarrow,\mathrm{l})}\dot{u}^{(\downarrow,\mathrm{l})}_\ell(r_\mu)\end{pmatrix}, \tag{5.38}$$

where $a^{(\mu)}_{\mathbf{K},L,\sigma} = c_{\mathbf{K},\sigma}A^{(\mu)}_{\mathbf{K},L,\sigma}$ and $b^{(\mu)}_{\mathbf{K},L,\sigma} = c_{\mathbf{K},\sigma}B^{(\mu)}_{\mathbf{K},L,\sigma}$. A more detailed review on how these values are calculated in the FLEUR code explicitly can be found *e.g.* in [83].

The expectation value of the orbital moment is calculated as well and in second order perturbation theory it is given by the expression [35]

$$\langle\mathbf{L}\rangle = \sum_{i,j}\frac{\langle\psi_i|\mathbf{L}|\psi_j\rangle\langle\psi_i|H_{\mathrm{SO}}|\psi_j\rangle}{\epsilon_i-\epsilon_j}w(\epsilon_i,\mathrm{T})\left(1-w(\epsilon_j,\mathrm{T})\right)\,, \tag{5.39}$$

where $w(\epsilon_i,\mathrm{T})$ is the Fermi-Dirac function from Eq. (5.17) and $i,j = \mathbf{k}\nu$. Its value is expected to be maximal at the minimum of the energy, *i.e.* when the spin moments are pointing into the direction of the easy axis (*cf.* Ch. 2).

Second Variation

As pointed out in the beginning of this chapter, it is of major importance to use a well-suited basis set, so that already a few basis functions are sufficient to describe the problem acceptably correct. A scheme in which the known eigenfunctions $\{\psi^{(0)}_\nu\}$ to a Hamiltonian H_0 are used as basis set for the full Hamiltonian $H = H_0 + H_1$ with the perturbation H_1 is called *second variation*.

For example, H_{SO} can be written within the basis of the unperturbed, scalar-relativistic basis functions. Within this thesis, however, this scheme is not used to describe the Hamiltonian of the spin-orbit coupling as perturbation, but a different orientation of the magnetic moments. The self-consistent solution to a Hamiltonian $H = H_{\mathrm{SR}} + H_{\mathrm{SO}}$ is used as unperturbed basis set.

6 Co chains deposited on Pt(664) Step-Edges

The following two Chapters 6 and 7 are dedicated to present the computational analysis of Co atoms and other transition metals (TMs) deposited in monatomic rows along Pt(664) step-edges. In the beginning of this chapter a brief summary of experimental and theoretical investigations that deal with this particular type of structure is given, followed by a detailed examination regarding the structural setup of the unit cell as it is used in the performed calculations. Then we describe and present computational analyses that have been carried out and that are suitable to obtain system-specific parameters, such as the spin stiffness constant A, the Dzyaloshinskii-vector (**D**-vector) and the anisotropy tensor $\underline{\mathsf{K}}$. As part of the investigation we show several convergence tests that help to appraise the reliability of the evaluated data. In the last part of this chapter we explore the two criteria for the appearance of homogeneous and inhomogeneous flat spin spirals, *cf.* Eqs. (2.39) and (2.52), respectively. The determined parameters enter the criteria as functions of the rotation axis $\hat{\mathbf{e}}_{\mathrm{rot}}$, *i.e.* the axis that is normal to the plane the spins are rotating in. Referring to these criteria a prediction about the resulting magnetic ground state in the Co chains concludes this chapter.

6.1 Current Experimental and Theoretical State of Understanding

Growing monatomic TM chains deposited along the step edges of a Pt(997) surface used as a template is a challenging task. Only a few years ago Dallmeyer, Gambardella and their collaborators succeeded in growing high density arrays of metal wires on vicinal Pt(997) surfaces [10, 84, 85]. Angle-resolved photoemission spectroscopy (ARPES) [10] or the combination of thermal energy atom scattering (TEAS) as real-time control device for a consistent wire deposition and scanning tunneling microscopy (STM) as investigation tool at the atomic scale [84, 85] allowed to determine the best deposition parameters such as the optimal temperature regime that lead to smooth single row TM wires. Historically the first examination of a truly 1D magnet, Co/Pt(997), and first magnetic measurements by X-ray magnetic circular dichroism (XMCD) was reported shortly after [11, 12]. Below a so-called blocking temperature of about $T_{\mathrm{B}} = 15\,\mathrm{K}$ the short-ranged magnetic order is transferred to a long-range ferromagnetic metastable state. The authors explain this ferromagnetic order with a large magnetic anisotropy energy (MAE) of $\Delta E = (2.0 \pm 0.2)\,\mathrm{meV}$ / Co atom and orbital magnetic anisotropy

(OMA) of $\Delta\mu = 0.12\,\mu_B$ in the plane perpendicular to the chains.

The success in growing and measuring 1D magnetic monatomic chain structures as well as the detection of unusual high anisotropy values encouraged the investigation from the theoretical point of view. Early studies from Komelj *et al.* [15] present the calculation of the XMCD spectra by means of a tight-binding linear muffin-tin orbital (LMTO) method and a full-potential linearized augmented plane-wave (FLAPW) calculation scheme, both of them including spin-orbit (SO) coupling. In order to approach the Pt(997) step-edged structure of the experiment [11] they analyzed Pt-supported and unsupported Co monolayer and Co chains in a repeated supercell structure. They concluded that the performed calculations are only comparable to the experimentally determined results by introducing an orbital-polarization term to the calculation scheme. Also, they found large orbital moments ($> 2\,\mu_B$) in the investigated unsupported wire structure. Shick *et al.* [16] investigated the easy axis direction by using a first-principles calculation scheme (FLAPW method) and found an easy axis direction that is tilted by 18° towards the Pt step-edge, which shows the correct tendency, but is not in qualitative agreement with experimental results (43° in Ref. [11]). The calculation of the MAE results in a value of about 4 meV/Co atom, which is two times larger than the experimental result. The authors expect a better agreement when measurements of the MAE are performed in the regime close to $T = 0\,\mathrm{K}$. An investigation of a finite Co-chain structure in a supercell structure is reported by Újfalussy *et al.* [17]. Their calculations are performed within a fully relativistic Green's function embedded cluster method. Although the edge atoms of the finite Co chain reveal a slightly larger orbital moment compared to the inner Co atoms ($0.25\,\mu_B$ and approximately $0.20\,\mu_B$, respectively), they are in satisfying agreement with the results of Gambardella *et al.* [11]. Furthermore the calculated easy axis (42° towards the Pt step-edge) differs only by 1° from the experimental result. The influence of the Pt substrate on the magnetic anisotropy is investigated by Komelj *et al.* [18] who performed calculations for Co and Fe chains deposited along Pt step-edges. They report on easy axis directions that are tilted by about 67° (Co chain) and about 10° (Fe chain) towards the step edge.

Up to now, all presented theoretical analyses deal with unit cells that simulate the (997)-surface by using narrow single-layer stripes of Pt atoms deposited on a wider Pt(111) superstructure. The Co chain is then deposited along one edge of these stripes. First investigations with a unit cell containing a true step-edged structure (Pt(664) step-edges, the (111) direction is tilted to the z-direction of the unit cell by about 10°) are presented by Baud *et al.* [19, 20]. These calculations are performed using the FLEUR code, which allows for a more detailed comparison to the results presented in this thesis. They investigated the effect of relaxation [19] and the deposition of multi-rows [20]. The latter showed a periodic behavior of the easy axis direction and strength of MAE as it has been reported in experiment [14]. Further investigations of the effect of relaxation were performed by Conte *et al.* [21] and for the case of a single Co atom placed on a Pt(111) surface [7]. In conclusion the analysis of a relaxed structure does not lead to more precise results, as the MAE is of the same order and the difference of the easy axis direction to experiment is larger [19]. The authors explain this by a larger hybridization of the Co orbitals with the Pt substrate as the Co atoms relax towards the step edge.

In conclusion one can state that up to now the focus of theoretical simulation lies on the analysis of anisotropy effects and the strength of orbital and magnetic moments. However, since the step-edged system provides a surface structure with a lack of inversion symmetry and the Pt substrate atoms exhibit large SO interaction, it is also fair to assume that the structure gives rise to a large Dzyaloshinskii-Moriya interaction (DMI) which might play a crucial role in the formation of the magnetic ground state, as it was reported for thin film systems, *e.g.* Mn/W(110) [4].

6.2 The investigated Structure and computational Parameters

The investigation of the step-edged surface structure is performed using the FLEUR code in the film geometry (*cf.* Sec. 5.4). The unit cell is visualized in Fig. 6.1. It contains a thin slab of 43 Pt atoms and two Co atoms placed above and underneath the substrate. Thus, the unit cell describes two monatomic chains that are deposited on both sides of the slab embedded in the step-edges along the $[\bar{1}10]$-direction, the y-axis of the unit cell. This results in two alternating layers along this direction, in the lower panel of Fig. 6.1 indicated by different color intensities and labeled front and back. Throughout this thesis no relaxation of the unit cell is considered. To ensure a periodic repetition of the structure along the x-direction the step surfaces with normal [111] are tilted by an angle of about 10°, so that the z-direction of the unit cell is [664] and the x-direction is $[11\bar{3}]$. The used lattice constant is $a = 7.543\,a_\mathrm{B} = 3.99\,\text{Å}$. Along the x-direction the unit cell has the length of the distance of two vicinal Co chains, $a_x = \sqrt{11}\cdot a \approx 13.24\,\text{Å}$. The width corresponds to the distance between two neighboring Co atoms within one chain, $a_y = \frac{a}{\sqrt{2}} \approx 2.82\,\text{Å}$ (also referred to as a_C). The distance between the two Co atoms at opposed sides within the unit cell is $\sqrt{2}\cdot a_x \approx 18.72\,\text{Å}$ and the interstitial region is confined by $|z| < \frac{D}{2} = 10.79\,\text{Å}$. The plane wave boundary for the basis functions in the interstitial region (IR) is chosen to $|z| < \frac{\tilde{D}}{2} = 11.95\,\text{Å}$. For all types of atoms, labeled by μ, the muffin-tin (MT) radius is chosen to be $R_\mu^\mathrm{MT} = 1.16\,\text{Å} < 1.41\,\text{Å}$, where the latter number is the maximum value meaning that neighboring MTs touch each other.

The cutoff values for the expansion of the Kohn-Sham potential (*cf.* Eq. (5.14)) are given by $\mathbf{G}_\mathrm{max} = 12.0\,a_\mathrm{B}^{-1}$ for the potential and $\mathbf{G}_\mathrm{max}^\mathrm{xc} = 9.5\,a_\mathrm{B}^{-1}$ for the exchange-correlation potential. For all 45 atoms the non-spherical part of the Hamiltonian is expanded up to $\ell_\mathrm{max}^\mathrm{n-sph} = 6$. The spherical harmonics in the LAPW basis function set are incorporated up to $\ell_\mathrm{max} = 8$ within each MT and the number of used basis functions is limited to $|\mathbf{K}_\parallel| = |\mathbf{k}_\parallel + \mathbf{G}_\parallel| < K_\mathrm{max}$. In most calculations $K_\mathrm{max} = 3.5\,a_\mathrm{B}^{-1}$ is used. In Section 6.3 calculations within this system will be tested with respect to this value.

The Bravais matrix of the unit cell contains the two vectors of the reciprocal space, $\mathbf{b}_1 = \left(\frac{2\pi}{a_x}, 0\right)$ and $\mathbf{b}_2 = \left(0, \frac{2\pi}{a_y}\right)$, and reads

$$\underline{B} = \begin{pmatrix}\mathbf{b}_1\\ \mathbf{b}_2\end{pmatrix} = \begin{pmatrix}\frac{2\pi}{a_x} & 0\\ 0 & \frac{2\pi}{a_y}\end{pmatrix} = \begin{pmatrix}0.25 & 0\\ 0 & 1.18\end{pmatrix} a_\mathrm{B}^{-1}\,. \tag{6.1}$$

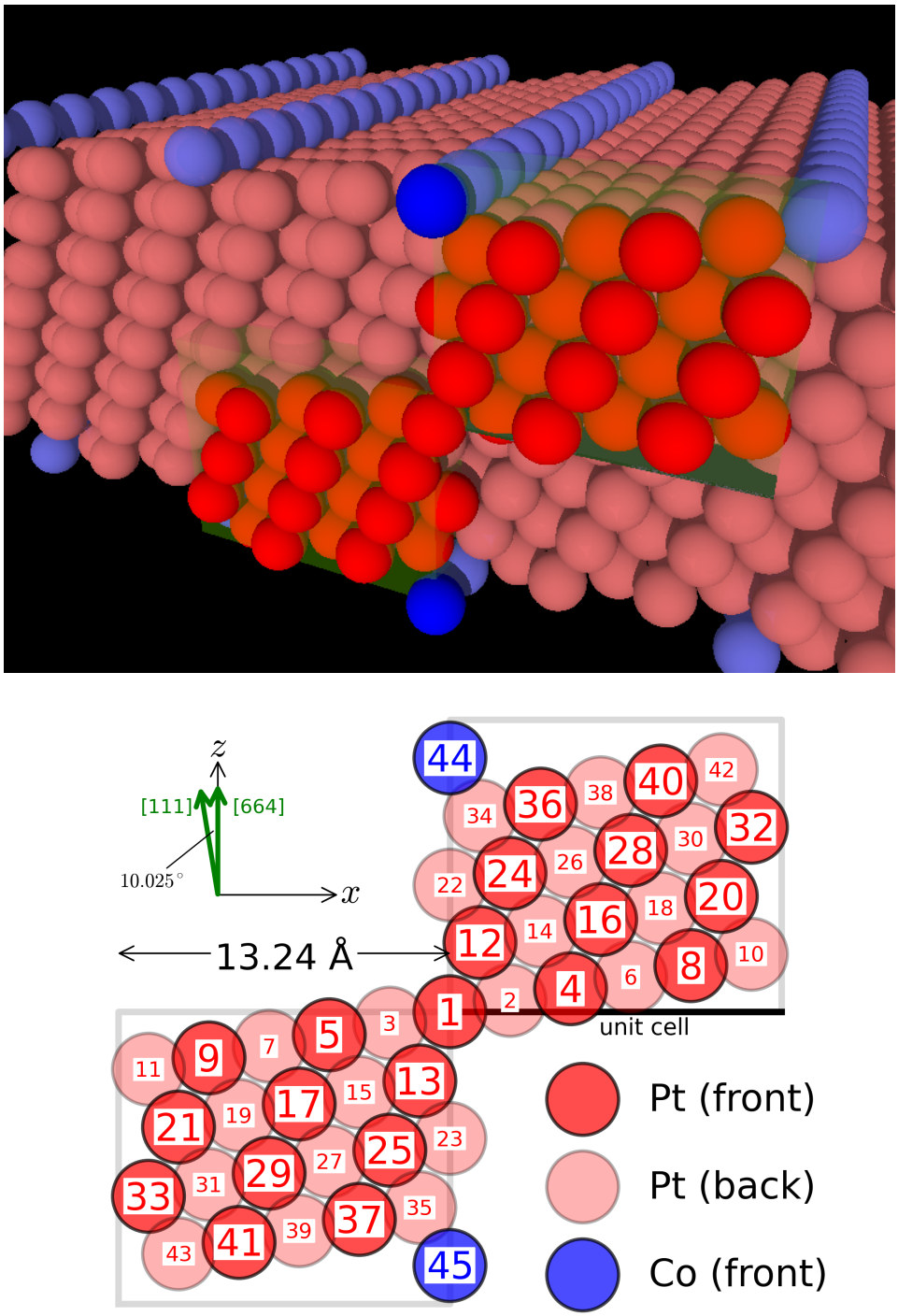

Fig. 6.1: These two figures illustrate the chemical structure that is investigated in this thesis. The lower panel shows a side view on the unit cell, whereas the upper panel shows how the repetition of unit cells in the xy-plane leads to the surface structure with repeated step edges along the x-direction. The blue circles correspond to the transition metals (Co in this chapter, Fe and Mn in the next) and the red circles represent the substrate atoms (Pt in all cases). The 2D unit cell is a black line in the side view and is 13.24 Å long and 2.82 Å deep.

Each **k**-point and **q**-vector can be expressed in units of theses reciprocal vectors by a dimensionless vector (denoted by a tilde $\tilde{\cdot}$):

$$\mathbf{k} = \tilde{\mathbf{k}} \cdot \underline{B} \quad \text{or} \quad \mathbf{q} = \tilde{\mathbf{q}} \cdot \underline{B}\,. \tag{6.2}$$

Because a spiral magnetic structure is only realizable along the y-direction in the Co chains, all investigated spiral vectors take the form $\mathbf{q} = (0, q_y) = \left(0, \tilde{q} \cdot \frac{2\pi}{a_y}\right)$.

The period length λ of the spiral is defined by the equation:

$$\varphi_{\text{period}} = \underbrace{\mathbf{q} \cdot \hat{\mathbf{e}}_y}_{=q_y} \lambda = \tilde{q} \cdot \frac{2\pi}{a_y} \cdot \lambda \stackrel{!}{=} 2\pi\,, \tag{6.3}$$

so that for a given value $\tilde{q}$ the period length reads

$$\lambda = \frac{a_y}{\tilde{q}} = \frac{0.282}{\tilde{q}}\text{nm}\,. \tag{6.4}$$

Instead of a_y we will use a_{C}, the nearest-neighbor distance within the chain, in the following.

In order to produce reliable results it is feasible to incorporate a large number of **k**-points within the performed calculations. Especially for the determination of the magnetocrystalline anisotropy (MCA) or the Dzyaloshinskii-vector (**D**-vector) small differences within the energy play a major role and a precise calculation of this quantity is mandatory. To investigate spiral structures with long ranged periodicity (equivalent to small **q**-vectors) along the chain direction, a denser sampling of the first BZ with **k**-points along the y-direction compared to the sampling along the x-direction is recommended. On the other hand the sampling of the BZ should be homogeneous, *i.e.* the distance among two adjacent **k**-points along the x-direction δk_x should be comparable to the distance along the y-direction δk_y. In the present calculations we used **k**-point sets with a ratio of

$$\frac{\delta k_x}{\delta k_y} = 1.7\,, \tag{6.5}$$

which means that the density along the **q**-vector is less than two times higher than in the direction perpendicular to **q**. In Fig. 6.2 the used **k**-point sets are shown.

6.3 Determination of the Spin Stiffness A

In this section, the study concerning the spin stiffness A of the investigated structure is presented. The performed calculations analyze the total energy as a function of the size of the spin spiral vector q.

The value of the spin stiffness describes the Heisenberg-type interaction and enters the previously discussed micromagnetic model (*cf.* Sec. 2.3) as a parameter. Although it cannot be excluded in the first place that A exhibits a dependency on the period length λ of a spiral magnetic structure, it is treated as a constant quantity of the underlying

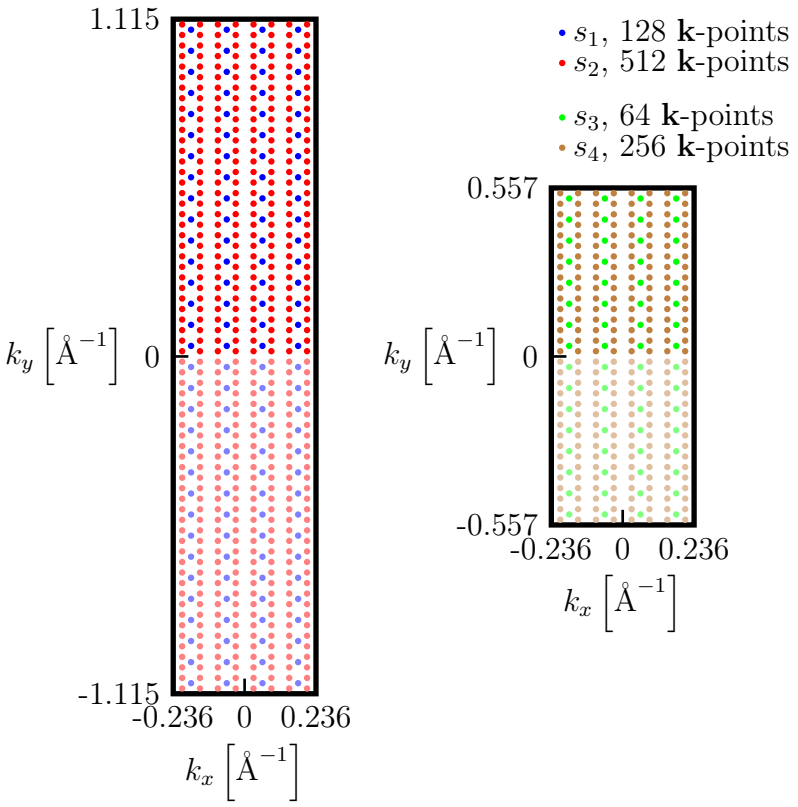

Fig. 6.2: This figure shows the different (two-dimensional) **k**-point sets. Hereafter, we will refer to them by s_i where i labels the four sets. On the left-hand side the unit cell of the investigated structure is shown, whereas the right BZ refers to a doubled unit cell which is used in the investigation of the Mn chains (see next chapter). This is due to the fact that Mn is arranged antiferromagnetically along the step-edges. The blue and the red dots correspond to a sampling of the whole Brillouin zone (BZ) with 128 and 512 **k**-points, respectively. The green and the brown dots correspond to a sampling of the whole Brillouin zone (BZ) with 64 and 256 **k**-points, respectively. For calculations that neglect SOC only the **k**-points of the upper half of the BZ are regarded (indicated by a darker color).

chemical system. By presenting and analyzing test calculations with respect to the number of used **k**-points and to $K_{\max}$, a cutoff parameter for the number of considered basis functions, in the following we investigate whether this assumption is justifiable.

The value of the spin stiffness is dominated by non-relativistic effects. Therefore, its determination is achieved by calculations in the scalar-relativistic (SR) approximation, so that effects induced by spin-orbit coupling (SOC) are not considered. By the use of the generalized Bloch theorem (*cf.* Sec. 4.3), the series of calculations with different **q**-vectors are restrictable to the chemical unit cell. In addition, the decoupling of spin and real space allows to diagonalize the Hamiltonian for each spin channel independently. Thus, this time-consuming part of the diagonalization experiences a speed-up by a factor of approximately 4 in the calculations, compared to the computation time of diagonalizing the full Hamiltonian. For small q-values the leading energy deviation to the energy of

the collinear magnetic structure is expected to depend quadratically on $\tilde{q} = \frac{a_C}{2\pi} \cdot q$,

$$E_{SR}(\tilde{q}) = \mathsf{A} \cdot \underbrace{\frac{\tilde{q}^2}{a_C^2}}_{=\lambda^{-2}} + E_{SR,0}\,, \tag{6.6}$$

where $E_{SR,0}$ is an energy offset and represents the energy value for $\tilde{q} = 0$.

By use of the self-consistency cycle (*cf.* Sec. 3.2.1) we calculated a charge density in the ferromagnetic order in the SR approximation up to a distance of $\Delta_{s-c} < 10^{-6}\,\frac{e}{a_B^3}$, where Δ_{s-c} represents a measure for the difference between the two charge densities before and after one iteration step. Due to symmetry considerations and performed test calculations the sampling of the BZ could be restricted to the upper half ($k_y > 0$), which results in a number of 64 used **k**. Then, we applied the force theorem (*cf.* Sec. 3.4.1), which means that for a series of different spiral lengths a single iteration step is calculated, where the previously determined self-consistent charge density is taken as starting point. The calculated series of the total energy with respect to q are shown in figure 6.3.

6.3.1 Testing the Convergence of the system

We have tested the value of A with respect to the number of used **k**-points and by varying the number of incorporated basis functions. The latter investigation was realized by performing calculations with different cutoff values K_{max} and only include basis functions $\varphi^{LAPW,2D}_{\mathbf{K}_\parallel \mp \frac{\mathbf{q}}{2}, \mathbf{G}_\perp}$ that fulfill [81]

$$|\mathbf{K}_\parallel \mp \frac{\mathbf{q}}{2}| = |\mathbf{k}_\parallel + \mathbf{G}_\parallel \mp \frac{\mathbf{q}}{2}| < K_{max}\,. \tag{6.7}$$

Thus, for each **k**-point a set of about 75 ($K_{max} = 3.2\,a_B^{-1}$), 99 ($K_{max} = 3.5\,a_B^{-1}$) or 126 ($K_{max} = 3.8\,a_B^{-1}$) basis functions per atom in the unit cell is set up. In the left panel of Fig. 6.3 the different series of performed calculations are shown. The spin stiffness constant is calculated for every data set by fitting the results with two functions of the form

$$f_1(\lambda) = \mathsf{A}_1 \cdot \lambda^{-2} \text{ and } f_2(\lambda) = \mathsf{A}_2 \cdot \lambda^{-2} + \mathsf{B}_2\,. \tag{6.8}$$

The latter function f_2 accounts for a possible error in the total energy that corresponds to the ferromagnetic spin alignment, $E_{SR,0}$, which is used as an energy offset. In the right panel of Fig. 6.3 two data sets (s_2,$K_{max,2}$ and s_2,$K_{max,3}$) with respect to λ^{-2} and for each set the two fits f_1 and f_2 are shown. For the fits only data with $\tilde{q}$-values in the regime $0.0 \leq \tilde{q} \leq 0.2$ are regarded, since the quadratic behavior is restricted to small q-values. The calculated values for the spin stiffness and the corresponding errors are shown in Table 6.1.

The general trend is that the spin stiffness lies in the order of about 100 meV nm^2, but the value of A cannot be regarded as converged with respect to both, the number of considered basis functions and the number of used **k**-points. However, the most accurate calculation setup (s_2, $K_{max,3}$) allows the prediction that a quadratic behavior in this $\tilde{q}$-point regime is justifiable: At first the two different fits seem to converge to the same

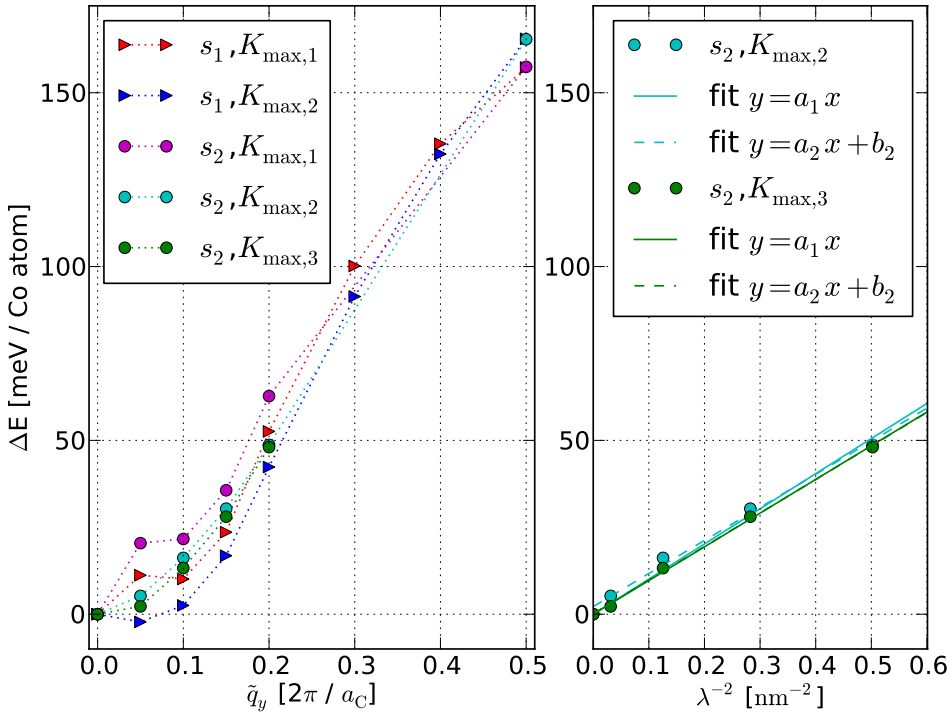

Fig. 6.3: In the left panel, the different series of calculated total energies are shown. The **k**-point set with label s_1 corresponds to calculations with 64 **k**-points and s_2 to those with the denser set of 256 **k**-points, where both sets are located in the upper BZ. The values $K_{\mathrm{max},1}$, $K_{\mathrm{max},2}$ and $K_{\mathrm{max},3}$ denote the values $3.2\,a_{\mathrm{B}}^{-1}$, $3.5\,a_{\mathrm{B}}^{-1}$ and $3.8\,a_{\mathrm{B}}^{-1}$, respectively. For two data series the right panel shows two fits, one with a fixed offset $b = 0$ and a truly linear fit accounting for an error with respect to the value of $E_{\mathrm{SR},0}$.

range of $\tilde{q}$ $\left[\frac{2\pi}{a_{\mathrm{C}}}\right]$	number of **k**-points	K_{max} $\left[a_{\mathrm{B}}^{-1}\right]$	$(\mathsf{A}_1 \pm \sigma_1)$ [meV nm^2/Co atom]	$(\mathsf{A}_2 \pm \sigma_2)$ [meV nm^2/Co atom]
0.0 ... 0.2	64	3.2	99.50 ± 8.39	95.28 ± 13.39
0.0 ... 0.2	64	3.5	75.31 ± 8.85	87.88 ± 10.43
0.0 ... 0.2	256	3.2	128.87 ± 14.75	107.83 ± 17.31
0.0 ... 0.2	256	3.5	101.05 ± 4.16	95.13 ± 4.89
0.0 ... 0.2	256	3.8	96.91 ± 1.37	96.50 ± 2.24

Tab. 6.1: Here are listed the values for the spin stiffness and the corresponding errors, as they result from the two different fits. In the most accurate calculation $(K_{\mathrm{max},3}, s_2)$, the value for the spin stiffness is nearly converged with respect to both parameters, the number of **k**-points and the number of regarded basis functions. Both fits seem to converge to the same value, whereas a fit of the form $y = a \cdot x + b$ shows less fluctuations with respect to A and is therefore more reliable than a fit of the form $y = a \cdot x$.

value of about $\mathsf{A} = 97\,\mathrm{meV\ nm^2/Co\ atom}$ and secondly, the error decreases for both fits, f_1 and f_2. If only the first four data points with $\tilde{q}$-values between 0.0 and 0.15 are taken into account the value of A decrease by about 20 % (for the **k**-point mesh s_1) or increase by about 5-10 % (for the **k**-point mesh s_2). In the following analysis a spin stiffness constant of $\mathsf{A} = 96.50\,\mathrm{meV\ nm^2/Co\ atom}$ is used, which represents the result for the most accurate data set and a fit of the form f_2.

6.4 The Anisotropy Tensor

In a crystal structure the total energy usually depends on the direction of the spin moments $\mathbf{m} = \mathbf{m}(\vartheta, \varphi)$ with respect to their orientation in real space, which is why it is crucial to include SOC in the performed calculations (*cf.* Sec. 2.2.2). Up to the second order in $\mathbf{m}$ it is possible to describe the magnetocrystalline anisotropy (MCA) energy $E_{\mathrm{MCA}}(\mathbf{m})$ by an anisotropy tensor $\underline{\mathsf{K}}$ (see Eq. (2.17)). To extract this tensor for the investigated structure, it is necessary to determine the three principal axis, namely the easy, medium and hard axis, and their directions with respect to the unit cell coordinates. This is realized by determining the energy series

$$\begin{matrix} E\left(\vartheta, \varphi = \ \ 0^\circ\right) \\ E\left(\vartheta, \varphi = 90^\circ\right) \end{matrix} \quad \text{with } \vartheta \in \{\pm 90^\circ, \pm 75^\circ, \pm 60^\circ, \pm 45^\circ, \pm 30^\circ, \pm 15^\circ, \quad 0^\circ\}\,. \tag{6.9}$$

Due to the absence of external magnetic fields and the time-inversion symmetry (see Eq. (2.18)) it is sufficient to restrict the calculations to $|\vartheta| \leq 90^\circ$.

To circumvent the huge computational demand of determining self-consistent solutions to the Kohn-Sham equations for every single spin moment direction, the force theorem is used (*cf.* Sec. 3.4.1). For spins pointing parallel to the chain direction (y-direction, $\vartheta = \varphi = 90^\circ$) a self-consistent solution is determined up to a distance of $\Delta_{\mathrm{s-c}} < 10^{-6}\,\frac{e}{a_{\mathrm{B}}^3}$ between input and output charge densities. The number of used basis functions is approximately 100 per atom (corresponding to $K_{\max} = 3.5\,a_{\mathrm{B}}^{-1}$) and the used **k**-point set contains 128 **k**-points in the whole BZ. Then, for each investigated direction the resulting preconverged charge density is used to calculate the change in energy caused by a single iteration step. The resulting data sets are shown in Fig. 6.4. For the spin moments with $\varphi = 0^\circ$ an additional series is indicated in order to investigate the impact of the preconverged charge density and the force step on the resulting energies. The starting densities differ only in the direction of the magnetic moment which points in the direction of the chain (labeled inpl.) in one case and normal to the terrace surface (labeled oopl.) in the other case. As can be observed from the resulting energies, the effect is small compared to most energy differences within one series.

Due to the fact that the terrace normal and the z-direction of the unit cell (referred to as $\cdot_{\mathrm{u.c.}}$) enclose an angle of about 10°, the spin quantization axis used in the calculations and shown in the figure are connected via a rotation in the xz-plane. The resulting pairs of angles are displayed in Table 6.2.

The total energy as function of the spin moments pointing towards the normal direction of the terrace (out-of plane, $\vartheta = \varphi = 0^\circ$) is part of both data sets, $\varphi = 0^\circ$ and

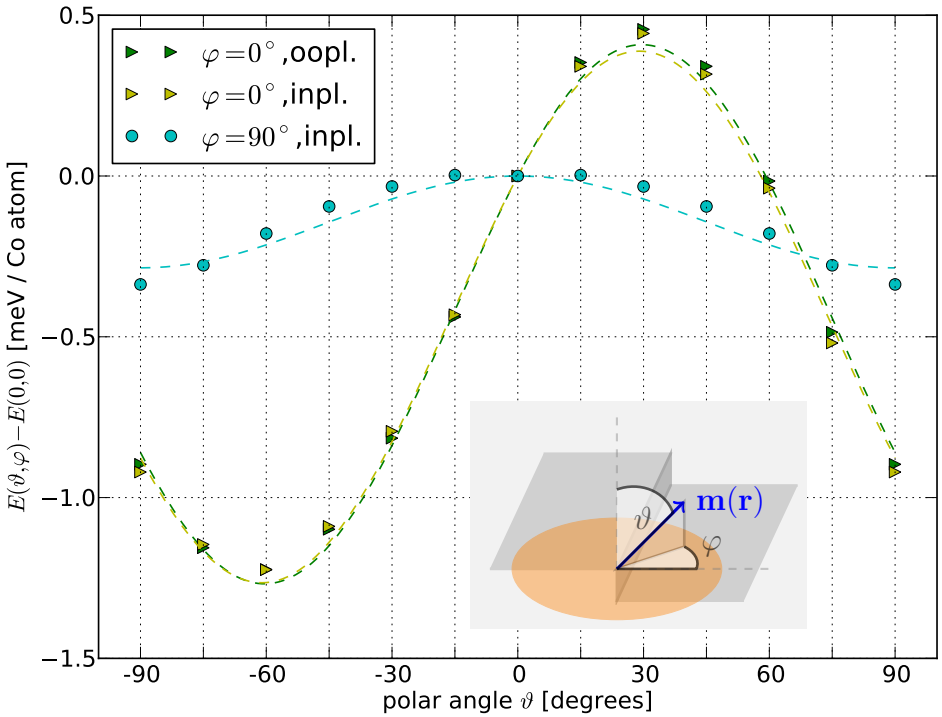

Fig. 6.4: To extract the MCA energy we determined the energy for different collinear spin alignments. In the case of $\varphi = 0°$ the xz-plane and in the case of $\varphi = 90°$ the yz-plane is sampled. Additionally, the former data set is collected using two different charge densities as a starting point, one with spins pointing along the z-direction (oopl.) and the other in y-direction (inpl.). The resulting energy determined by the force theorem is not affected much by the choice of the starting potential.

ϑ	φ	$\vartheta_{\text{u.c.}}$	$\varphi_{\text{u.c.}}$	ϑ	φ	$\vartheta_{\text{u.c.}}$	$\varphi_{\text{u.c.}}$
-90	0	100.025	180	-90	90	90.000	270.000
-75	0	85.025	180	-75	90	75.234	267.329
-60	0	70.025	180	-60	90	60.504	264.261
-45	0	55.025	180	-45	90	45.868	260.125
-30	0	40.025	180	-30	90	31.482	253.221
-15	0	25.025	180	-15	90	17.978	236.990
0	0	10.025	180	0	90	10.025	180.000
15	0	4.975	0	15	90	17.978	123.011
30	0	19.975	0	30	90	31.482	106.779
45	0	34.975	0	45	90	45.868	99.875
60	0	49.975	0	60	90	60.504	95.739
75	0	64.975	0	75	90	75.234	92.671
90	0	79.975	0	90	90	90.000	90.000

Tab. 6.2: Here are listed the spherical angles ϑ and φ with respect to the (111)-direction (out-of plane) in degrees and the corresponding values $\vartheta_{\text{u.c.}}$ and $\varphi_{\text{u.c.}}$ with respect to the coordinate system of the unit cell.

$\varphi = 90°$, respectively. Therefore, the functions that are fitted to the data sets read

$$E_{\text{fit}}(\vartheta, \varphi) = A_\varphi \cdot \left[\cos^2(\vartheta + B_\varphi) - \cos^2(B_\varphi)\right] , \tag{6.10}$$

where A_φ and B_φ are two fitting parameters. This type of function already accounts for a data comprehensive energy offset since $E_{\text{fit}}(0,0) = 0$. Thus it is ensured that the relative energy value for the principal axis pointing along the chain direction is given with reference to the values of the other two principal axis that are located within the xz-plane, along two directions perpendicular to each other.

Evaluating the extrema of the fit functions for the data sets labeled 'inpl.' we extract the values for the three principal axes:

$$\begin{array}{rcrcl} \mathsf{k}_1 & = & E_{\text{fit}}(\vartheta = -61°, \varphi = \ \ 0°) & = & -1.26\,\text{meV / Co atom} , \\ \mathsf{k}_2 & = & E_{\text{fit}}(\vartheta = \ \ 90°, \varphi = 90°) & = & -0.29\,\text{meV / Co atom} , \\ \mathsf{k}_3 & = & E_{\text{fit}}(\vartheta = \ \ 29°, \varphi = \ \ 0°) & = & \ \ 0.39\,\text{meV / Co atom} . \end{array} \tag{6.11}$$

The easy axis is tilted by $\vartheta_{\text{easy}} = -61°$ with respect to the (111)-surface towards the upper terrace. In the case of the data set with the charge density preconverged with spin moments pointing in z-direction ('oopl'), we find an angle of $-60°$ and $\mathsf{k}_1 = -1.27\,\text{meV}$ and $\mathsf{k}_3 = 0.41\,\text{meV}$ per Co atom. The energy difference of easy and hard axis is about 1.7 meV, which is comparable to experimental results ((2.0 ± 0.2) meV / Co atom in the experiment of Gambardella *et al.* [11]). Although the tendency of the direction of k_1 is in agreement with previous experimental and theoretical studies, the tilting of the easy axis towards the upper terrace is overestimated by almost 20° compared to experiment ($\vartheta_{\text{easy}} = 43°$ in [11]). To explore the origin of this instance we will approach the determination of the angle ϑ_{easy} by exploring the orbital moment and by following the calculation scheme used by Baud *et al.* [19].

6.4.1 Determination of the Easy Axis Direction

As pointed out in Eq. (5.39) of Section 5.5.1, the expectation value of the orbital moment is expected to be maximal, when the spin moments are constrained in a direction nearby the easy axis direction. This instance can be used to determine the easy axis by use of a different approach besides the investigation of the total energy. For a selective number of atoms (Co atom and a choice of particular Pt atoms nearby) the calculated relative orbital moments are shown in Fig. 6.5. These quantities are given with respect to the corresponding values when the spin moments point in the (111)-direction ($\vartheta = 0$).

Apparently, the maximum of the Co orbital moment is reached for $\vartheta = -36°$ with a value of $0.203\,\mu_{\text{B}}$ and an orbital moment anisotropy (OMA) of about $0.049\,\mu_{\text{B}}$). Two of the Pt atoms that are located at the surface next to the chain show the largest anisotropies induced in the substrate (atoms labeled 40: OMA of $0.017\,\mu_{\text{B}}$, atoms labeled 42: OMA of $0.019\,\mu_{\text{B}}$). Their maxima are reached for $\vartheta_{\text{max}} = -81°$ (Pt atom 40) and $\vartheta_{\text{max}} = -78°$ (Pt atom 42). Summing up over all orbital moments of atoms (labeled 2,4,...,44), a maximum at $\vartheta = -52°$ is found which is in better agreement to the calculated easy axis by the investigation of the total energy ($\vartheta_{\text{easy}} = 61°$). Still it is

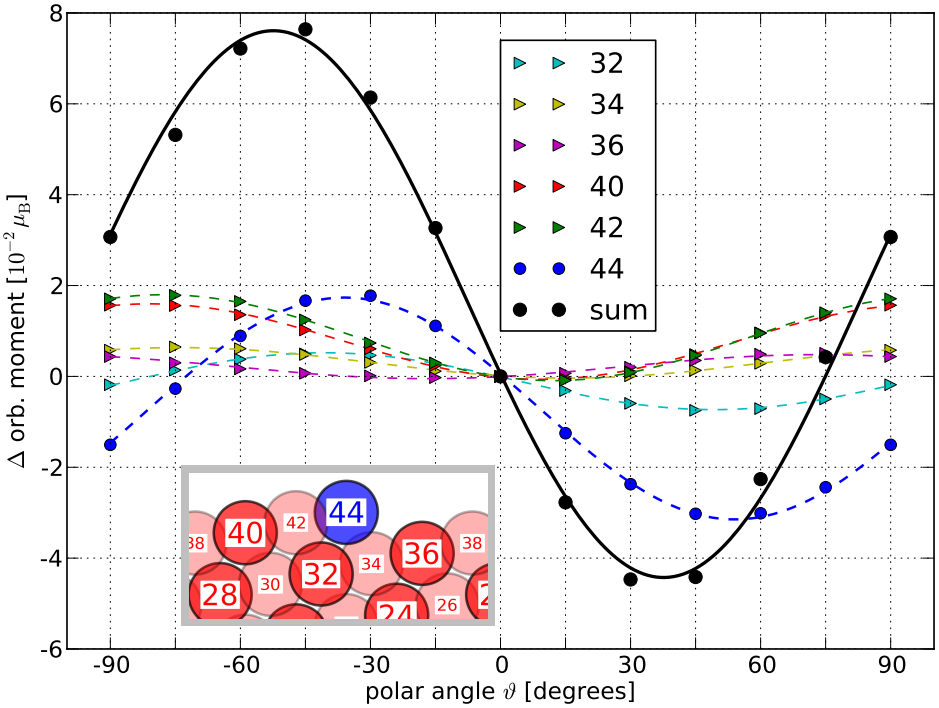

Fig. 6.5: In this figure the orbital moment anisotropies of several selected atoms with respect to the xz-plane are shown. Note that these values are not absolute quantities, but represent the difference to the corresponding orbital moment when the Co spin moment is oriented normal to the surface ($\vartheta = 0$). It shows that the sum of orbital moments (black dots) is a compromise of the orbital moment of the Co atom (blue data) and mainly two nearby Pt atoms contributions, labeled 40 and 42. Thus, the maximal value of $-35°$ of the Co atom only is directed towards the upper terrace, resulting in a maximum of the sum over all orbital moments at $-52°$. In addition, it is remarkable that the anisotropy of the atom labeled 34 is of minor importance, although it is one of three next-neighbors to the Co atom.

label of atom	L_{max} [μ_B]	ϑ_{max} [degrees]	OMA [μ_B]
32	0.037	-41	0.013
34	0.046	-74	0.007
36	0.012	73	0.005
40	0.016	-81	0.017
42	0.062	-78	0.019
44	0.203	-36	0.049
sum$(2, 4, \ldots, 44)$	0.786	-52	0.120

Tab. 6.3: In this table the maximal values for the orbital moments of the Co atom and a selection of Pt atoms nearby the chain are shown. In addition the corresponding polar angle ϑ is given and the orbital magnetic anisotropy (OMA). The labels correspond to the inset picture in Fig. 6.5.

	xc-potential	$K_{\max}$ $[a_B^{-1}]$	inv. sym.	ϑ_{easy} [degrees]	ΔE_{easy} [meV]
series 1	LDA	3.5	no	-61	-1.26
series 2	LDA	3.2	no	-55	-0.68
series 3	LDA	3.2	yes	-55	-0.68
series 4	GGA	3.2	yes	-51	-1.26
Ref. [19]	GGA	3.2	yes	-52	-1.55

Tab. 6.4: Here are listed the results for the polar angle ϑ_{easy} of the easy axis direction and the difference $\Delta E_{\text{easy}} = E(\vartheta_{\text{easy}}) - E(\vartheta = 0)$ for different computational setups. In addition the results from Baud *et al.* [19] are listed. It appears that the easy axis direction is sensible to the chosen xc potential.

worthwhile to examine, why the easy axis differs from experimental results [11] by more than 10°.

As already mentioned in Section 6.1 the performed calculations and the presented analysis can be compared to previously published results by Baud *et al.* [19], as the presented data in this paper was calculated by use of the FLEUR code. The main differences to the performed calculations in this thesis are listed consecutively:

(1) A different approximation of the exchange correlation potential is used (*cf.* Sec. 3.3). Whereas Baud *et al.* used a general gradient approximation (GGA) scheme proposed by Perdew and Wang [60], in this thesis a local density approximation (LDA) derived by Moruzzi, Janak and Williams [63] is used.

(2) Whereas in this work nearly 100 basis functions per atom in the unit cell are considered (realized by a cutoff parameter of $K_{\max} = 3.5\, a_B^{-1}$), Baud *et al.* used $K_{\max} = 3.2\, a_B^{-1}$ or about 75 basis functions per atom.

(3) Baud *et al.* produced their results by using a FLEUR feature to take advantage of the inversion symmetry of the investigated structure, whereas in this examination all 45 atoms are treated as individual atom types.

In order to re-calculate the results of Ref. [19] we varied the parameters of the calculation in several test series (see Tab. 6.4). The results in terms of the MCA and the orbital moments are shown in Fig. 6.6.

Fortunately, the adoption of the three different adjustments used in [19] leads to results that are in good agreement with the reported outcomes. Especially the orbital moments and the easy axis direction are in accordance. The use of LDA leads to a further tilting of the easy axis towards the upper Pt terrace, so that the difference to the experimental value of 43° [11] is enlarged. On the other hand, the value of the MCA seems to describe the experimental value of about 2.0 meV better than the use of the GGA functional. In the concluding part of this chapter, we assume that the easy axis direction is given by $\vartheta = -61°$. Accounting for the presented analysis of the two exchange-correlation functionals, it is on the other hand advisable to treat the determination of the easy axis direction with care.

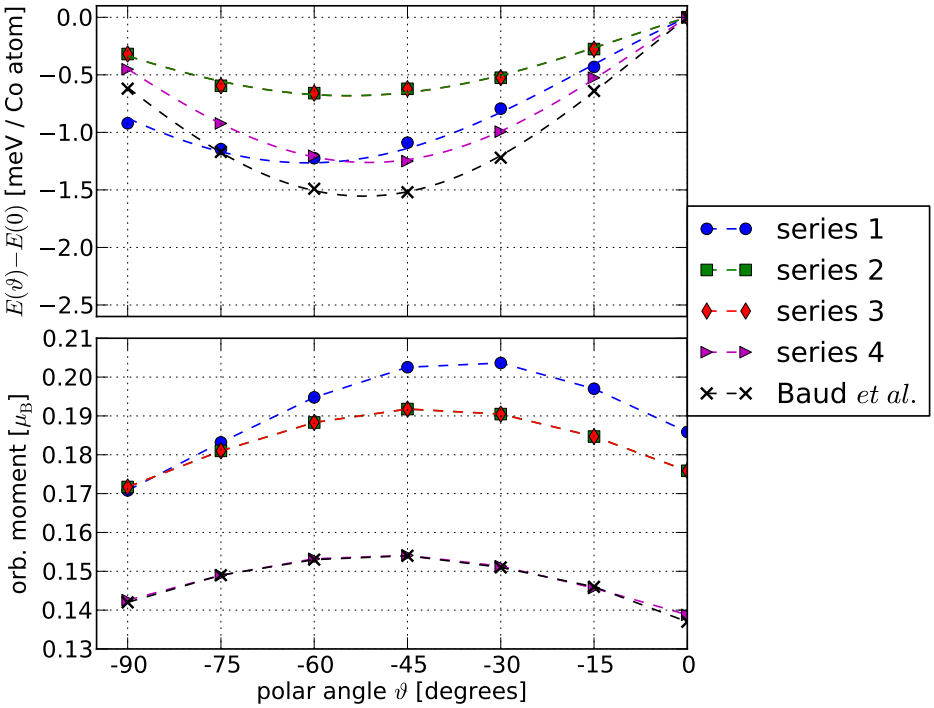

Fig. 6.6: In this figure an approach to the calculation scheme used in Ref. [19] is shown. In the upper panel the MCA is calculated and in the lower panel the orbital moments are shown. The accordance is satisfying, when all three parameters are adopted, whereas the easy axis tilted by about 10° towards the step edge by use of a different exchange-correlation potential approach.

6.5 Investigation of the Dzyaloshinskii-Moriya Interaction

The investigation of the DMI in a one-dimensional (1D) magnet is a new topic of scientific research and to our knowledge it is the first time to present calculations regarding this antisymmetric exchange interaction in a step-edged surface structure decorated with a monatomic chain. As pointed out in Chapter 2, a system with substrate atoms that have a large nuclear number and thus exhibit strong SO interaction can give rise to a large DMI, when in addition the structure lacks inversion symmetry.

The preconverged charge density is determined by incorporating 64 **k**-points in the upper half of the two-dimensional BZ (i.e. $k_y > 0$). To avoid errors occurring from rotation of the magnetic moments within the unit cell, the magnetization in the interstitial region (IR, *cf.* Sec. 5.1) is set to zero. Although at first sight, such a procedure seems to cause a large error in the resulting energies, it leads to more precise results. This is due to the fact that the induced error is of the same size for all calculations, whereas an error of non-rotated magnetization densities in the IR leads to a q-dependent error, which falsifies the results in a more crucial manner. By applying the force theorem, spin-spiral ground states for a series of different $\tilde{q}$-values are computed. The effect of SOC is calculated in first order perturbation theory and the resulting shift in the energy

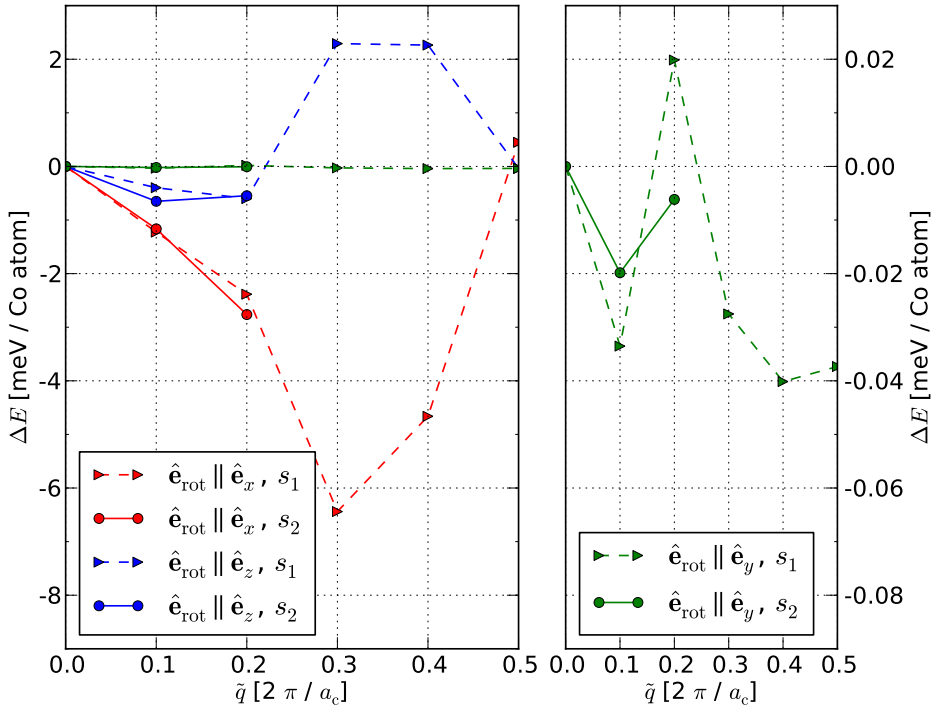

Fig. 6.7: Examination of the three components of the D-vector. The dashed lines correspond to calculations with 128 k-points, whereas the solid lines represent calculations with 512 k-points. The right panel shows the y-component enhanced by a factor of 100. Since the value decreases when the number of k-points in increased, the deviations from zero are attributed to numerical effects.

(compared to the accordant calculation where SOC is neglected) is given by ΔE.

6.5.1 The D-vector in Co/Pt(664)

Since the investigated structure exhibits only one mirror plane which is perpendicular to the y-direction, the **D**-vector is expected to be of the form (*cf.* Sec. 2.2.1)

$$\mathbf{D} = \begin{pmatrix} D_x \\ 0 \\ D_z \end{pmatrix} . \tag{6.12}$$

In order to determine D_x and D_z and to confirm that $D_y = 0$ we evaluated for every considered $\tilde{q}$-point three planar spin-spiral structures, for which the rotation axis $\hat{\mathbf{e}}_{\mathrm{rot}}$ is set parallel to $\hat{\mathbf{e}}_x$, $\hat{\mathbf{e}}_y$ and $\hat{\mathbf{e}}_z$. In Fig. 6.7 the performed calculations regarding all three components of the **D**-vector are shown up to the antiferromagnetic regime ($\tilde{q} = 0.0$ to $\tilde{q} = 0.5$). Additionally to a set of 128 **k**-points in the whole BZ (labeled s_1), a few calculations with a denser mesh of 512 **k**-points (labeled s_2) are shown. Whereas ΔE_x and ΔE_z (corresponding to $\hat{\mathbf{e}}_{\mathrm{rot}} \parallel \hat{\mathbf{e}}_x$ and $\hat{\mathbf{e}}_{\mathrm{rot}} \parallel \hat{\mathbf{e}}_z$, respectively) show a nearly linear course up to $\tilde{q} = 0.2$, the energy difference ΔE_y smaller by a factor of 100. The visible

$\lvert\Delta E(\vartheta_r = 70^\circ)\rvert$	1.2877 meV / Co atom
$\lvert\Delta E(\vartheta_r = 72^\circ)\rvert$	1.2884 meV / Co atom
$\lvert\Delta E(\vartheta_r = 74^\circ)\rvert$	1.2878 meV / Co atom
$\sqrt{(\Delta E_x)^2 + (\Delta E_z)^2}$	1.2884 meV / Co atom

Tab. 6.5: For a rotation axis of $\vartheta_r = 72^\circ$ the value of $|\Delta E(\vartheta_r)|$ becomes maximal and is identical to $\sqrt{(\Delta E_x)^2 + (\Delta E_z)^2}$.

fluctuation of ΔE_y decreases for a denser **k**-point mesh (see right panel of Fig. 6.7), so that the calculated difference to zero can be attributed to numerical inaccuracy.

In the following we present another set of performed calculations that determines the SO-induced energy correction term ΔE for different rotation axes

$$\vartheta_r \in \{0^\circ, 70^\circ, 72^\circ, 74^\circ, 90^\circ\}\,, \tag{6.13}$$

where the $\tilde{q}$-value ($\tilde{q} = 0.1$) and the **k**-point set (s_1) are kept fixed. The purpose of this examination is to test whether

$$\begin{aligned} \Delta E_x = \Delta E(\vartheta_r = 90^\circ) &= -1.2257\,\text{meV / Co atom} \\ \text{and}\quad \Delta E_z = \Delta E(\vartheta_r = \ 0^\circ) &= -0.3972\,\text{meV / Co atom}\,, \end{aligned}$$

taken from the calculations shown in Fig. 6.7, actually can be treated as components of a vector. If this was the case, we would expect a maximal value of $\Delta E = \sqrt{(\Delta E_x)^2 + (\Delta E_z)^2}$ for

$$\vartheta_r = \arctan\left(\frac{\Delta E_x}{\Delta E_z}\right) = 72^\circ\,.$$

The results are shown in Table 6.5. Indeed, the strength as well as the direction of a vector spanned by ΔE_x and ΔE_z is sufficiently well described by a calculation of these two energy differences. This result can also be interpreted as a strong indication that the **D**-vector is not affected by the rotation axis.

6.5.2 Influence of the Broadening Temperature

In order to calculate reliable values for the strength of **D** it is necessary to examine the role of the broadening temperature. This parameter determines the weight for the states near the Fermi energy, *i.e.* how they enter the total energy when SOC is included. In Fig. 6.7 this value is set to $k_\mathrm{B}T = 10^{-3}$ htr, which corresponds to approximately 27.21 meV or a broadening temperature of 316 K. Since the energy correction ΔE is in the order of 3 meV, it is advisable to explore the influence on the resulting **D**-vector components by decreasing the temperature down to $k_\mathrm{B}T = 10^{-5}$ htr. In Figs. 6.8 and 6.9 the results for the two investigated directions are shown. In addition, the values are listed in Table 6.6.

For both components, D_x and D_z the calculated data shows that the linear behavior in the regime for large broadening temperatures does not hold, when the value is decreased.

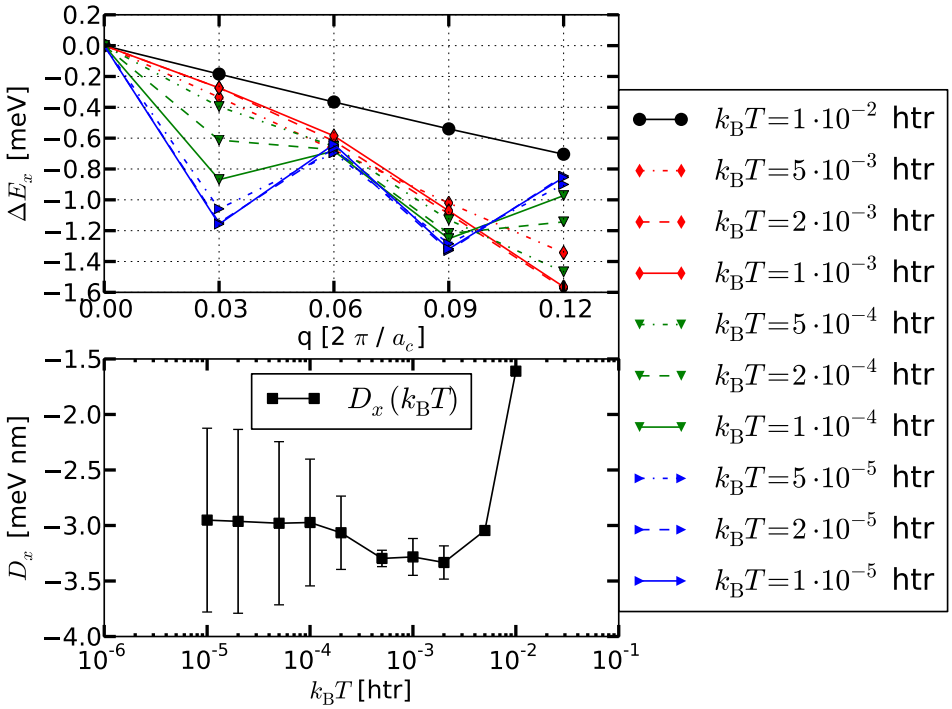

Fig. 6.8: This figure illustrates the variation of D_x, when the broadening temperature is varied from 3158 K (according to 10^{-2} htr) down to 3.2 K (according to 10^{-5} htr). Whereas the upper panel reveals an increasing nonlinear dependence of ΔE_x on the spiral length, when the temperature is decreased, the lower panel shows that a fit of the form $y = D \cdot x$ leads to a convergence of the D_x-component.

As for low temperatures, the crucial region around the Fermi energy is very narrow, only a dense **k**-point mesh is capable of describing the change in the energy properly. The resulting curves show that below a temperature of 158 K the linear dependency is superimposed by oscillations that we trace back to be caused by the limited number of considered **k**-points. Aside from a massively large fluctuation and a resulting large error for the linear fit, the value of the slope seems to converge in both cases (lower panel of both figures 6.8 and 6.9). The values and the corresponding errors are listed in Table 6.6. In the following we refer to the value of D_x and D_z that are calculated with the lowest broadening temperature, so that the **D**-vector takes the form

$$\mathbf{D} = \begin{pmatrix} -2.95 \\ 0 \\ -0.59 \end{pmatrix} \text{meV nm}\,. \tag{6.14}$$

6.5.3 Atom-resolved Contributions to DMI

The value of ΔE is the sum over the contributions that arise from each atom within the unit cell. In this sections we study the individual contributions to the SO-induced energy correction with respect to a formula that describes the DMI as an interaction of

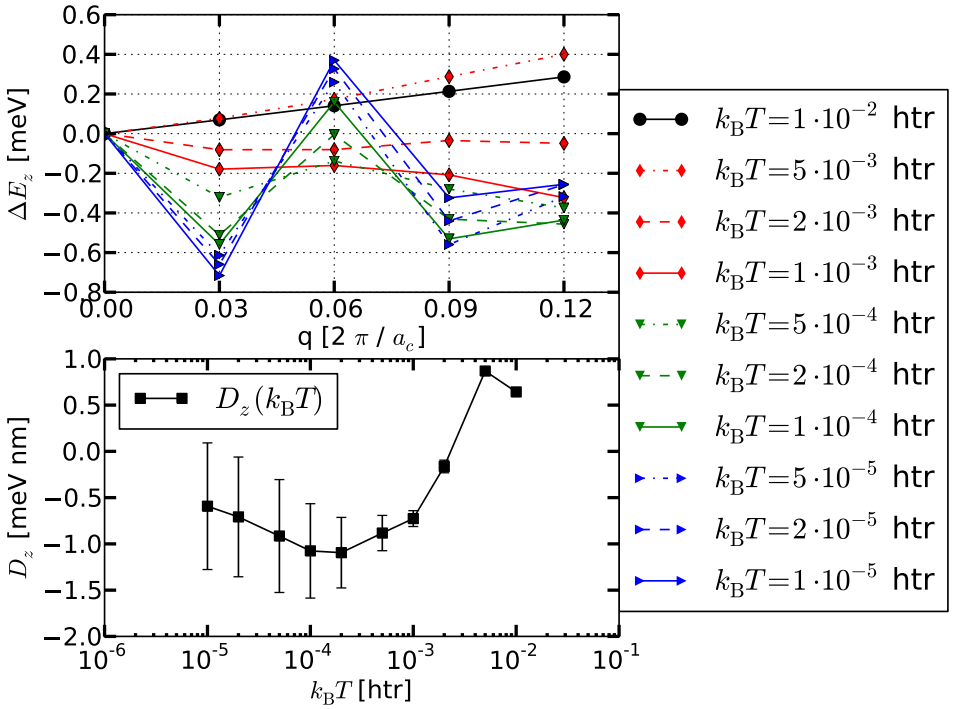

Fig. 6.9: This figure shows the analysis of D_z with respect to the broadening temperature. For explanations see the caption of Fig. 6.8. Also, the drawn conclusions resemble those given for D_x.

broad. temp. T [K]	$(D_x \pm \sigma_{D_x})$ [meV nm / Co atom]	$(D_z \pm \sigma_{D_z})$ [meV nm / Co atom]
3158	-1.61 ± 0.01	0.64 ± 0.002
1579	-3.05 ± 0.01	0.87 ± 0.03
631.6	-3.33 ± 0.15	-0.16 ± 0.07
315.8	-3.28 ± 0.17	-0.73 ± 0.09
157.9	-3.30 ± 0.07	-0.88 ± 0.19
63.2	-3.07 ± 0.33	-1.09 ± 0.38
31.6	-2.97 ± 0.57	-1.08 ± 0.51
15.8	-2.98 ± 0.73	-0.92 ± 0.61
6.3	-2.96 ± 0.83	-0.70 ± 0.65
3.2	-2.95 ± 0.83	-0.59 ± 0.68

Tab. 6.6: The calculated **D**-vector components D_x and D_z for different broadening temperatures are shown. They result from a linear fit of the form $y = D \cdot x$. On the one hand the error increases due to the nonlinear behavior at low temperatures, but on the other hand the value of the slope seems to converge in both cases.

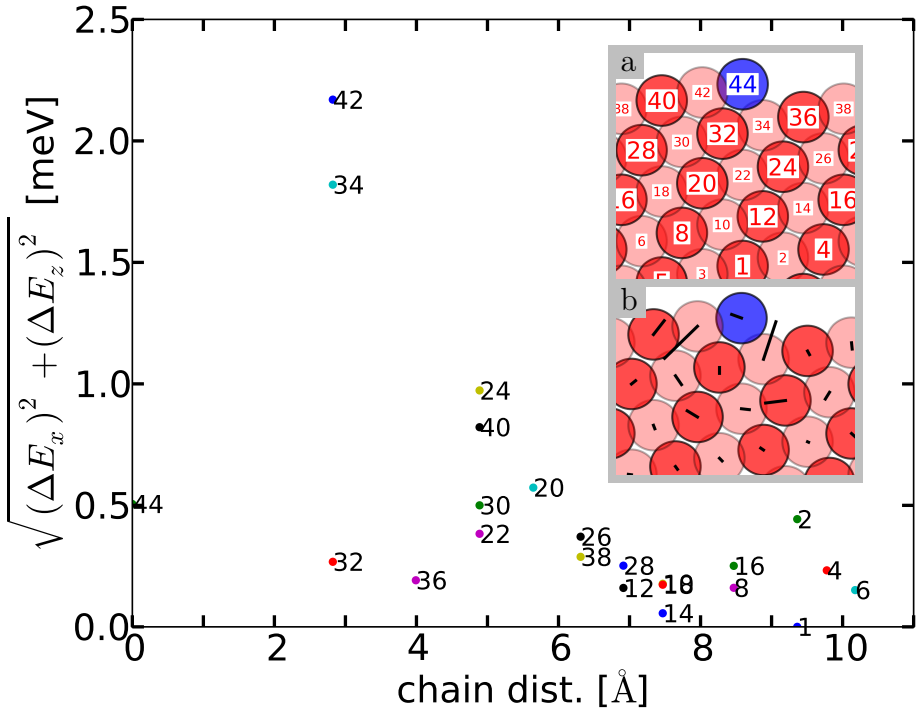

Fig. 6.10: The atom-resolved analysis of the different energy contributions shows that the strength of DMI decreases with larger distances to the nearest Co chain. Two of the three Pt atoms (34,42) show the largest contributions. On the other hand the third Pt atom (32) nearby the chain is not large, which is due to the fact that it is positioned in the same layer as the Co atom (indicated by a darker color compared to (34) and (42)) and therefore has a larger distance to the next-nearest Co atom in the chain. The total contribution to the DMI is small since the different contributions nearly cancel each other out, as it is *e.g.* the case for (34) and (42).

two magnetic atoms via a non-magnetic surface atom.

We consider two magnetic atoms A and B with normed spins $\hat{\mathbf{S}}_A$ and $\hat{\mathbf{S}}_B$, respectively, that are placed on a substrate with atoms that are non-magnetic but exhibit a large SOC constant ξ. Then the anisotropic exchange interaction of the two deposited atoms via a substrate atom positioned at the origin is given by [86]

$$H_{\mathrm{DM}} = -V_{\mathrm{eff}}(\xi)\,\frac{\sin\left[k_{\mathrm{F}}\left(R_A+R_B+R_{AB}\right)+\eta\right]\hat{\mathbf{R}}_A\cdot\hat{\mathbf{R}}_B}{R_A R_B R_{AB}}\left(\hat{\mathbf{R}}_A\times\hat{\mathbf{R}}_B\right)\left(\hat{\mathbf{S}}_A\times\hat{\mathbf{S}}_B\right), \tag{6.15}$$

where $V_{\mathrm{eff}}(\xi)$ is a SO induced potential, $\mathbf{R}_A = R_A\hat{\mathbf{R}}_A$ and $\mathbf{R}_B = R_B\hat{\mathbf{R}}_B$ point to the two magnetic atoms' sites, that are $R_{AB} = |\mathbf{R}_B - \mathbf{R}_A|$ apart from each other, k_{F} is the absolute of the Fermi vector and η is a phase shift induced by the magnetic atoms.

In the following we will explore formula (6.15) by an analysis of the energy correction values coming from each atom site in the unit cell. In Fig. 6.10 the absolute value of the atom-resolved contributions to the **D**-vector as they result from the calculated SOC energy corrections for $\tilde{q} = 0.1$ and rotation axes in x- and z-direction as shown

with respect to the distance to the next-nearest chain of Co atoms. In addition to the strength of the resulting **D**-vector contribution the direction indicated by a vector in the xz-plane is shown in the small picture b in Fig. 6.10. Due to the inversion symmetric setup of the unit cell, the sum over all contributions vanishes as two atoms i and $i+1$ ($1 \leq i \leq 44$) form a pair connected by inversion symmetry via the origin and their contributions cancel out. This is in agreement with Eq. (6.15) as the inversion operator only changes the sign of $\hat{\mathbf{R}}_A \times \hat{\mathbf{R}}_B$ and thus the sign of H_{DM}.

A second characteristic of the investigated data in Fig. 6.10 is that the contributions show a tendency to decrease with increasing distance to the nearest Co chain. According to Eq. (6.15) this decay should have an $1/R^2$-like characteristic.

Finally we denote that the strength of H_{DM} becomes largest when $\hat{\mathbf{S}}_A \times \hat{\mathbf{S}}_B$ is parallel to $\hat{\mathbf{R}}_A \times \hat{\mathbf{R}}_B$. In other words, we expect the tendency that the energy contribution of a substrate atom is largest perpendicular to the rotation plane of the spins $\hat{\mathbf{S}}_A$ and $\hat{\mathbf{S}}_B$. This results in a vortex-like structure, when the energy corrections are denoted by a vector. This is illustrated by the small picture b in Fig. 6.10.

6.6 Magnetic Ground State of Co chains

Up to this point of this chapter we have analyzed the system Co/Pt(664) with respect to the spin stiffness A, the Dzyaloshinskii-vector (**D**-vector) and the anisotropy tensor $\underline{\mathsf{K}}$ which contains the information about the magnetic anisotropy up to the second order in the magnetic moment $\mathbf{m}$. By means of the underlying micromagnetic model, in Chapter 2 we derived two criteria for the appearance of planar homogeneous and inhomogeneous spiral magnetic structures, Eqs. (2.39) and (2.52), respectively. We now have the ability to analyze these criteria by inserting values that are derived from the parameters mentioned above. Thus, we are able to give a prediction for the system's magnetic ground state. The analysis of the two criteria is presented with respect to the rotation axis $\hat{\mathbf{e}}_{\mathrm{rot}} = (\sin\vartheta_r, 0, \cos\vartheta_r)^{\mathrm{T}}$, *i.e.* the direction normal to the rotation plane of the spin moments. Thus, we consider the fact that it is not clear in the first place which angle ϑ_r leads to the most promising spin spiral structure to compete with the collinear magnetic phase of spins pointing parallel to the easy axis:

On the one hand the DMI becomes extremal when the rotation axis points in the same direction as the **D**-vector, on the other hand the energy costs due to (magnetic) anisotropy effects are minimal if the easy axis lies within the rotation plane of the spin moments. Since in most cases both conditions cannot be fulfilled at the same time (this is only possible if the **D**-vector is perpendicular to the easy axis direction), a rotation axis somewhere between these two extremal cases will in general lead to a minimization of the spin-spiral energy, and thus to the best candidate to be compared to the energy of the collinear spin alignment.

In the upper panel of Fig. 6.11 the developing of the two criteria dependent on the

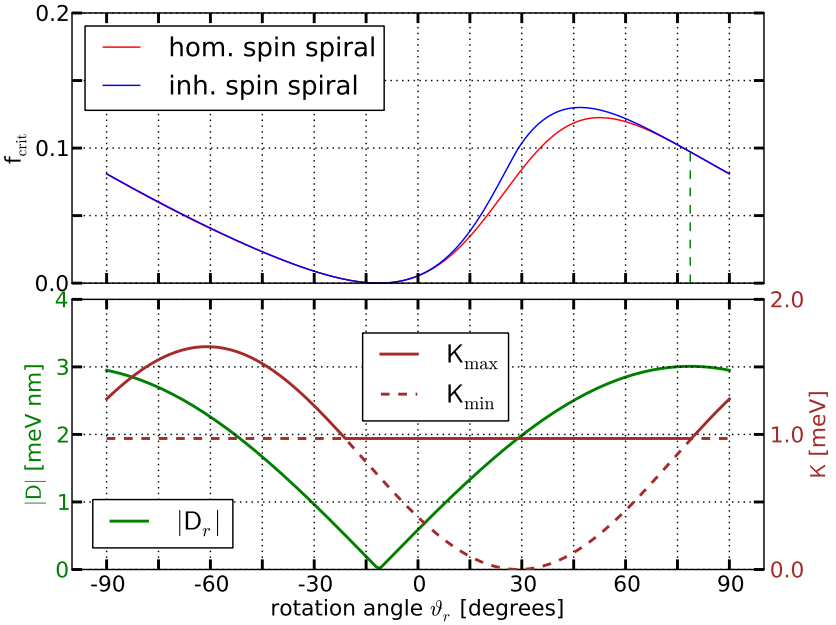

Fig. 6.11: Co/Pt(664): The criteria for the appearance of a homogeneous (red) or an inhomogeneous (blue) spin spiral as a function of the rotation axis ϑ_r. Clearly, neither the homogeneous nor the inhomogeneous spiral is reaching the threshold barrier of 4. However, it turns out that the direction of $\mathbf{D}$ is not necessarily the best direction regarding the minimal spiral energy, since the dashed green line does not represent the maximum of the function.

rotation angle are shown, whereas the function f_{crit} is given by

$$f_{\mathrm{crit}}(\vartheta_r) \overset{?}{>} 4\,,\,,\ \text{with}\ f_{\mathrm{crit}} = \begin{cases} \frac{\mathsf{D}_r^2}{\mathsf{AK}} & ,\ \text{hom. spin spiral} \\ \\ \frac{\mathsf{D}_r^2}{\mathsf{AK}_{\mathrm{max}}} \frac{\pi^2}{4\mathsf{E}(\epsilon)^2} & ,\ \text{inh. spin spiral} \end{cases}, \tag{6.16}$$

with $\overline{\mathsf{K}} = \frac{1}{2}\left(\mathsf{K}_\perp + \mathsf{K}_2\right)$ and $\epsilon = \sqrt{1 - \mathsf{K}_{\mathrm{min}}/\mathsf{K}_{\mathrm{max}}}$. Additional parameters are given by

$$\mathsf{D}_r = \mathbf{D} \cdot \hat{\mathbf{e}}_{\mathrm{rot}} = D_x \sin\vartheta_r + D_z \cos\vartheta_r \tag{6.17}$$

$$\mathsf{K}_\perp = \mathsf{K}_{11} \cos^2\vartheta_r + \mathsf{K}_{33} \sin^2\vartheta_r + 2\mathsf{K}_{13} \cos\vartheta_r \sin\vartheta_r \tag{6.18}$$

In the lower panel of Fig. 6.11 the three parameters D_r, $\mathsf{K}_{\mathrm{max}}$ and $\mathsf{K}_{\mathrm{min}}$ are shown with respect to ϑ_r. The kink of the blue function in the upper panel in Fig. 6.11 ($\vartheta_r = 78°$) represents the angle for which local easy and local hard axis with respect to $K_\perp$ and K_2 are the same. Since for this angle $\mathsf{K}_{\mathrm{min}} = \mathsf{K}_{\mathrm{max}}$ both criteria are equal as no anisotropy effects are to consider in the rotation plane.

The two optimal values for the criteria are given by $f_{\mathrm{crit}}\left(\vartheta = 45°\right) = 0.21$ (homogeneous spin spirals) and $f_{\mathrm{crit}}\left(\vartheta = 45°\right) = 0.25$ (inhomogeneous spin spirals). Clearly the function f_{crit} remains below the threshold value of 4 for both, the homogeneous and inhomogeneous spin spiral. Thus, we conclude that despite uncertainties regarding the calculated parameters it is save to state that a non-collinear magnetic ground state structure is unlikely to appear.

This result is in agreement with the experimental observation [11] that below the blocking temperature of 15 K a long-ranged ferromagnetic order is established as magnetic ground state. Tests regarding the reliability of the results show that by a lower spin stiffness constant (80% of the used value) and changing the easy axis direction to the optimal value (normal to the **D**-vector) the criteria are still not fulfilled, meaning that D_r must be enlarged by a factor of 3.3 to find the criteria for the appearance of an inhomogeneous spiral fulfilled.

The next step is to extend the performed investigations to similar structures and carry out the analysis in the same way as explained in this chapter. In this thesis we also investigate monatomic Fe and Mn chains deposited on Pt(664) step edges. In the following Chapter 7 the performed calculations are discussed and the results are compared to those of the Co chains.

7 Comparison among Transition-Metal Chains

Although the structure of monatomic Co chains deposited on vicinal Pt(111) surfaces is the most-studied system in literature, a variety of similar structural setups are known. For example, one can investigate the behavior of magnetic properties, when the number of Co rows is increased from one strand up to the limit of a full decoration, which has been investigated a few years ago [14, 20]. Another possibility is the substitution of the Pt in the substrate by another $5d$ element or the replacement of the Co rows by a variety of different transition-metal (TM) chains. In this chapter we present a modification of the latter type, where monatomic Fe and Mn chains are deposited along the Pt(664) step-edges instead of the Co atoms.

7.1 Spin stiffness in Fe and Mn chains

In this section the analysis of the spin stiffness A for the two systems Fe/Pt(664) and Mn/Pt(664) is presented. In order to have results that are comparable to those for the Co chains (*cf.* Sec. 6.3) the computational setup, *i.e.* the used parameters and the sequence of performed calculations, is kept as unmodified as possible:

- Development of a self-consistent solution to the Kohn-Sham equation for the collinear spin alignment.
- By use of the resulting charge density as starting point[1], the total energy for different q-values is calculated by means of the force theorem (see Sec. 3.4.1).

In contrast to the Co and the Fe chains the system that deals with Mn chains is expected to have a magnetic ground state in the antiferromagnetic regime. Thus, the charge density with which the force step is performed is calculated in self-consistence cycle with $\tilde{q} = 0.5$. Throughout the calculations of the spin stiffness within this section, the number of incorporated basis functions is set to $K_{\max} = 3.5\, a_{\mathrm{B}}^{-1}$, *i.e.* around 100 functions per atom in the unit cell. Referring to the analysis of the Co chains (see Tab. 6.1) this value gives sufficiently reliable results with reasonable computational costs. For both systems two series with different $\mathbf{k}$-point sets are evaluated. The mesh labeled s_1 contains 64 $\mathbf{k}$-points in the irreducible BZ. For more accurate calculations a denser mesh (labeled

[1] We recall that the interstitial magnetization is set to zero for reasons that are explained in Section 6.3.

s_2) with 256 **k**-points is used. The results are shown in Fig. 7.1. To extract the values for A the energy values are plotted against λ^{-2}, where

$$\lambda = \begin{cases} \frac{\tilde{q}}{a_\mathrm{C}} & , \text{ Fe chains} \\ \\ \frac{\tilde{q}-0.5}{a_\mathrm{C}} & , \text{ Mn chains} \end{cases} . \tag{7.1}$$

and $a_\mathrm{C} = 2.82$ Å represents the next-neighbor distance within the chain. The two functions of the form

$$\mathrm{fit}_1 : \; y = a_1 \cdot x \text{ and } \mathrm{fit}_2 : \; y = a_2 \cdot x + b_2 \tag{7.2}$$

are fitted to the resulting set, where x refers to λ^{-2} and y to the corresponding total-energy deviations with respect to the value of the ferromagnetic order.

For the Fe chains the tendency to the ferromagnetic order is already visible for the coarse mesh s_1, but the calculations with the denser **k**-point set s_2 show in addition that the ferromagnetic order seems to be the magnetic ground state of the system, when spin-orbit coupling is neglected. The same conclusions can be drawn for the Mn chains, whereas the antiferromagnetic is favored here.

In comparison with the Co chains the quadratic regime is assumed to reach up to a distance of $\Delta\tilde{q} = 0.2$ to the collinear ground state. In Table 7.1 the resulting spin stiffness and the corresponding errors are listed. Similar to the analysis of the Co chains it appears that the fit of the form $y = a_2 \cdot x + b_2$ produces more reliable results, in the sense that the variation of A_2 is smaller when the data of the two **k**-point sets are compared. When only the total energies up to $\tilde{q} = 0.15$ (or down to 0.35 for the Mn chains) are taken into account regarding the Fe chains, all resulting spin-stiffness constants for the denser **k**-point mesh increase by a factor of 12 to 19 % compared to the original value. This might be an indication that the choice of the incorporated $\tilde{q}$-values is chosen too large. In the following, however, we will refer to the value of $\mathsf{A} = 71.54\,\mathrm{meV\ nm^2}$ per Fe atom in the case of the Fe chains and for the system with Mn chains we use $\mathsf{A} = 50.13\,\mathrm{meV\ nm^2}$ per Mn atom. We will also note that we expect the real value to be a bit larger than the used value.

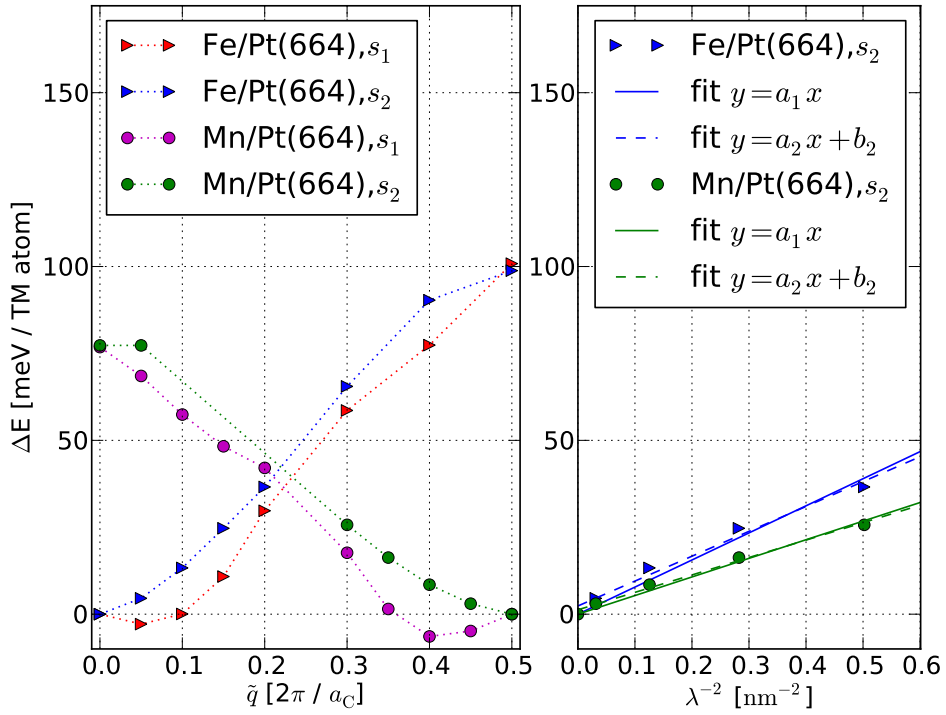

Fig. 7.1: In the left panel of this figure, the total energies with respect to the corresponding $\tilde{q}$-values are shown for both, Fe chains and Mn chains. For both systems we evaluated two series with different sets of **k**-points (s_1 and s_2 refer to 64 and 256 **k**-points, both in the upper BZ). In both systems the denser mesh shows the tendency to a collinear spin alignment, *i.e.* a ferromagnetic and an antiferromagnetic ground state for the Fe chains and the Mn chains, respectively. The right panel shows the energy as function of λ^{-2} in the linear regime of both systems with the two linear fits.

system	range of $\tilde{q}$ $\left[\frac{2\pi}{a_C}\right]$	number of **k**-points	$(A_1 \pm \sigma_1)$ [meV nm^2/TM atom]	$(A_2 \pm \sigma_2)$ [meV nm^2/TM atom]
Fe/Pt(664)	0.0 ... 0.2	64	51.37 ± 8.03	63.01 ± 9.28
Fe/Pt(664)	0.0 ... 0.2	256	77.93 ± 4.68	71.54 ± 5.72
Mn/Pt(664)	0.3 ... 0.5	64	23.91 ± 11.34	39.95 ± 13.43
Mn/Pt(664)	0.3 ... 0.5	256	53.53 ± 2.34	50.13 ± 2.71

Tab. 7.1: The values for the spin stiffness and the corresponding errors for both systems, Fe/Pt(664) and Mn/Pt(664), and for both **k**-point sets, s_1 and s_2 are listed here. Similar to the analysis of the Co chains a fit of the form $y = a \cdot x + b$ (fit on the right side) seems more reasonable. Also it is assumed that the values for spin stiffness change in the order of 2-5 %, when $K_{max} = 3.8\, a_B^{-1}$ is used.

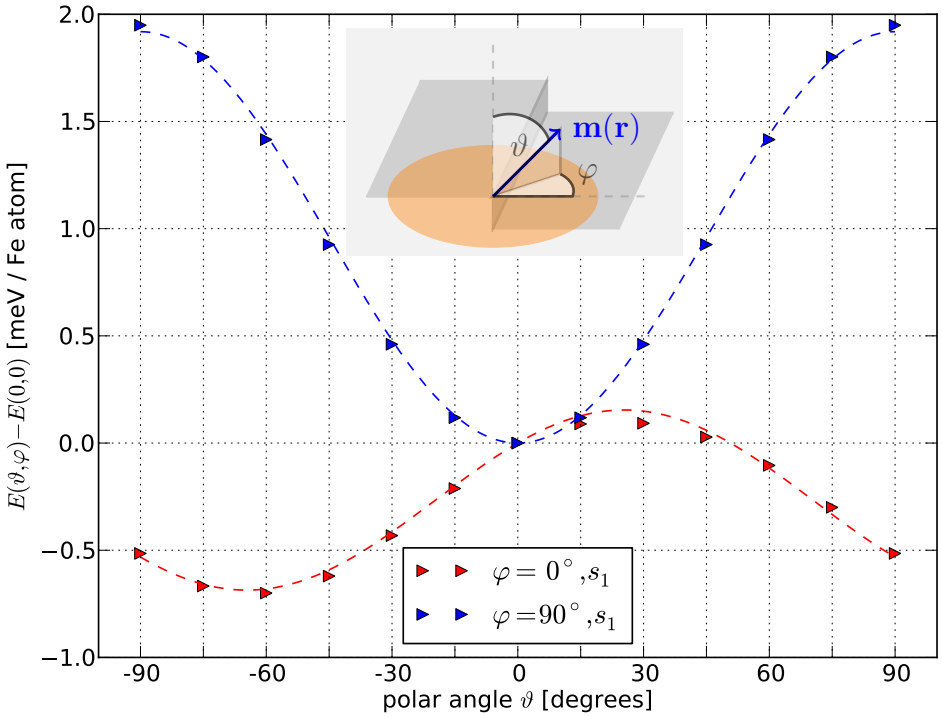

Fig. 7.2: In this figure two series of performed calculations are shown. For $\varphi = 0°$ the total energy is evaluated for spin moments that are located within the plane perpendicular to the chain direction whereas for $\varphi = 90°$ they are in the plane that contains the chain direction and the direction that is normal to the surface (see inner picture). The **k**-point set s_1 contains 128 **k**-points in the whole BZ. A momentous outcome of this analysis is that the hard axis direction is identical to the chain direction, whereas easy and medium axis are located in the plane perpendicular to the chain. Thus, for any cycloidal spiral the spins have to overcome the hard axis.

7.2 The Anisotropy Tensor for Fe and Mn Chains

The investigation of the spin stiffness in the preceding section shows that the two systems Fe/Pt(664) and Mn/Pt(664) have to be treated differently, as far as the evaluation of magnetic anisotropy effects are concerned. Whereas the magnetic moments in the Fe chains prefer to be aligned parallel to each other pointing in the same direction, the minimal energy for the Mn chains is reached in the antiferromagnetic phase, *i.e.* when each spin points in the opposite direction compared to the two vicinal atoms in the chain.

In Fig. 7.2 the determined data for the Fe chains is shown. In the same way as proceeded with the Co chains a function of the form

$$E_{\text{fit}}(\vartheta,\varphi) = A_\varphi \cdot \left[\cos^2(\vartheta + B_\varphi) - \cos^2(B_\varphi)\right] \tag{7.3}$$

is fitted to the two data series, where A_φ and B_φ are two fitting parameters. Evaluating the extrema of these functions, we extract the three principal components

$$\mathsf{k}_1 = -0.69\,\text{meV}\ ,\ \mathsf{k}_2 = 1.92\,\text{meV}\ ,\ \mathsf{k}_3 = 0.15\,\text{meV}\,, \tag{7.4}$$

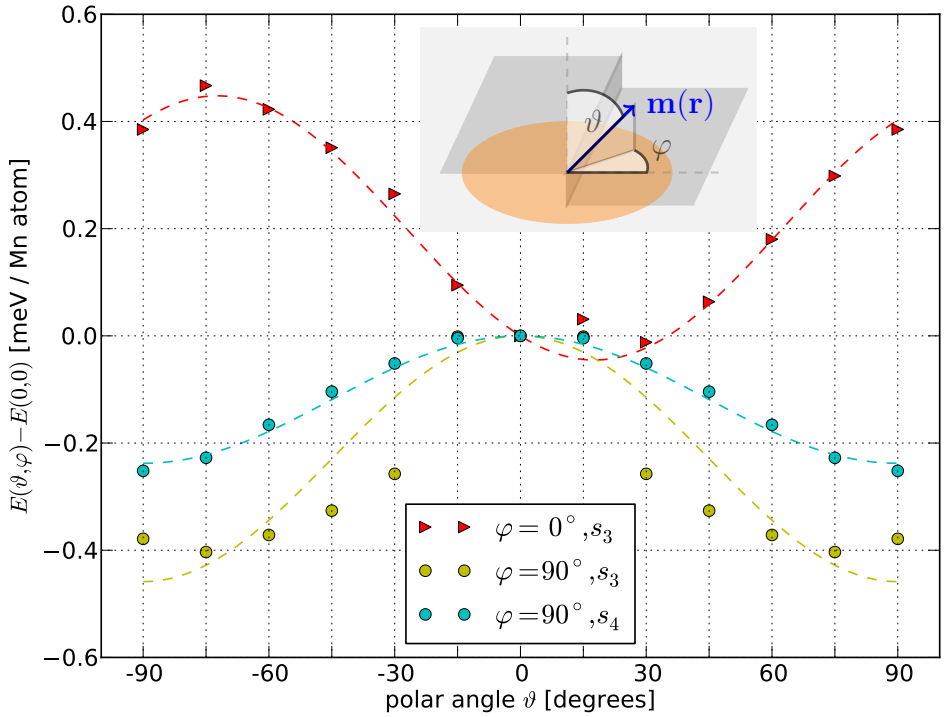

Fig. 7.3: In this figure the calculations of the magnetocrystalline anisotropy in the Mn chains are shown. In Fig. 6.2 it is already referred to the **k**-point sets s_3 and the denser s_4 as they preserve the same mesh density in the doubled unit cell, as s_1 or s_2 provide for the single unit cell. In the Mn chain, the easy axis direction is given by the chain direction. Also it is notable that the energy difference of hard and easy axis is by a factor of 5 lower than it is for the Fe chains.

of the anisotropy matrix $\underline{\mathsf{k}}$ (*cf.* Sec. 2.2.2), where k_1 is the easy axis and tilted by 69° with respect to the terrace normal towards the upper terrace. For spins pointing in hard and easy direction the corresponding energies differ by about 2.6 meV. To reduce the number of atoms these calculations are performed by use of the inversion symmetry of the structure.

On the other hand, the magnetocrystalline anisotropy (MCA) for the Mn chains has to be evaluated in the antiferromagnetic order: Along the y-direction (chain direction) the unit cell has to be of double size in order to account for an alternating spin moment direction along the chain. This results in a unit cell with 46 atom types, where 44 of them form a pair of two atoms whose positions are connected via inversion symmetry. Due to the fact that the new unit cell is stretched by a factor of 2 along the y-direction, the BZ is only half as large, so that a different **k**-point mesh is used (see also Sec. 6.2), where the number of **k**-points along the y-direction is reduced by a factor 2 in order to preserve the quotient between the density along k_x and k_y-direction. The calculated data series are shown in Fig. 7.3. In the plane perpendicular to the chain, a denser **k**-mesh (s_4) is used, since a convergence with respect to the results was not reached yet.

The resulting fits lead to the following values for the three principal components:

$$\mathsf{k}_1 = -0.05\,\mathrm{meV}\ ,\ \mathsf{k}_2 = -0.24\,\mathrm{meV}\ ,\ \mathsf{k}_3 = 0.45\,\mathrm{meV}\,. \tag{7.5}$$

The hard axis is given by k_3 and points into a direction perpendicular to the chain direction and tilted by 72° towards the upper terrace. The energy differences are smaller than those for the Fe chain by more than a factor of 3. In addition the easy axis points along the chain direction. These are very promising insights as a cycloidal spiral rotates over the easy axis, no matter in which direction the **D**-vector is pointing.

In the next section we briefly discuss the results concerning the DMI in both systems, before we conclude this chapter with a prediction for the established magnetic ground state.

7.3 Dzyaloshinskii-Moriya interaction

The computational procedure for the evaluation of the **D**-vector is performed in the same way as presented in Section 6.5. Whereas the spiral calculations for the Fe chains are performed in the ferromagnetic regime, the corresponding analysis for the Mn chains has to be performed in the region of the antiferromagnetic order. In Fig. 7.4 the corresponding energy corrections with respect to different broadening temperatures are shown for the Fe chains, whereas the data related to the Mn chains are shown in Fig. 7.5.

For the lowest value of the broadening temperature, we find the components:

$$\begin{aligned}
\mathrm{Fe/Pt(664)} &: D_x = -2.79 \pm 0.46\,\mathrm{meV\ nm\ /\ Fe\ atom} \\
\mathrm{Fe/Pt(664)} &: D_z = 1.13 \pm 0.98\,\mathrm{meV\ nm\ /\ Fe\ atom} \\
\mathrm{Mn/Pt(664)} &: D_x = -4.19 \pm 2.29\,\mathrm{meV\ nm\ /\ Mn\ atom} \\
\mathrm{Mn/Pt(664)} &: D_z = 5.87 \pm 1.76\,\mathrm{meV\ nm\ /\ Mn\ atom}
\end{aligned}$$

Whereas the system with the Fe chain reveals a DMI that is of similar strength to the Co system, the Mn system shows the largest value for the **D**-vector.

7.4 Search for homochiral spirals in Fe and Mn chains

In a similar way to the proceedings with the Co chains in Chapter 6, the analysis of the two systems Fe/Pt(664) and Mn/Pt(664) concludes with an investigation of the magnetic ground state. The system-specific quantities – spin stiffness A, **D**-vector and anisotropy tensor $\underline{\mathsf{K}}$ – give rise to some parameters that enter the two criteria for the appearance of homogeneous and inhomogeneous spin spirals (see Eq. (6.16)). By evaluating the function f_{crit} for different rotation axes $\hat{\mathbf{e}}_{\mathrm{rot}}$ and comparing it to the critical threshold value 4, it is possible to give a prediction for the magnetic ground state of the two structures.

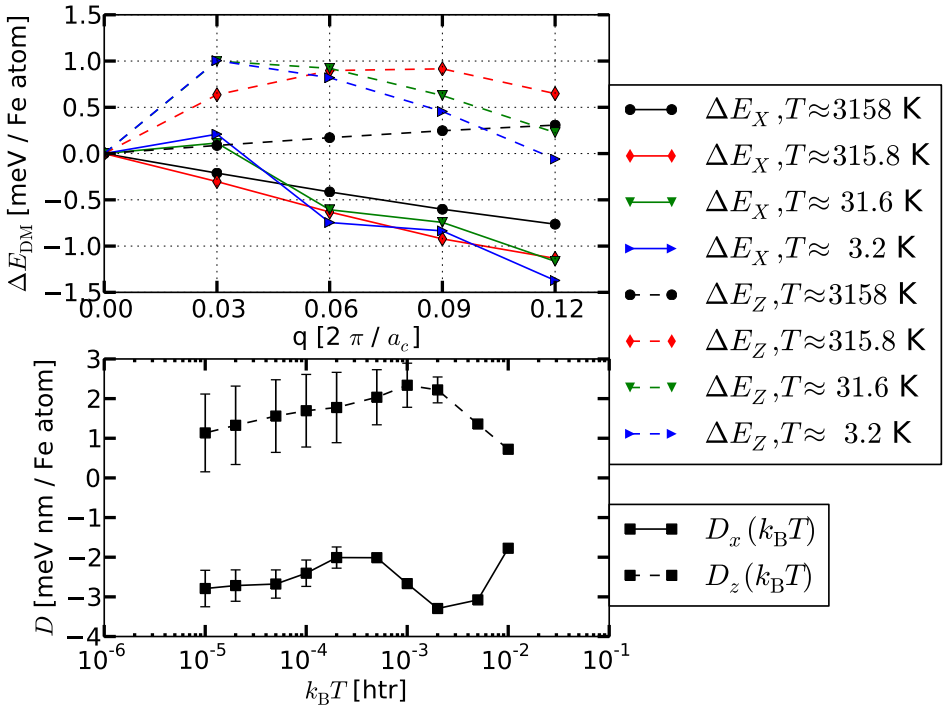

Fig. 7.4: In this figure the energy differences with respect to different $\tilde{q}$-values are shown for Fe/Pt(664). The two components of the **D**-vector arise from these energy differences that represent the shift in the energy when SOC is included. The DMI appears to be equaly strong compared to the DMI of the Co chains.

The Co chains show a ferromagnetic ground state in accordance to experimental observations [11]. However, for the Fe and the Mn chains we notice some auspicious properties that may lead to different conclusions:

- The spin stiffness A is smaller by a factor 0.7 (Fe chains) and 0.5 (Mn chains) compared to the value for the Co chains. Since non-collinear magnetic structures are prevented in systems with large A, this instance is beneficial for the appearance of spin spirals.

- For both cases the absolute value of the **D**-vector is in the same order (Fe chains) or larger (Mn chains) than the corresponding size for the Co system. Since the strength of this value enters the criteria in quadratic order, it is most advantageous for a spiral structure.

- Finally for the Mn system, the easy axis direction points along the chain direction, which means that a cycloidal spiral structure rotates over the easy axis, no matter which value for $\hat{\mathbf{e}}_{\mathrm{rot}}$ is regarded. In addition the anisotropy energy, *i.e.* the energy difference for this system when spins are aligned parallel to the hard and the easy axis, is the smallest for all investigated systems.

The last item, however, is not true for the Fe chains. The anisotropy energy of the Fe

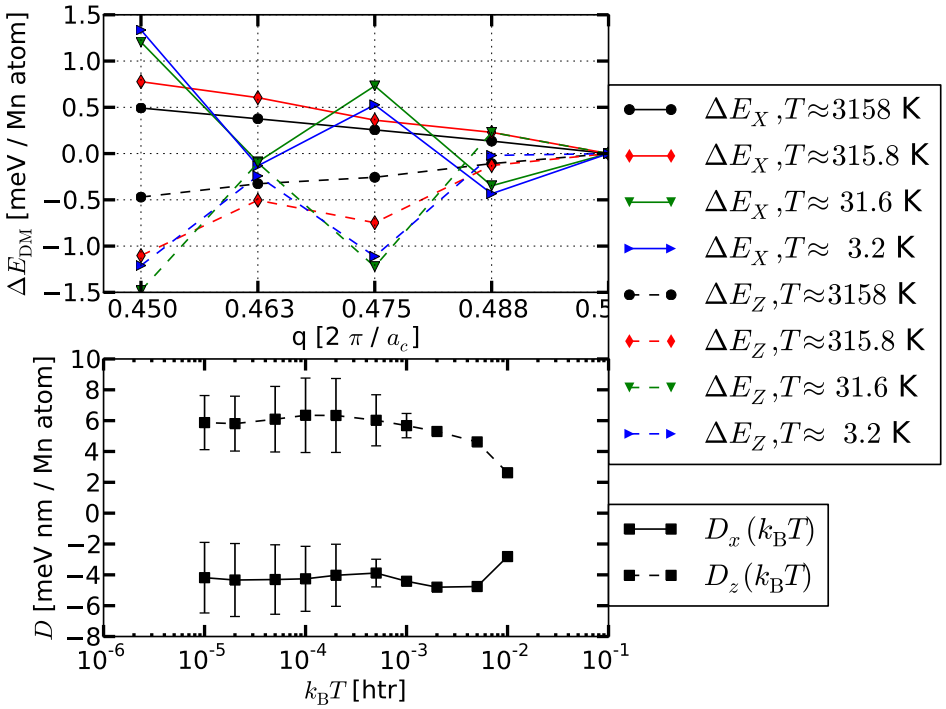

Fig. 7.5: In this figure the energy differences with respect to different $\tilde{q}$-values are shown for Mn/Pt(664). The two components of the **D**-vector arise from these energy differences that represent the shift in the energy when SOC is included. The DMI appears to be stronger than in the case of Co/Pt(664).

chains is not only the largest value that has been evaluated in this thesis, in addition, the hard axis points in the chain direction. Thus, a cycloidal spiral has to rotate over the hard axis, which is the case for all possible rotation axes $\hat{\mathbf{e}}_{\mathrm{rot}}$.

In Fig. 7.6 the resulting functions f_{crit} for the two criteria are shown. The most auspicious values for the criteria

$$\begin{aligned} \text{homogeneous spin spiral} \quad &: \quad f_{\mathrm{crit}}(\vartheta_r = -69^\circ) = 0.07 \\ \text{inhomogeneous spin spiral} \quad &: \quad f_{\mathrm{crit}}(\vartheta_r = -69^\circ) = 0.09 \end{aligned}$$

are clearly below the critical value of 4. This means that despite the fact that the performed calculations yield a non-vanishing DMI for the system with the Fe chains, the disadvantageous anisotropy properties lead to a collinear ferromagnetic spin alignment nonetheless. Although it cannot be seen as the leading factor, it is furthermore disadvatageous that the **D**-vector is pointing almost in the easy axis direction (less than 3° difference with respect to the polar angle). As a consequence the maxima of f_{crit} are even smaller than the corresponding values for the Co chains.

In contrast to the Co and the Fe chains, the investigation of the system Mn/Pt(664) leads to a non-collinear ground state. The corresponding analysis is shown in Fig. 7.7.

Clearly a regime of $\vartheta_r = -83^\circ$ to $\vartheta_r = -22^\circ$ (for the appearance of a homogeneous spin spirals) and $\vartheta_r = -88^\circ$ to $\vartheta_r = -14^\circ$ (for the appearance of an inhomogeneous

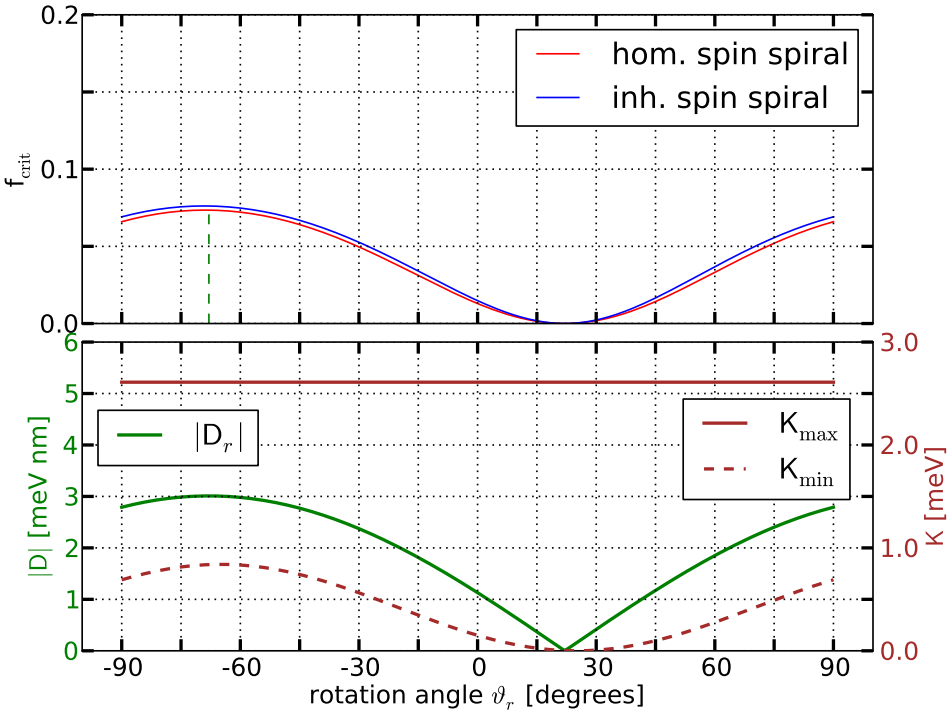

Fig. 7.6: In this figure we present the two criteria as functions of the rotation angle ϑ_r. The optimal angle with respect to the DMI contribution ($\vartheta_r = -68°$) corresponds to a bad constellation for the anisotropy and *vice versa*. Since the criterion is not fulfilled for both, homogeneous and inhomogeneous spirals, the magnetic ground state is collinear.

spin spirals) is detectable that predict spiral magnetic structures to be energetically more favorable than the collinear ground state of spins that point along the easy axis direction. For an angle of $\vartheta = -60°$ the two criteria become maximal:

$$\begin{aligned} \text{homogeneous spin spiral} \quad &: \quad f_{\text{crit}}(\vartheta_r = -60°) = 8.12 \\ \text{inhomogeneous spin spiral} \quad &: \quad f_{\text{crit}}(\vartheta_r = -60°) = 10.02\,. \end{aligned}$$

The energy of a homogeneous spiral is given by (*cf.* Sec. 2.3.1)

$$E = \mathsf{A}\lambda^{-2} + \mathsf{D}_r\lambda^{-1} + \frac{1}{2}\left(\mathsf{K}_\perp + \mathsf{K}_2\right)\,, \tag{7.6}$$

so that the energy for $\vartheta_r = -60°$ is given by

$$\begin{aligned} E_{\text{min}} &= -\frac{\mathsf{D}_r^2}{4\mathsf{A}} + \frac{1}{2}\left(\mathsf{K}_\perp + \mathsf{K}_2\right) \\ &= -0.215\,\text{meV} + 0.106\,\text{meV} = -0.109\,\text{meV}\,, \end{aligned}$$

which is more favorable than the energy for the collinear spin alignment, $E = 0\,\text{meV}$. The chosen parameters D_r, K_2 and $\mathsf{K}_\perp$ are defined in Eq. (6.18). The corresponding period length is given by

$$\lambda_{\text{min}} = -2\frac{\mathsf{A}}{\mathsf{D}_r} = -15.275\,\text{nm} \approx -54 \cdot a_{\text{C}}\,,$$

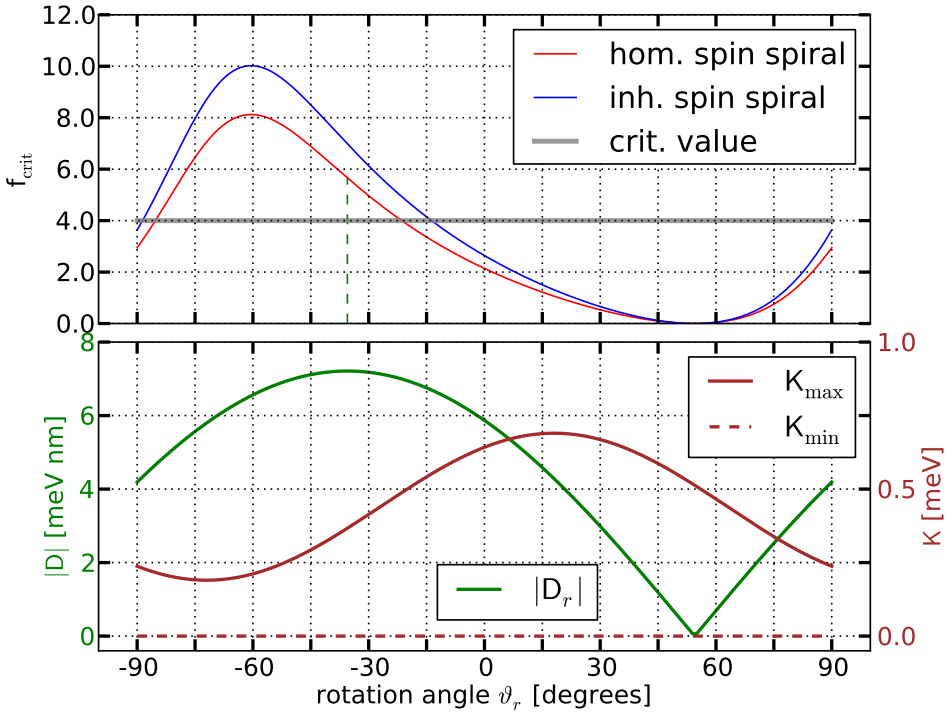

Fig. 7.7: In the investigation of the spiral structure it shows that the spiral is established for both criteria with a maximum at $\vartheta_r = -60°$.

where a_C is the distance of two vicinal Mn atoms in the chain. Since the value of λ_{min} is sensitive to variations of the parameters[2], the calculated value for the period length is not exactly predictable at this point. Nonetheless, we conclude that according to the performed calculation and the presented analysis, a left-handed spiral of a long periodic range is expected to appear in the Mn chains deposited at the step edges of Pt(664).

[2]The previous analysis of all three systems has shown that all three contributions, spin stiffness, **D**-vector and anisotropy tensor, cannot be regarded as fully converged.

8 Summary and Outlook

In this thesis a theoretical *ab initio* investigation of the magnetic ground state in monatomic transition-metal (TM) chains deposited along the step edge of a Pt(664) surface is presented. This study covers the analysis of three different systems, where, besides the experimental [10, 11, 14, 85] and theoretical [7, 15, 16, 17, 19, 20, 21] well-explored Co chains, two new, previously not considered systems of Pt(664)-supported Fe and Mn chains are included in the examination. The coujecture on the magnetic ground state relies on a carful investigation of the magnetic interactions The calculations were performed by use of the FLEUR code, an FLAPW (full-potential linearized augmented planewave) code, based on density functional theory. For all three TM systems, the structural setup and the computational procedure was kept as similar as possible, which allows for a comparison among the different system-specific magnetic interaction parameters.

By use of a micromagnetic model that takes into account the spin-stiffness constant, A, the magnetic anisotropy tensor, $\underline{\mathsf{K}}$, and the Dzyaloshinskii-vector ($\mathbf{D}$-vector), the latter arizing from the Dzyaloshinskii-Moriya interaction (DMI), a prediction concerning the magnetic ground state of the three investigated systems is made. This prediction is manifested in two derived criteria for the appearance of spin-orbit (SO) driven non-collinear homogeneous and inhomogeneous spin-spiral structures.

For the evaluation of the spin-stiffness constant, a series of spin-spiral calculations in the scalar-relativistic approximation for different period lengths is collected. The value of A is evaluated from a quadratic fit to the resulting energy dispersion curve.

In order to study the strength and the direction of the $\mathbf{D}$-vector in the different systems, a more sophisticated computational scheme [24] is used, which allows to perform spin-spiral calculations within the chemical unit cell while treating SO coupling in first order perturbation theory. This is crucial due to the fact that DMI is a SO driven magnetic effect. To obtain the direction of the $\mathbf{D}$-vector, we perform spin-spiral calculations with different rotation axes along the x- and z-direction, which results in two rotation-axis dependent energy corrections. A test calculation was performed to verify that these values correspond to the Cartesian components of the $\mathbf{D}$-vector, D_x and D_z.

The components of the anisotropy tensor $\underline{\mathsf{K}}$ are determined by a set of calculations including SO interaction with different collinear spin moment directions, that are located in the xz- and the yz-plane.

In order to avoid time-consuming calculations, where a self-consistent solution is approached in several iteration steps, the presented calculations for A, $\mathbf{D}$ and $\underline{\mathsf{K}}$ are performed by applying the force theorem, where only one iteration step is performed starting from a well-converged scalar-relativistic self-consistent collinear solution.

In particular for the system with the Co chain, we show test calculations that investigate the convergence of the performed calculations with respect to the number of used **k**-points and considered basis functions.

To our knowledge, this work presents the first theoretical investigation of the DMI in monatomic metallic chains, *i.e.* one-dimensional (1D) magnets. All three systems reveal a strong DMI and, according to the lower symmetry of the chain at the step edge as compared to 2D ultrathin films, the corresponding **D**-vector is not oriented along a high-symmetry direction of the crystal structure. As the direction of this **D**-vector is significantly related to the system's symmetry, we could show that in a step-edged structure with only one mirror plane perpendicular to the chain direction, two Cartesian components can be non-zero.

Summarizing the studies concerning the magnetic ground state, we conclude that a homochiral spiral magnetic structure is unlikely to appear in the Co and the Fe chains. For one part the resulting DMI is not large enough, which we trace back to oppositely directed contributions to the **D**-vector of the Pt atoms nearby the chain and, on the other hand, the magnetic anisotropy represents barriers that are too large to be overcome. This effect is especially strong for the Fe chains, where the hard axis points along the chain direction. Due to the symmetry of the investigated structure, a cycloidal spiral is the only type of spiral the DMI can give rise to. Thus, the spin moments are forced to rotate over the hard axis that is aligned along the chain direction in order to establish a non-collinear spiral structure, which prevents the formation of a spin spiral in the Fe chains. On the other hand, we find a non-collinear magnetic ground state for the Mn chains, close to the antiferromagnetic order. According to the results we predict a left-handed spin-spiral structure with a periodicity of about 54 lattice constants along the chain. This non-collinear ground state should therefore be accessible to experimental studies, so that we expect to find an evidence for the DMI in this particular chain structure. Also our results state that this spiral rotates in a plane that is tilted by about 60° from the (111)-direction towards the upper terrace. If this result can be verified by experiment, it can be explained by a **D**-vector that points in a direction that is not identical to a high-symmetry direction.

Of course even though non-collinear structures in the investigated Co and Fe systems are not predicted to appear, it is still possible to have access to the DMI in these systems from the experimental point of investigation. Recently Szunyogh *et al.* [87] presented in a theoretical study how in experimental observations of the magnon spectrum of Fe/W(110) an asymmetric dispersion can be found that can be assigned to the DMI of this system.

From the state of knowledge that is reached with this thesis one can think of different modifications of the investigated step-edged structure. For one part it is possible to extend the search for homochiral magnetic structures in monatomic TM chains by continuing the investigation with a system of *e.g.* Cr chains. Another promising chemical substitution would be to use an Ir substrate as the step-edged structure. Only recently Mokrousov *et al.* [88, 89] as well as Mazzarello and Tosatti [90] investigated the magnetic interaction in biatomic Fe chains deposited on an Ir(100) surface and found that DMI

can give rise to a chiral magnetic ground state in such structures.

Furthermore, the investigation of multi-rows of Co atoms along the step-edged structure is presented in experiment [14] and theory [20]. It would be interesting to observe if the direction of the **D**-vector shows a similar oscillatory behavior as the easy axis direction. In addition the double-row structure showed a small MAE in the direction perpendicular to the chain, which is therefore a promising candidate for the non-collinear spiral magnetic ground state.

The effect of relaxation in the step-edged structure has been investigated in recent years [19, 7] and is not considered in this thesis. In the case of MAE investigations the relaxed structure does not lead to results that represent experimental data better than calculation with the unrelaxed structure. In addition we do not expect that relaxation results in higher values for DMI as the leading contribution from Pt atoms nearby the chain may tilt towards opposite direction and the spin stiffness constant A tends to increase when the overlap of Co and Pt orbitals increases due to a Co relaxation into the step-edge structure.

Since data storage problems have reached the scale of atomic distance the exploration of low-dimensional magnetic systems will become an interesting and challenging tasks for investigation. Especially the exploration of 1D magnetic system represents a challenging and fascinating topic of research, that will play a crucial role in the near future and will provide further insights in novel magnetic exchange interaction such as the DMI.

9 Acknowledgments

During the process of performing the presented calculations and writing this thesis I have received a lot of support on all aspects related to my work. Many people have supported me in various ways. In the following I want to acknowledge them with great gratitude.

It is my great pleasure to thank Prof. Dr. Stefan Blügel for the opportunity to write this thesis in his institute. By proposing to me the subject matter that this thesis is dealing with, he has drawn my attention to a fascinating topic of research. It was of highest value for my work to regularly discuss the progress of my state of research with him. Throughout the year I could profit from his deep understanding of the subject matter which he shared with me in discussions as often as possible.

Also, I am indebted to Prof. Dr. Stefan Heinze, who kindly agreed to be the second assessor of my thesis.

The present work would not have been possible for the continuous help and guiding support I received from Dr. Gustav Bihlmayer. For the entire period of time he patiently answered a vast number of my questions, if necessary more than once. Many presented analyses of the calculated data can be attributed to his suggestions.

I thank Marcus Heide who shared much of his enormous knowledge in the field of magnetic interactions with me. With high reliability he answered my questions very carefully and in great detail.

In particular I wish to express my gratitude to Bernd Zimmermann who spent a lot of effort in introducing the theoretical background and the computational scheme to me.

Moreover, I thank the whole institute for the wonderful time and a special group around Yuriy, Alex, David and Timo for numerous great soccer games and the countless funny moments that offered a welcome change to the actual work related to the thesis.

I thank the Jülich Supercomputer Center for the computational time on the Juropa supercomputer that was offered to me to perform the calculations.

Last but not least, I thank my parents and Sonat for their love, encouragement, support and for always believing in me and being there for me.

Bibliography

[1] H. Kronmüller and S. Parkin, editors, *Handbook of Magnetism and Advanced Magnetic Materials*, John Wiley & Sons, Ltd, July 2007.

[2] S. Blügel and G. Bihlmayer, *Magnetism of Low-dimensional Systems: Theory*, John Wiley & Sons, Ltd, 2007.

[3] M. Heide, G. Bihlmayer, P. Mavropoulos, A. Bringer, and S. Blügel, Spin–orbit Driven Physics at Surfaces, Newsletter of the Psi-K Network **Vol. 78**(SCIENTIFIC HIGHLIGHT OF THE MONTH 78) (2006).

[4] P. Ferriani, K. von Bergmann, E. Y. Vedmedenko, S. Heinze, M. Bode, M. Heide, G. Bihlmayer, S. Blügel, and R. Wiesendanger, Atomic-Scale Spin Spiral with a Unique Rotational Sense: Mn Monolayer on W(001), Phys. Rev. Lett. **101**(2), 027201 (Jul 2008).

[5] M. N. Baibich, J. M. Broto, A. Fert, F. N. Van Dau, F. Petroff, P. Etienne, G. Creuzet, A. Friederich, and J. Chazelas, Giant Magnetoresistance of (001)Fe/(001)Cr Magnetic Superlattices, Phys. Rev. Lett. **61**, 2472–2475 (Nov 1988).

[6] G. Binasch, P. Grünberg, F. Saurenbach, and W. Zinn, Enhanced magnetoresistance in layered magnetic structures with antiferromagnetic interlayer exchange, Phys. Rev. B **39**, 4828–4830 (Mar 1989).

[7] A. B. Shick and A. I. Lichtenstein, Orbital moment of a single Co atom on a Pt(111) surface—a view from correlated band theory, Journal of Physics: Condensed Matter **20**(1), 015002 (2008).

[8] J. Shen, R. Skomski, M. Klaua, H. Jenniches, S. S. Manoharan, and J. Kirschner, Magnetism in one dimension: Fe on Cu(111), Phys. Rev. B **56**, 2340–2343 (Aug 1997).

[9] H. J. Elmers, J. Hauschild, H. Höche, U. Gradmann, H. Bethge, D. Heuer, and U. Köhler, Submonolayer Magnetism of Fe(110) on W(110): Finite Width Scaling of Stripes and Percolation between Islands, Phys. Rev. Lett. **73**, 898–901 (Aug 1994).

[10] A. Dallmeyer, C. Carbone, W. Eberhardt, C. Pampuch, O. Rader, W. Gudat, P. Gambardella, and K. Kern, Electronic states and magnetism of monatomic Co and Cu wires, Phys. Rev. B **61**(8), R5133–R5136 (Feb 2000).

[11] P. Gambardella, A. Dallmeyer, K. Maiti, M. C. Malagoli, W. Eberhardt, K. Kern, and C. Carbone, Ferromagnetism in one-dimensional monatomic metal chains, Nature **416**(8), 301–304 (Mar 2002).

[12] P. Gambardella, Magnetism in monatomic metal wires, Journal of Physics: Condensed Matter **15**(34), S2533 (2003).

[13] N. D. Mermin and H. Wagner, Absence of Ferromagnetism or Antiferromagnetism in One- or Two-Dimensional Isotropic Heisenberg Models, Phys. Rev. Lett. **17**, 1133–1136 (Nov 1966).

[14] P. Gambardella, A. Dallmeyer, K. Maiti, M. C. Malagoli, S. Rusponi, P. Ohresser, W. Eberhardt, C. Carbone, and K. Kern, Oscillatory Magnetic Anisotropy in One-Dimensional Atomic Wires, Phys. Rev. Lett. **93**, 077203 (Aug 2004).

[15] M. Komelj, C. Ederer, J. W. Davenport, and M. Fähnle, From the bulk to monatomic wires: An *ab initio* study of magnetism in Co systems with various dimensionality, Phys. Rev. B **66**, 140407 (Oct 2002).

[16] A. B. Shick, F. Máca, and P. M. Oppeneer, Anomalous ferromagnetism of a monatomic Co wire at the Pt(111) surface step edge, Phys. Rev. B **69**, 212410 (Jun 2004).

[17] B. Újfalussy, B. Lazarovits, L. Szunyogh, G. M. Stocks, and P. Weinberger, *Ab initio* spin dynamics applied to nanoparticles: Canted magnetism of a finite Co chain along a Pt(111) surface step edge, Phys. Rev. B **70**, 100404 (Sep 2004).

[18] M. Komelj, D. Steiauf, and M. Fähnle, Influence of the substrate on the magnetic anisotropy of monatomic nanowires, Phys. Rev. B **73**, 134428 (Apr 2006).

[19] S. Baud, C. Ramseyer, G. Bihlmayer, and S. Blügel, Relaxation effects on the magnetism of decorated step edges: Co/Pt(664), Phys. Rev. B **73**(10), 104427 (Mar 2006).

[20] S. Baud, G. Bihlmayer, S. Blügel, and C. Ramseyer, First-principles investigation of Co wires at Pt(111) step-edges, Surface Science **600**(18), 4301 – 4304 (2006).

[21] A. Mosca Conte, S. Fabris, and S. Baroni, Properties of Pt-supported Co nanomagnets from relativistic density functional theory calculations, Phys. Rev. B **78**, 014416 (Jul 2008).

[22] M. Bode, M. Heide, K. von Bergmann, P. Ferriani, S. Heinze, G. Bihlmayer, A. Kubetzka, O. Pietzsch, S. Blügel, and R. Wiesendanger, Chiral magnetic order at surfaces driven by inversion asymmetry, Nature **447**, 190–193 (2007).

[23] `http://www.flapw.de`.

[24] M. Heide, G. Bihlmayer, and S. Blügel, Describing Dzyaloshinskii-Moriya spirals from first principles, Physica B: Condensed Matter **404**(18), 2678 – 2683 (2009), Proceedings of the Workshop.

[25] L. M. Falicov, D. T. Pierce, S. D. Bader, R. Gronsky, K. B. Hathaway, H. J. Hopster, D. N. Lambeth, S. S. P. Parkin, G. Prinz, M. Salamon, I. K. Schuller, and R. H. Victora, Surface, interface, and thin-film magnetism, Journal of Materials Research **5**, 1299–1340 (1990).

[26] R. Skomski, *Simple Models of Magnetism*, University Press, Oxford, 2008.

[27] W. Heisenberg, Zur Theorie des Ferromagnetismus, Zeitschrift für Physik **49**(Nr.9), 619–636 (1928).

[28] P. Dirac, On the Theory of Quantum Mechanics, Proc. Roy. Soc. London A **112**, 661–677 (1926).

[29] R. Coehoorn, Period of oscillatory exchange interactions in Co/Cu and Fe/Cu multilayer systems, Phys. Rev. B **44**(17), 9331–9337 (Nov 1991).

[30] D. Lyons and T. A. Kaplan, A Cluster Method for Finding Minimum Energy Spin States, J. Phys. Chem. Solids **25**, 645–648 (1964).

[31] T. Yildirim, A. B. Harris, A. Aharony, and O. Entin-Wohlman, Anisotropic spin Hamiltonians due to spin-orbit and Coulomb exchange interactions, Phys. Rev. B **52**, 10239 (1995).

[32] I. E. Dzyaloshinskii, Thermodynamik theory of "weak" ferromagnetism in antiferromagnetic substrances, Sov. Phys JETP **5** (1957).

[33] T. Moriya, Anisotropic Superexchange Interaction and Weak Ferromagnetism, Phys. Rev. **120**, 91 (1960).

[34] I. Turek, J. Kudrnovský, M. Diviš, P. Franek, G. Bihlmayer, and S. Blügel, First-principles study of the electronic structure and exchange interactions in bcc europium, Phys. Rev. B **68**(22), 224431 (Dec 2003).

[35] G. Bihlmayer, *Magnetism goes Nano*, chapter C2 Reduced Dimensions II: Magnetic Anisotropy, 36$^{\text{th}}$ Spring School of the Institute of Solid State Research (IFF), 2005.

[36] L. Néel, Anisotropie magnétique superficielle et surstructures d'orientation, J. Phys. Rad. **15**, 225 (1954).

[37] N. S. Akulov, Zur Theorie der Feinstruktur der Magnetisierungskurven der Einkristalle, Z. Physik **69**, 78 (1931).

[38] M. Gutzwiller, Effect of Correlation on the Ferromagnetism of Transition Metals, Phys. Rev. Lett. **10**, 159–162 (1963).

[39] J. Hubbard, Electron correlation in narrow energy bands, Proc. Roy. Soc. (London) A **276**, 238–257 (1963).

[40] P. Kurz, G. Bihlmayer, K. Hirai, and S. Blügel, Three-Dimensional Spin Structure on a Two-Dimensional Lattice: Mn /Cu(111), Phys. Rev. Lett. **86**(6), 1106–1109 (Feb 2001).

[41] B. Hardrat, A. Al-Zubi, P. Ferriani, S. Blügel, G. Bihlmayer, and S. Heinze, Complex magnetism of iron monolayers on hexagonal transition metal surfaces from first principles, Phys. Rev. B **79**(9), 094411 (Mar 2009).

[42] B. Zimmermann, Calculation of Dzyaloshinskii-Moriya Interaction in ultrathin magnetic Films: Cr/W(110), Master's thesis, RWTH Aachen, 2010.

[43] W. Döring, *Mikromagnetismus, Handbuch der Physik XVIII/2*, Springer-Verlag Berlin, 1966.

[44] C. Kittel, Physical Theory of Ferromagnetic Domains, Rev. Mod. Phys. **49**, 541 (1949).

[45] I. E. Dzyaloshinskii, Theory of helicoidal structures in antiferromagnets III, Sov. Phys. JETP **20**, 665 (1965).

[46] Y. A. Izyumov, Modulated, or long-periodic, magnetic structures of crystals, Sov. Phys. USPEKHI **27 (11)**, 845–867 (1984).

[47] M. Heide, G. Bihlmayer, and S. Blügel, Non-Planar Dzyaloshinskii Spirals and Magnetic Domain Walls in Non-Centrosymmetric Systems with Orthorhombic Anisotropy, Journal of Nanoscience and Nanotechnology **11**(4), 3005–3015 (2011).

[48] M. Born and R. Oppenheimer, Zur Quantentheorie der Molekeln, Annalen der Physik **389**(20), 457–484 (1927).

[49] P. Hohenberg and W. Kohn, Inhomogeneous Electron Gas, Phys. Rev. **136**(3B), B864–B871 (Nov 1964).

[50] W. Kohn and L. J. Sham, Self-Consistent Equations Including Exchange and Correlation Effects, Phys. Rev. **140**, A1133–A1138 (Nov 1965).

[51] L. H. Thomas, The calculation of atomic fields, Mathematical Proceedings of the Cambridge Philosophical Society **23**(05), 542–548 (1927).

[52] R. O. Jones, *NIC Series Volume 31 Computational Nanoscience: Do It Yourself! Lecture Notes*, chapter Introduction to Density Functional Theory and Exchange-Correlation Energy Functionals, Johannes Grotendorst and Stefan Blügel and Dominik Marx, IFF, Forschungszentrum Jülich, winterschool edition, February 2006.

[53] C. F. v. Weizsäcker, Zur Theorie der Kernmassen, Zeitschrift für Physik A Hadrons and Nuclei **96**, 431–458.

[54] S. Blügel and G. Bihlmayer, *NIC Series Volume 31 Computational Nanoscience: Do It Yourself! Lecture Notes*, chapter The Full-Potential Linearized Augmented Plane Wave Method, Johannes Grotendorst and Stefan Blügel and Dominik Marx, IFF, Forschungszentrum Jülich, winterschool edition, February 2006.

[55] P. A. M. Dirac, Note on Exchange Phenomena in the Thomas Atom, Mathematical Proceedings of the Cambridge Philosophical Society **26**(03), 376–385 (1930).

[56] G. Ortiz and P. Ballone, Correlation energy, structure factor, radial distribution function, and momentum distribution of the spin-polarized uniform electron gas, Phys. Rev. B **50**, 1391–1405 (Jul 1994).

[57] R. O. Jones and O. Gunnarsson, The density functional formalism, its applications and prospects, Rev. Mod. Phys. **61**, 689–746 (Jul 1989).

[58] J. P. Perdew and A. Zunger, Self-interaction correction to density-functional approximations for many-electron systems, Phys. Rev. B **23**, 5048–5079 (May 1981).

[59] J. P. Perdew, K. Burke, and M. Ernzerhof, Generalized Gradient Approximation Made Simple, Phys. Rev. Lett. **77**, 3865–3868 (Oct 1996).

[60] Y. Wang and J. P. Perdew, Correlation hole of the spin-polarized electron gas, with exact small-wave-vector and high-density scaling, Phys. Rev. B **44**, 13298–13307 (Dec 1991).

[61] J. Tao, J. P. Perdew, V. N. Staroverov, and G. E. Scuseria, Climbing the Density Functional Ladder: Nonempirical Meta–Generalized Gradient Approximation Designed for Molecules and Solids, Phys. Rev. Lett. **91**, 146401 (Sep 2003).

[62] A. D. Becke, A new mixing of Hartree-Fock and local density-functional theories, J. Chem. Phys. **98**(2), 1372–1377 (1993).

[63] V. L. Moruzzi, J. F. Janak, and A. R. Williams, *Calculated electronic properties of metals*, Pergamon Press, 1978.

[64] A. R. Mackintosh and O. K. Andersen, Electrons at the Fermi Level, Cambridge University Press **77**, 149 (1980).

[65] M. Methfessel and J. Kübler, Bond analysis of heats of formation: application to some group VIII and IB hydrides, Journal of Physics F: Metal Physics **12**(1), 141 (1982).

[66] U. von Barth and L. Hedin, A local exchange-correlation potential for the spin polarized case. i, Journal of Physics C: Solid State Physics **5**(13), 1629 (1972).

[67] K. Capelle and G. Vignale, Nonuniqueness of the Potentials of Spin-Density-Functional Theory, Phys. Rev. Lett. **86**, 5546–5549 (Jun 2001).

[68] A. K. Rajagopal and J. Callaway, Inhomogeneous Electron Gas, Phys. Rev. B **7**, 1912–1919 (Mar 1973).

[69] A. K. Rajagopal, Inhomogeneous relativistic electron gas, Journal of Physics C: Solid State Physics **11**(24), L943 (1978).

[70] A. H. MacDonald and S. H. Vosko, A relativistic density functional formalism, Journal of Physics C: Solid State Physics **12**(15), 2977 (1979).

[71] G. Baym, *Lectures on Quantum Mechanics*, volume 3, Westview Press, 1969.

[72] A. H. MacDonald, W. E. Picket, and D. D. Koelling, A linearised relativistic augmented-plane-wave method utilising approximate pure spin basis functions, Journal of Physics C: Solid State Physics **13**(14), 2675 (1980).

[73] J. C. Slater, Wave Functions in a Periodic Potential, Phys. Rev. **51**, 846–851 (May 1937).

[74] P. Schwerdtfeger, J. R. Brown, J. K. Laerdahl, and H. Stoll, The accuracy of the pseudopotential approximation. III. A comparison between pseudopotential and all-electron methods for Au and AuH, **113**(17), 7110–7118 (2000).

[75] O. K. Andersen, Linear methods in band theory, Phys. Rev. B **12**, 3060–3083 (Oct 1975).

[76] E. Wimmer, H. Krakauer, M. Weinert, and A. J. Freeman, Full-potential self-consistent linearized-augmented-plane-wave method for calculating the electronic structure of molecules and surfaces: O_2 molecule, Phys. Rev. B **24**, 864–875 (Jul 1981).

[77] H. Krakauer, M. Posternak, and A. J. Freeman, Linearized augmented plane-wave method for the electronic band structure of thin films, Phys. Rev. B **19**, 1706–1719 (Feb 1979).

[78] D. D. Koelling and B. N. Harmon, A technique for relativistic spin-polarised calculations, Journal of Physics C: Solid State Physics **10**(16), 3107 (1977).

[79] P. Kurz, *Non-Collinear Magnetism at Surfaces and in Ultrathin Films*, PhD thesis, RWTH Aachen, 2000.

[80] P. H. Dederichs, S. Blügel, R. Zeller, and H. Akai, Ground States of Constrained Systems: Application to Cerium Impurities, Phys. Rev. Lett. **53**, 2512–2515 (Dec 1984).

[81] P. Kurz, F. Förster, L. Nordström, G. Bihlmayer, and S. Blügel, *Ab initio* treatment of noncollinear magnets with the full-potential linearized augmented plane wave method, Phys. Rev. B **69**, 024415 (Jan 2004).

[82] S. Youn, W. Mannstadt, and A. Freeman, Analytic Spin-Orbit Coupling Matrix Element Formulae in FLAPW Calculations, Journal of Computational Physics **172**(1), 387 – 391 (2001).

[83] M. Heide, *Magnetic domain walls in ultrathin films: Contribution of the Dzyaloshinskii-Moriya interaction*, PhD thesis, RWTH Aachen, 2006.

[84] P. Gambardella, M. Blanc, H. Brune, K. Kuhnke, and K. Kern, One-dimensional metal chains on Pt vicinal surfaces, Phys. Rev. B **61**, 2254–2262 (Jan 2000).

[85] P. Gambardella, M. Blanc, L. Bürgi, K. Kuhnke, and K. Kern, Co growth on Pt(997): from monatomic chains to monolayer completion, Surface Science **449**(1-3), 93 – 103 (2000).

[86] A. Fert and P. M. Levy, Role of Anisotropic Exchange Interactions in Determining the Properties of Spin-Glasses, Phys. Rev. Lett. **44**, 1538–1541 (Jun 1980).

[87] L. Udvardi and L. Szunyogh, Chiral Asymmetry of the Spin-Wave Spectra in Ultrathin Magnetic Films, Phys. Rev. Lett. **102**(20), 207204 (May 2009).

[88] Y. Mokrousov, A. Thiess, and S. Heinze, Structurally driven magnetic state transition of biatomic Fe chains on Ir(001), Phys. Rev. B **80**, 195420 (Nov 2009).

[89] M. Menzel, Y. Mokrousov, R. Wieser, K. von Bergmann, E. Vedmedenko, S. Blügel, S. Heinze, A. Kubetzka, and R. Wiesendanger, to be published.

[90] R. Mazzarello and E. Tosatti, Connection between magnetism and structure in Fe double chains on the Ir(100) surface, Phys. Rev. B **79**, 134402 (Apr 2009).

Selbständigkeitserklärung

Hiermit versichere ich, die vorliegende Arbeit selbständig und nur unter Zuhilfenahme der angegebenen Quellen und Hilfsmittel angefertigt zu haben.

Benedikt Schweflinghaus
Jülich, den 10. Oktober 2011